THE UNIVERSITY OF HULL

Monte-Carlo Simulations of Gunn Diodes and Hot-Phonon Effects in Bulk Semiconductors

being a Thesis submitted for the Degree of Doctor of Philosophy

in the University of Hull

By

Nicholas Appleyard B.Sc. (Hons.)

August 2016

Summary of Thesis

This thesis uses Monte Carlo simulations to investigate electron transport in GaAs, its ternary $In_{0.53}Ga_{0.47}As$ and GaN. Ensemble Monte Carlo methods are used to determine the effects of a non-equilibrium phonon distribution on the transport properties of bulk $In_{0.53}Ga_{0.47}As$. Hot phonons are shown to reduce the critical field, peak velocity and saturation velocity. The dominant hot phonon effects in $In_{0.53}Ga_{0.47}As$ are shown to be diffusive heating and phonon re-absorption. Evidence of the phonon drag effect is not found.

A notched GaAs Gunn diode originally modelled by J. Tully in 1983 [1] is then recreated with a finer mesh and more superparticles. The device is shown to operate in accumulation mode with a considerable 'dead zone'. The model is shown to be consistent with the original to a reasonable estimate considering the uncertainty surrounding material parameters. Significantly less noise is present demonstrating the increased precision offered by a Monte Carlo model with an increased resolution.

Characteristics of GaN Gunn diodes are then explored. Results are presented for a device operating in accumulation mode with an operating frequency of 164 GHz. Results are then presented for a device operating in dipole mode with an operating frequency of 119 GHz. The mechanisms surrounding the function of these devices are analysed and shown to be consistent with the literature.

Finally, a proof of concept 2-dimensional device simulator is validated through comparison with an equivalent 1-dimensional device. While equivalency is proven a number of obstacles are highlighted surrounding computational efficiency and optimum simulation parameters.

Contents

Acknowledgements

I would like to take this opportunity to thank my research supervisor Dr Angela Dyson, firstly for providing me with the excellent opportunity to study towards a PhD in such an interesting and enjoyable subject and secondly for her continued guidance and support throughout my PhD. Angela has been an excellent supervisor and I could not have completed my PhD without her help.

I would also like to thank Dr Dan Naylor, both for his part in developing the Monte Carlo code on which my work is based and also for passing on his invaluable experience on the theory of semiconductor transport. Despite being totally incompetent at playing 'RISK' Dan has been a brilliant colleague to discuss ideas with surrounding my work.

I must also thank those who I have had the pleasure of sharing an office with over the years. Ant Edwards, Beth Newton, Mr Raj and the Smith bros. along with the occasional cameo appearance from Alison Marshall have helped make each day of my PhD more enjoyable.

Finally, I would like to thank the Office of Naval Research for funding my studies for three and a half years.

Declaration of Authorship

I declare that the work presented in this thesis is original, my own and has not been previously submitted for examination for any other award. Where I have used the results, concepts or work of others they have been acknowledged at point of use.

Signed: . . . . . .

Date: . . . . . .

Conference Presentations

N. Appleyard, D. R. Naylor, A. Dyson and B. K. Ridley, "Red Hot Phonons in GaN", TMCS IV, Salford, United Kingdom, January 2014

N. Appleyard, D. R. Naylor, A. Dyson and B. K. Ridley, "Hot phonon effects in $In_{0.53}Ga_{0.47}As$ and GaN", WOCSDICE, Smolenice, Slovakia, August 2015

"My point is, life is about balance.

The good and the bad.

The highs and the lows.

The Piña and the Colada."

Addison Marshall 2014

Chapter 1. Introduction

Prior to the 1950's germanium was the most popular semiconductor material for device fabrication but it was severely limited by its large leakage current at only slightly elevated temperatures. By the early 1960's silicon had succeeded germanium as the material of choice for semiconductor device fabrication and remains the most popular today. Over the past 50 years the semiconductor industry has seen exponential growth; in both device capability and the adoption of devices by society. There is limited potential associated with silicon devices due to the intrinsic properties of the material; these limitations are beginning to be realised [2]. This has led to increased research in other semiconductor materials, especially the III-V group of semiconductors and their ternaries such as GaAs and InGaAs and III-nitrides like GaN and InN.

1.1. GaN

GaN has a high heat capacity, high thermal conductivity, large band-gap and high negative differential mobility meaning devices are capable of operating at high

powers, high current density and have a high cut-off frequency. GaN devices are known to operate at higher frequencies than silicon devices and even outperform devices made with other wide bandgap materials such as SiC [2]. Increased GaN production and the ability to produce larger GaN substrates is reducing the costs of GaN technology leading to more commercial interest in the material [3]. Yole's 'Power GaN market and SiC modules, devices and substrates for power electronics market' report estimates that by 2020 the GaN power device market would be worth over US$550 million driven in part by the increasing popularity of electric automobiles [3].

In addition to the potential for GaN in the high power electronics market; GaN can be used to make High Electron Mobility Transistors (HEMT's). HEMTs can be created without modulation doping in GaN hetero-structures due to spontaneous and piezoelectric fields forming at the interface giving rise to a two-dimensional electron gas [4]. Due to the significant Negative Differential Resistance (NDR) region in GaN it can also be used to fabricate Transferred Electron (TE) devices such as Gunn diodes [5]. In 2000 Pavlidis et al. [6] fabricated and tested the first GaN Gunn diode. GaN Gunn diodes were shown to operate at double the frequency of GaAs diodes (87 GHz compared with 40 GHz) and the output power density increased significantly ($2x10^5$ W/cm^2 for the GaN device compared to ~10^3 W/cm^2 for GaAs devices [6]).

Although the potential of GaN as a material is huge there are a number of obstacles which must be overcome before the technology can fully mature. One of the main obstacles to GaN technology is perhaps the most fundamental, material growth. Progress in GaN growth was held back by a difficulty in finding a suitable growth substrate. GaN growth originally focussed on heteroepitaxial growth on foreign substrates like sapphire, gallium arsenide, silicon and silicon carbide [7]. Large dislocation densities amongst other undesirable characteristics were present when GaN was grown on sapphire [8]. In 1986 Amano et. al made significant progress in material growth, improving the optical and electrical properties of GaN layers by growing GaN on sapphire using atmospheric pressure Metal-Organic Vapour Phase Epitaxial (MOVPE) with AlN buffer layers [9].

The most dominant growth technique used today is Hydride Vapour Phase Epitaxy (HVPE) [2]. HVPE boasts high growth rates, good control of impurities and large wafer sizes, however the substrates typically suffer from poor material uniformity and exhibit high strain which leads to bowing and cracking at the interface between GaN and the growth substrate leading to dislocations [2]. The choice of growth substrate is fundamental to material growth. By reducing the lattice mismatch between the growing material and the substrate the dislocation density can be significantly reduced. Reduction in dislocation density by two orders of magnitude

from 10^9 cm^{-2} to 10^7 cm^{-2} has been achieved by growing GaN on GaN/Al_2O_3 substrates [10].

There is a significant disparity between the intrinsic material properties of GaN and the achievable performance of actual GaN devices [2].The saturation velocities in devices such as HEMTs for example are significantly lower than predictions based solely on bulk-material parameters. One of the major limiting factors in achieving predicted saturation velocities is thought to be the 'hot phonon effect' [11]. Pomeroy et al. [11] used conventional Raman thermography combined with Stokes/anti-Stokes temperature measurements to monitor the phonon presence in the channel of AlGaN/GaN HFETs. With a 30V applied bias a phonon temperature of around 1000K was found [11]. Later works using electroluminescence have found electron temperatures of over 1600K in AlGaN/GaN HEMT's [12]. Investigations into HFET degradation found that the most dominant cause of device degradation was due to hot-phonon, hot-electron effects in the channel [13]. With such a growing body of evidence it seems that hot phonons undoubtedly have a significant effect on device performance and longevity.

In the remainder of this chapter the reader is provided with a general overview of the properties of semiconductor crystals. The background physics relevant to studying electron transport using Monte Carlo methods is then discussed. Band structure and various analytical approximations of bands structure are covered along

with an overview of the most dominant scattering mechanisms in III-V and III-Nitride materials.

1.2. Crystal Structure

Semiconductors are highly ordered crystalline materials. Semiconductors can be monatomic materials, like silicon; or can be made up of multiple atoms from binary compounds, like GaN or GaAs, or from ternary compounds, like AlGaN or InGaAs. The arrangement of atoms within a crystal is known as the crystal lattice; all points within a lattice are described using lattice vectors. Any point within the lattice can be reached using a combination of lattice vectors, shown mathematically in two dimensions using,

$$\mathbf{R} = n_1\mathbf{a} + n_2\mathbf{b} \tag{1.1}$$

where $\mathbf{R}$ is any position within the lattice $\mathbf{a}$ and $\mathbf{b}$ are lattice vectors and n_1 and n_2 are integers.

Due to the repeating structure of a semiconductor crystal it is possible to define it using multiple 'unit cells' all joined together.

One of the crystal structures central to solid state physics is the diamond lattice. A diamond lattice traditionally consists of carbon atoms covalently bonded to 4

neighbouring carbon atoms forming a face-centred cubic lattice; semiconductors with a diamond crystal structure include Germanium and Silicon [14].

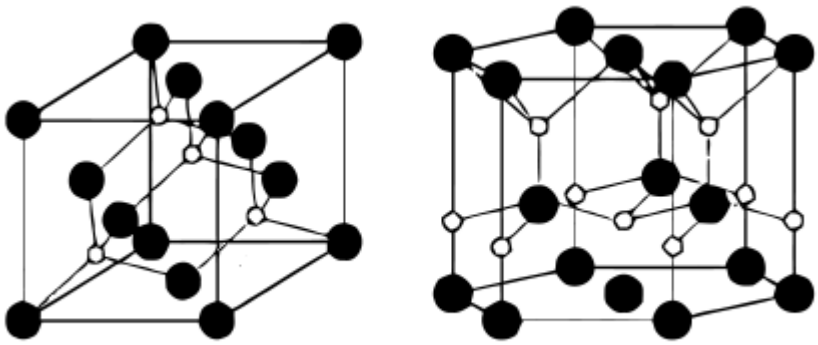

(a) (b)

Figure 1.1 [15] – The zinc blend (a) and wurtzite (b) lattice crystal structures.

A variation of the diamond crystal structure is the zinc blende structure. Originally named after the zinc blende mineral, the zinc blende crystal structure is made up of two materials from a binary compound and follows a similar pattern to the diamond structure; the difference being that each atom is covalently bonded to 4 differing atoms, as shown in Figure 1.1a. Many of the III-V group of semiconductors such as, GaAs, AlAs, InAs, InP and GaN can all crystallise to form a zinc blende structure [16]. Many III-V or III-nitride materials can also crystallise to form a wurtzite structure. Originally named after zinc oxide, the wurtzite structure is made up of tetrahedral bonds much like the zinc blende and diamond structures, differing only by the stacking sequence. The change in stacking sequence means that unlike the face centred cubic symmetry of the zinc blende lattice the wurtzite structure has hexagonal symmetry (See Figure 1.1b).

The same material, GaN for example, can form either a wurtzite or zinc blende structure depending on how it is grown. GaN grown on sapphire substrates tend to acquire the hexagonal symmetry from the sapphire lattice to form a wurtzite crystal, whereas GaN grown on a GaAs substrate will often form a zinc blende crystal [17].

1.3. Band structure

If a free electron is treated as a wave with a frequency, $\omega = E/\hbar$ (where $\hbar$ is the reduced Planck's constant), the time independent wave equation can be solved to give an expression for the energy of the wave, in terms of its wave vector $\mathbf{k}$:

$$E(\mathbf{k}) = \frac{\hbar^2 \mathbf{k}^2}{2m_0} \qquad 1.2$$

where m_0 is the electron's mass in free space. The product $\hbar\mathbf{k}$ is equivalent to the electron's momentum which implies equation 1.2 is equivalent to the electrons kinetic energy. These same principles can be used to interpret an electron's motion through a semiconductor. A characteristic of a crystalline structure is a periodic potential associated with its highly ordered atomic nuclei and native electrons. It is possible to approximate this many body potential using a prescribed potential $V(\mathbf{r})$, effectively creating a single electron problem [18]. $V(\mathbf{r})$ will act on any electron passing through the material and will vary with electron position $\mathbf{r}$, according to the periodicity of the crystal lattice. In order to determine the wave function of an

electron travelling through a semiconductor material the one electron Schrodinger equation must be solved:

$$\left[-\frac{\hbar^2}{2m_0}\nabla^2+V(\mathbf{r})\right]\psi(\mathbf{r})=E\psi(\mathbf{r}) \tag{1.3}$$

Where $\psi(\mathbf{r})$ is the wave function to be determined, E is electron energy and ∇^2 is the Laplacian operator. Bloch theorem states that any solution to this equation must be periodic, which would take the mathematical form:

$$\psi_{\mathbf{k}} = u_{\mathbf{k}}(r)e^{i\,\mathbf{k}.\mathbf{r}} \tag{1.4}$$

Where $u_{\mathbf{k}}$ is the Bloch function for a lattice with a periodicity such that a translation by vector $\mathbf{R}$ would result in moving one whole period,

$$u_{\mathbf{k}}(\mathbf{r}) = u_{\mathbf{k}}(\mathbf{r}+\mathbf{R}) \tag{1.5}$$

Since the waveform solution to the Schrodinger equation is itself periodic the $E-\mathbf{k}$ relationship can be fully described within one period of the reciprocal lattice. This elementary cell is usually referred to as the Brillouin zone [18][19]. Since the electrons in a semiconductor have only certain allowed values of energy and k-vector, there is a finite number of transitions which they can undertake within the first Brillouin zone. Valley minima, where electrons are likely to be present at room

temperatures, are often represented diagrammatically using $\mathrm{E} - \mathbf{k}$ plots; the energy dispersion for InGaAs is given in Figure 1.2 as an example.

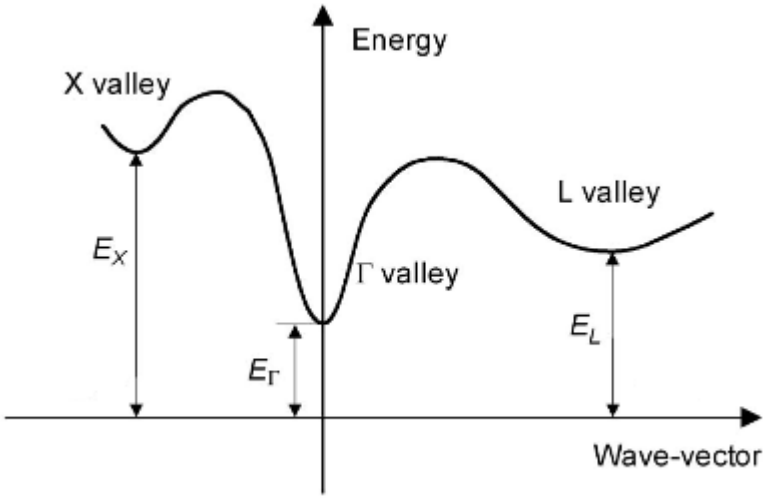

Figure 1.2 – Electron energy dispersion in InGaAs – showing Γ, L and X valleys. [20]

1.4. Analytical band approximations

In order to model an electrons motion and to derive scattering rates it is necessary to define the band structure of the material in which the electrons are propagating. Full band solutions are often immensely numerically complex; as such it is useful to use an analytical approximation. Mobile electrons mostly populate the lowest conduction band valley. This means that, provided they are accurate in the area around the lowest conduction band valley, approximate solutions to the Schrodinger equation will often suffice when studying carrier transport [19][21]. Two of the most established analytical approximations for studying carrier transport are the parabolic and $\mathbf{k}.\mathbf{p}$ approximations. A further approximation called the cosine band

approximation has been used by Naylor et. al to study high field transport in GaN [22]. Fundamental to each of these approximations is the electron effective mass.

1.4.1. *Effective mass*

It can be shown that as an electron travels through a crystal it acts in the same way as a free electron but with a varying mass [23]. In order for this assumption to be valid the potential of the crystal must vary slowly over a unit cell. This ensures that any quantum effects such as reflection and tunnelling can be discounted, allowing the electron to be analysed using Newtonian mechanics [24].

The effective mass, m^*, of an electron is defined as [19][21]

$$\mathrm{m}^* = \frac{\hbar^2}{\mathrm{d}^2\mathrm{E}/\mathrm{d}\mathbf{k}^2} \tag{1.6}$$

Where E is electron energy and $\mathbf{k}$ is the electron $\mathbf{k}$ vector.

1.4.2. *Parabolic approximation*

The relationship between an electrons energy and $\mathbf{k}$ vector can be modified to give the $\mathrm{E}-\mathbf{k}$ relation in terms of its effective mass. The parabolic approximation maintains its accuracy if electrons are close to the valley minima. If high applied fields are considered then electrons are likely to lie close to the band edge [18]. In these circumstances the parabolic approximation can become quite inaccurate. The

parabolic approximation assumes the effective mass of electrons is constant, which is rarely a good fit to the exact band structure and so more complex and flexible methods are often used, such as the $\mathbf{k}.\mathbf{p}$ approximation.

1.4.3. $\boldsymbol{k.p}$ *approximation*

The $\mathbf{k}.\mathbf{p}$ method is used to create a band structure which more accurately represents the exact band structure as calculated using pseudo potential methods when compared with the simple parabolic approximation. If a solution to the one-electron Schrodinger equation is known around the lowest conduction band valley then it is possible to obtain solutions to neighbouring valleys using the product $\mathbf{k}.\mathbf{p}$, where $\mathbf{k}$ is the electron wave vector and $\mathbf{p} = -i\nabla\hbar$.

By substituting the Bloch wave function into the Schrodinger equation Ridley [21] shows that

$$\left[\frac{\mathbf{p}^2}{2m_0} + \frac{\hbar^2}{m_0}\,\mathbf{k}.\mathbf{p} + \frac{\hbar^2\mathbf{k}^2}{2m_0} + V(\mathbf{r})\right] u(\mathbf{k},\mathbf{r}) = E(\mathbf{k})u(\mathbf{k},\mathbf{r}) \qquad 1.7$$

Where $V(\mathbf{r})$ is the periodic potential and $u(\mathbf{k},\mathbf{r})$ is the Bloch lattice function.

Solving the above for a single band, neglecting spin-orbit interaction, the following dispersion relation is found, given in terms of the Kane non-parabolicity to the third order [18],

$$\gamma(\mathbf{E_k}) = \mathbf{E_k}(1 + \alpha\,\mathbf{E_k} + \beta\mathbf{E_k^2} + \eta\mathbf{E_k^3}) \quad 1.8$$

The above approximation is usually accurate when used to the first order, and so only α is used; given by [18],

$$\alpha = \frac{1}{E_g}\left(1 - \frac{m^*}{m_0}\right)^2 \quad 1.9$$

where E_g is the energy gap between the valence band maxima and the first conduction band valley minima, m^* is the electron effective mass at the valley minima and m_0 is the electron rest mass. The $\mathbf{k}.\mathbf{p}$ approximation is often preferred to the parabolic approximation since it accounts for the non-parabolicity of a band and hence has a varying effective mass. Some materials have a highly non-parabolic band structure, such as the Γ valley in GaN, which is not accurately represented by the parabolic or $\mathbf{k}.\mathbf{p}$ approximations.

1.4.4. *Cosine band approximation*

The degree of non-parabolicity in the gamma valley of GaN has meant that full band simulations are usually required to accurately model carrier transport in the material. Ridley, Schaff and Eastman suggested in 2005 that by using a cosine band approximation the non-parabolicity of the Γ valley could be more accurately modelled [25]. Naylor and Dyson used this approximation to investigate the effect of

the gamma valley inflection point on the Negative Differential Resistance (NDR) effects in GaN [22]. The cosine band approximation takes the form:

$$E_{\mathbf{k}} = \frac{E_B}{2}(1 - \cos(\mathbf{k}a)) \tag{1.10}$$

Where $E_{\mathbf{k}}$ is the energy of an electron with wave vector $\mathbf{k}$, E_B is the band width (the energy difference between the minimum and maximum of the valley) and a is the hexagonal lattice constant.

1.5. Boltzmann Transport Equation (BTE)

The original application of the Boltzmann Transport Equation (BTE) was to describe how external forces and collisions affect the velocity distribution of particles in a gas [26]. By using the effective mass approximation electrons within a semiconductor material can be treated classically which means the BTE can be altered to describe how external forces (periodic potential of the crystal lattice) and collisions (scattering events) affect electron transport. The BTE for electron transport is given in terms of the distribution function f(r, p, t), which describes the probability of finding electrons at a time t, with position r and momentum p; the equation takes the general form [19]:-

$$\frac{df}{dt} = \left(\frac{df}{dt}\right)_{force} + \left(\frac{df}{dt}\right)_{diff} + \left(\frac{df}{dt}\right)_{coll} \quad 1.11$$

Where the force term describes the change of f(r, p, t) due to an external force exerted on the electrons, the diff term describes the diffusion of particles and the coll term describes electron scattering events. These functions are not easy to derive and electrons are analysed in six-dimensional position-momentum space, (also known as phase space) which makes the BTE rather complicated. Since an analytic solution to this is equation is not plausible the BTE is often solved using numerical methods such as the Monte Carlo method [18]. A detailed description of the Monte Carlo method will be presented later in this thesis.

1.6. Carrier Scattering

As electrons travel through a semiconductor material their journey is often interrupted by interactions with various perturbations. These interactions translate an electron from $\mathbf{k}$ to $\mathbf{k}'$ and are known as electron scattering events. There are a variety of different scattering mechanisms which an electron may experience, each with a different probability of occurring. Scattering is one of the dominant mechanisms affecting electron transport and so it is important that we know the transition rate from $\mathbf{k}$ to $\mathbf{k}'$, $S(\mathbf{k},\mathbf{k}')$. The transition rate for elastic scattering is given by [19],

$$S(\mathbf{k},\mathbf{k}') = \frac{2\pi}{\hbar} | H_{\mathbf{k}'\mathbf{k}} |^2 \delta(E_f - E_i) \quad 1.12$$

Where $H_{\mathbf{k}'\mathbf{k}}$ is the scattering rate matrix element, specific to each scattering mechanism, connecting $\mathbf{k}$ and $\mathbf{k}'$, E_i is the initial electron energy (before scattering), E_f is the final electron energy (after scattering). To find a scattering rate in three dimensional space the transition rate is integrated across all available final states N_f. The scattering rate, $W(\mathbf{k})$, can then be derived using a result known as Fermi's Golden Rule,

$$W(\mathbf{k}) = \frac{2\pi}{\hbar} \int | H_{\mathbf{k}'\mathbf{k}} |^2 \delta(E_f - E_i) dN_f \quad 1.13$$

Fermi's Golden Rule is found from the time dependent perturbation theory and assumes that each collision is instantaneous. Each collision is not instantaneous, although it is found that Fermi's Golden Rule is still valid if the duration of each collision is much smaller than the time between collisions. This condition is found to be satisfied in the majority of cases [21][24]. Each scattering mechanism will have a different scattering rate matrix element associated with it. To find each scattering rate the appropriate matrix, $H_{\mathbf{k}'\mathbf{k}}$, is substituted into Fermi's golden rule, given in equation 1.13, which is then solved for $W(\mathbf{k})$. The following section will provide an overview of the most common scattering mechanisms which an electron may

encounter, charged impurity and phonon scattering. For convenience and brevity we assume a parabolic band approximation throughout the remainder of this chapter.

1.6.1. *Phonon Scattering*

The periodic potential associated with the crystal lattice is derived assuming the lattice is static. In practise, thermal energy will cause the semiconductor lattice to vibrate slightly; these vibrations are quantised and named phonons. It is useful to define a phonon by its wave vector $\mathbf{q}$ and its angular frequency of oscillation ω_q. In the same way that an electron with wave vector $\mathbf{k}$ can be shown to have a momentum $\hbar\mathbf{k}$ it can be shown that a phonon with wave vector $\mathbf{q}$ has a momentum of $\hbar\mathbf{q}$. The energy of a phonon can be described according to its angular frequency, $\mathrm{E}_{\mathbf{q}} = \hbar\omega_{\mathbf{q}}$. Momentum and energy conservation laws must be applied to any interaction between an electron and phonon, such that:-

$$\mathrm{E}_{\mathbf{k}'} = \mathrm{E}_{\mathbf{k}} \pm \hbar\omega_{\mathbf{q}} \tag{1.14}$$

and

$$\hbar\mathbf{k}' = \hbar\mathbf{k} \pm \hbar\mathbf{q} \tag{1.15}$$

As the above equations suggest, there are two possible electron-phonon interactions. The electron can gain energy and momentum from a phonon, this is known as phonon absorption; alternatively the interaction between the crystal lattice and an electron can lead to a phonon being produced, this is known as phonon emission. Electron phonon interactions are one of the dominant scattering mechanisms in sub-micron semiconductor devices [18].

Non Polar Optical Phonons (NPOPs)

Optical phonons are produced when two atoms in the unit cell oscillate in different directions. When an optical phonon is present the lattice spacing, and hence the periodic potential, are affected directly. If an electrons trajectory is altered by this change in potential it is said to have been scattered by a Non-Polar Optical Phonon, also known as Optical Deformation Potential (ODP) scattering. The amount by which a lattice displacement will affect an electron is given by the materials optical deformation potential, D_0.

The matrix element for NPOP scattering is given as, [19]

$$| H_{\mathbf{k'k}} |^2 = \frac{D_0^2 \hbar}{2\rho\Omega\omega_q}\left(n_{\omega_q} + \frac{1}{2} \mp \frac{1}{2}\right)\delta_{\mathbf{k'},\mathbf{k}\pm\hbar\mathbf{q}} \qquad 1.16$$

where ρ is the material density, n_{ω_q} is the phonon occupation number, Ω is the volume of the crystal and $\mathbf{q}$ is the phonon wave vector. The optical phonon energy

is almost constant as a function of the phonon wave vector and so the phonon frequency, $\omega_{\mathbf{q}}$, is assumed to be constant and is replaced by ω_0 [18]. This can then be substituted into Fermi's Golden rule to give the scattering rate [18],

$$W(\mathbf{k}) = \frac{\pi D_0^2}{\rho\omega_0}\left(n_{\omega_0} + \frac{1}{2} \mp \frac{1}{2}\right) N(E_{\mathbf{k}} \pm \hbar\omega_0) \qquad 1.17$$

Where $N(E_{\mathbf{k}} \pm \hbar\omega_0)$ is the density of electron states given by

$$N(E_{\boldsymbol{k}}) = \frac{(2m^*)^{\frac{3}{2}}\sqrt{E_{\boldsymbol{k}}}}{4\pi^2\hbar^3} \qquad 1.18$$

And n_{ω_0}in this case is the number of non-polar optical phonons given by

$$n_{\omega_0} = \frac{1}{e^{\frac{\hbar\omega_0}{k_B T_L}} - 1} \qquad 1.19$$

Where T_L is the lattice temperature. The energy of an optical phonon, $\hbar\omega_0$, is comparable to the thermal energy of electrons at room temperature and so n_{ω_0} can be represented as,

$$n_{\omega_0} \sim \frac{k_B T_L}{\hbar\omega_0} \qquad 1.20$$

Physically this means that any interaction cannot be treated elastically. Two scattering mechanisms exist within equation 1.17, represented by the dependence of $W(\mathbf{k})$ on $E_{\boldsymbol{k}} \pm \hbar\omega_0$ and $n_{\omega_0} + \frac{1}{2} \mp \frac{1}{2}$. The upper scenario represents NPOP absorption while the lower represents NPOP emission.

It is possible for an electron to transfer between valleys as a result of an optical scattering event [18]. A large momentum change is required for the inter-valley transfer which means only phonons with a wave vector close to the zone boundary can contribute to inter-valley transfer. The energy of the optical phonons near the zone boundary is slightly less than the energy of the phonons in the zone centre ($\hbar\omega_0$), and so we give them a separate energy value ($\hbar\omega_{ij}$). The NPOP inter-valley scattering rate then becomes separate from the intravalley rate shown above and must then be re-derived. The NPOP inter-valley scattering rate for an electron transitioning from valley i to valley j is given by, [18]

$$W(\mathbf{k}) = \frac{\pi D_{ij}^2 Z_j}{\rho\omega_{ij}} \left(n_{w_{ij}} + \frac{1}{2} \mp \frac{1}{2} \right) N\left(E_{\mathbf{k}} \pm \hbar\omega_0 - \Delta E_{ji} \right) \qquad 1.21$$

Where D_{ij} is the intervalley deformation potential, Z_j is the number of final valleys available for scattering, $\Delta E_{ji} = E_j - E_i$ the energy difference between the bottom of valley i and the bottom of valley j. It is found that there is a threshold energy whereby an electron is capable of undergoing an intervalley scattering event which is

dependent on the energy difference between bands (ΔE_{ji}) and the phonon energy ($\hbar\omega_{ij}$).

Polar Optical Phonon (POP) Scattering

In polar materials like GaAs the bonds between neighbouring atoms are slightly ionic. Any lattice displacement will destroy local charge neutrality causing electric polarisation. The electric field associated with this polarisation will interfere with an electrons motion. This interaction is known as polar optical phonon scattering when associated with an optical mode displacement. The matrix element for POP scattering is given as [18],

$$| H_{\mathbf{k'k}} |^2 = \frac{e^2\hbar\omega_0}{2\epsilon_p\Omega}\frac{1}{\mathbf{q}^2}[n_{\omega_0} + \frac{1}{2} \mp \frac{1}{2}]\delta_{\mathbf{k'},\mathbf{k}\pm\hbar\mathbf{q}} \qquad 1.22$$

where $\omega_0$is the phonon frequency, e is the charge of an electron, $\frac{1}{\epsilon_p} = \frac{1}{\varepsilon_\infty} - \frac{1}{\varepsilon_s}$,$\varepsilon_\infty$is the high frequency dielectric constant and ε_s is the static dielectric constant.

The scattering rates can then be obtained as usual by inserting the matrix element and integrating over the final states N_f. In deriving the POP rate the integration is performed over all possible values of $\mathbf{q}$ which gives[18],

$$W(\mathbf{k}) = \frac{e^2\omega_0}{8\pi\varepsilon_p}\frac{k}{E_\mathbf{k}}[n_{\omega_0} + \frac{1}{2} \mp \frac{1}{2}]\ln\left(\frac{q_{max}}{q_{min}}\right) \qquad 1.23$$

where $\mathbf{q}_{\max}$ and $\mathbf{q}_{\min}$ are given by

$$\mathbf{q}_{\max} = \mathbf{k}\left|1 + \left(1 \pm \frac{\hbar\omega_0}{\mathrm{E}_{\mathbf{k}}}\right)^{\frac{1}{2}}\right|$$
$$\mathbf{q}_{\min} = \mathbf{k}\left|1 - \left(1 \pm \frac{\hbar\omega_0}{\mathrm{E}_{\mathbf{k}}}\right)^{\frac{1}{2}}\right| \qquad 1.24$$

If $\mathrm{E}_{\mathbf{k}} < \hbar\omega_0$ then $\left(1 \pm \frac{\hbar\omega_0}{\mathrm{E}_{\mathbf{k}}}\right)^{\frac{1}{2}}$ in equation 1.24 becomes unsolvable for the bottom condition. Physically, this implies threshold energy for the phonon emission process.

Acoustic Phonons

Acoustic phonons are produced when neighbouring atoms oscillate in the same direction. The strain on the lattice caused by this displacement will affect the periodic potential and hence the force acting on the electron, altering its trajectory. The amount by which a lattice displacement will affect an electron is given by the material's acoustic deformation potential, $\Xi_{i,j}$. The deformation potentials are material dependant and can be deduced by experiment.

The matrix element for acoustic scattering is given as, [18],[19]

$$|\,\mathrm{H}_{\mathbf{k}'\mathbf{k}}\,|^2 = \frac{\mathrm{q}^2\Xi^2\hbar}{2\rho\Omega\omega_{\mathbf{q}}}\left(n_{\omega_{\mathrm{q}}} + \frac{1}{2} \mp \frac{1}{2}\right)\delta_{\mathbf{k}',\mathbf{k}\pm\hbar\mathbf{q}} \qquad 1.25$$

Acoustic phonon scattering can be considered elastic since the acoustic phonon energy is much smaller than $k_B T_L$, where $k_B T_L$ is the thermal energy of the lattice [18]. In cases where $\hbar\omega_{\boldsymbol{q}} \ll k_B T_L$ we can say

$$n_{\omega_{\mathbf{q}}} \sim \frac{k_B T_L}{\hbar\omega_{\mathbf{q}}} \qquad 1.26$$

This is known as equipartition and is valid at all but very low temperatures [19]. Where $\hbar\omega_{\mathbf{q}}$ is the energy of the phonon at $\mathbf{q}$. Equation 1.26 hence shows how many phonons are needed to account for the thermal energy of the lattice. The above is substituted into the matrix element which is then put into Fermi's golden rule which can be solved to give [18],

$$W(\mathbf{k}) = \frac{2\pi\Xi^2 k_B T_L}{\hbar\rho v_{sL}^2} N(E_{\mathbf{k}}) \qquad 1.27$$

Where T_L is the lattice temperature, v_{sL} is the longitudinal sound velocity and $N(E_{\mathbf{k}})$ is the density of states given previously in equation 1.18 [18].

The acoustic scattering rate increases with electron energy due to its dependence on the density of states which increases with electron energy.

1.6.2. *Piezoelectric Scattering*

It is convenient to describe piezoelectric scattering as the acoustic equivalent of POP scattering since it is the resulting electric field of the elastic strain on the

lattice caused by an acoustic phonon, rather than an optical phonon. The matrix element for piezoelectric scattering is given as, [19]

$$| H_{\mathbf{k'k}} |^2 = \frac{e^2 K_{av}^2 \hbar}{2\epsilon_p{}^2 \rho \Omega \omega_{\mathbf{q}}} \left(N_{\omega_{\mathbf{q}}} + \frac{1}{2} \mp \frac{1}{2} \right) \delta_{\mathbf{k'},\mathbf{k}\pm\hbar\mathbf{q}} \qquad 1.28$$

where K_{av} is the average electromechanical coupling coefficient, dependent on material and crystal structure. For zinc blende structures

$$K_{av}^2 = \frac{e_{14}^2}{\epsilon_p} \left(\frac{12}{35 c_L} + \frac{16}{35 c_T} \right) \qquad 1.29$$

where e_{14} is the piezoelectric constant associated with zinc blende structures. And for wurtzite crystal structures, [21]

$$K_{av}^2 = \frac{1}{\epsilon_p} \left(\frac{e_L^2}{c_L} + \frac{e_T^2}{c_T} \right) \qquad 1.30$$

where c_L and c_T are the longitudinal and transverse spherical elastic constants, e_{14} is the zinc blende piezoelectric constant and $e_L$and e_T are given by, [21]

$$e_L^2 = \frac{e_{33}^2}{7} + \frac{4e_{33}(e_{31} + 2e_{15})}{35} + \frac{8(e_{31} + 2e_{15})^2}{105}$$

$$e_T^2 = \frac{16e_{15}(e_{33} - e_{15} - e_{31})}{105} + \frac{2(e_{33} - e_{15} - e_{31})^2}{35} + \frac{16e_{15}^2}{35} \quad 1.31$$

where e_{15}, e_{31} and e_{33} are the wurtzite piezoelectric constants.

If equipartition and an isotropic interaction is assumed then by inserting the piezoelectric scattering matrix element into Fermi's Golden Rule it is eventually found that [21]

$$W(\mathbf{k}) = \frac{e^2 K_{av}^2 k_B T_L m^*}{4\pi\varepsilon_p \hbar^3 \mathbf{k}} \log\left(1 + \frac{8m^* E_{\mathbf{k}}}{\hbar^2 \mathbf{q}_0^2}\right) - \frac{1}{1 + \hbar^2 \mathbf{q}_0^2 / 8m^* E_{\mathbf{k}}} \quad 1.32$$

Where $\mathbf{q}_0$ is the electronic screening given by,

$$\mathbf{q}_0 = \sqrt{\frac{2m^* \omega_L}{\hbar}} \quad 1.33$$

Where ω_L is the acoustic phonon frequency. At low energies the piezoelectric scattering increases because of screening. At all but the lowest of electron energies the scattering rate slowly reduces with energy much like the POP scattering rate.

Piezoelectric scattering is not a main contributor to the total scattering rate except at very low temperatures in very pure piezoelectric semiconductors.

1.6.3. *Impurity and Dislocation Scattering*

Free electrons in a semiconductor are usually supplied by the presence of electron rich impurities or dopants. The introduction of electron rich materials will sometimes be intended as is the case of n-type doping; otherwise it is certain that an amount of undesirable material will pollute the semiconductor during growth and fabrication. When these electron rich materials are present a significant electric field is produced within the material which will disturb the flow of electrons. When electron motion is affected by such a phenomena we call it an impurity scattering event. The electric field resulting from the electron rich impurity is largely screened, depending on the amount of carriers in its vicinity [18]. The scattering rate calculation becomes quite complicated due to screening and can be evaluated using various methods. The method used for the model presented in this thesis is the Brooks-Herring approximation. Ridley [21] gives the matrix element for impurity scattering using the Brooks-Herring approximation as

$$| H_{\mathbf{k}'\mathbf{k}} |^2 = \frac{z^2 e^4}{\Omega^2 \varepsilon_s^2} \left(\frac{1}{(|\mathbf{k}' - \mathbf{k}|^2 + q_D^2)^2} \right) \qquad 1.34$$

Where $\mathbf{k}$ and $\mathbf{k}'$ are the initial and final wave vectors, Ω is the crystal volume, z is the number of impurities and q_D is the Debye length (the distance it takes for electrons to screen out the impurities' electric potential). The Debye length is given by [18]

$$q_D = \sqrt{\frac{e^2 N_D}{k_B T_L \varepsilon_s}} \tag{1.35}$$

where N_D is the material's impurity concentration.

The matrix element can then be inserted into Fermi's golden rule. On performing the integrations it is found [18]

$$W(\mathbf{k}) = \frac{2\pi N_D z^2 e^4 N(E_{\mathbf{k}})}{\hbar \varepsilon_s^2} \frac{1}{q_D^2 (4\mathbf{k}^2 + q_D^2)} \tag{1.36}$$

where $N(E_{\mathbf{k}})$ is the density of available states after scattering.

Quite counter intuitively the impurity scattering rate actually decreases as the impurity concentration increases. This can be observed mathematically by inserting the equation for the Debye length into the scattering rate equation. This shows that $W(\mathbf{k})$ is proportional to N_D and $\frac{1}{N_D^2}$. Although the scattering rate decreases with increasing impurity concentration the electron mobility decreases. The angle by which an electron scatters is bigger when screening is more dominant. Screening

increases with carrier density which in turn increases with impurity concentration causing a decrease in mobility.

Dislocation scattering

Dislocations in a semiconductor can also lead to an unwanted electric field which can interfere with an electrons motion. A dislocation arises when there is a lattice mismatch between the semiconductor compound and the material on which it is grown. The way in which semiconductors are grown varies for each material and so dislocations will affect some semiconductors more than others. $In_{0.53}Ga_{0.47}As$ for example can be grown lattice matched to InP which will reduce the amount of dislocations within the material. If a different amount of Indium or Gallium is used to form the compound then the lattice formation will be different. In this circumstance a new growth material could be found to match the new lattice spacing, or InP could be used and the number of dislocations would increase.

Dislocation scattering is a two dimensional scattering event. What happens to an electron during scattering depends on the angle between the electron and dislocation. If an electron encounters a dislocation and its path is parallel to the dislocation plane the electron will continue mostly uninterrupted, whereas if an electron encounters a dislocation orthogonal to the electron path, scattering may occur. Since the simulations described in the following section are mainly

considering only one spatial dimension this scattering mechanism is not explored further.

1.6.4. *Scattering rates in GaN and $In_{0.53}Ga_{0.47}As$*

Scattering rates can vary quite significantly between materials. The materials which are being investigated in this thesis are GaN and $In_{0.53}Ga_{0.47}As$. The scattering rates as a function of electron energy at 300K are presented for GaN in Figure 1.3 and for $In_{0.53}Ga_{0.47}As$ in Figure 1.4. In GaN the POP scattering rate is clearly the dominant rate until electrons reach higher energies when intervalley scattering takes its place. While in $In_{0.53}Ga_{0.47}As$ impurity scattering is dominant at lower energies until POP scattering becomes equally dominant. Finally, at large electron energies intervalley scattering becomes the dominant mechanism. Having knowledge of the scattering rates for each material is invaluable when analysing electron transport in either of these materials. The material parameters used to calculate each of the scattering rates can be found in the table below.

Parameter (units)	$In_{0.47}Ga_{0.53}As$	GaN
Density (kg/m^3)	5500	6150
Impurity Concentration (cm^{-3})	1×10^{16}	1×10^{16}
Longitudinal sound velocity (ms^{-1})	4740	7641
Transverse sound velocity (ms^{-1})	2690	4110
Non-polar optical deformation potential coupling constant (eV/m)	10^{11}	10^{11}
Intervalley scattering coupling constant (eV/m)	10^{11}	10^{11}
Acoustic deformation potential (eV)	9.2	8.3
Piezoelectric constant e_{14} (Cm^{-2})	-0.09905	-
Piezoelectric constant e_{15} (Cm^{-2})	-	-0.3
Piezoelectric constant e_{31} (Cm^{-2})	-	-0.36
Piezoelectric constant e_{33} (Cm^{-2})	-	1
Energy gap (eV)	0.77	3.39
Energy separation between L / M-L and Γ valley (eV)	0.46	1.2
Energy separation between X / A and Γ valley (eV)	0.59	2.1
Number of equivalent L / M-L valleys	4	6
Number of equivalent X / A valleys	3	6
Effective mass in Γ valley (m_0)	0.041	0.2
Effective mass in L / M-L valley (m_0)	0.29	1
Effective mass in X / A valley (m_0)	0.68	1
Polar optical phonon energy (eV)	0.0327	0.0912
Lattice constant (Å)	5.8687	5.186

Table 1.1 – Material parameters for $In_{0.47}Ga_{0.53}As$ at 300K [27][28] and GaN at 300K [19], [29]–[34].

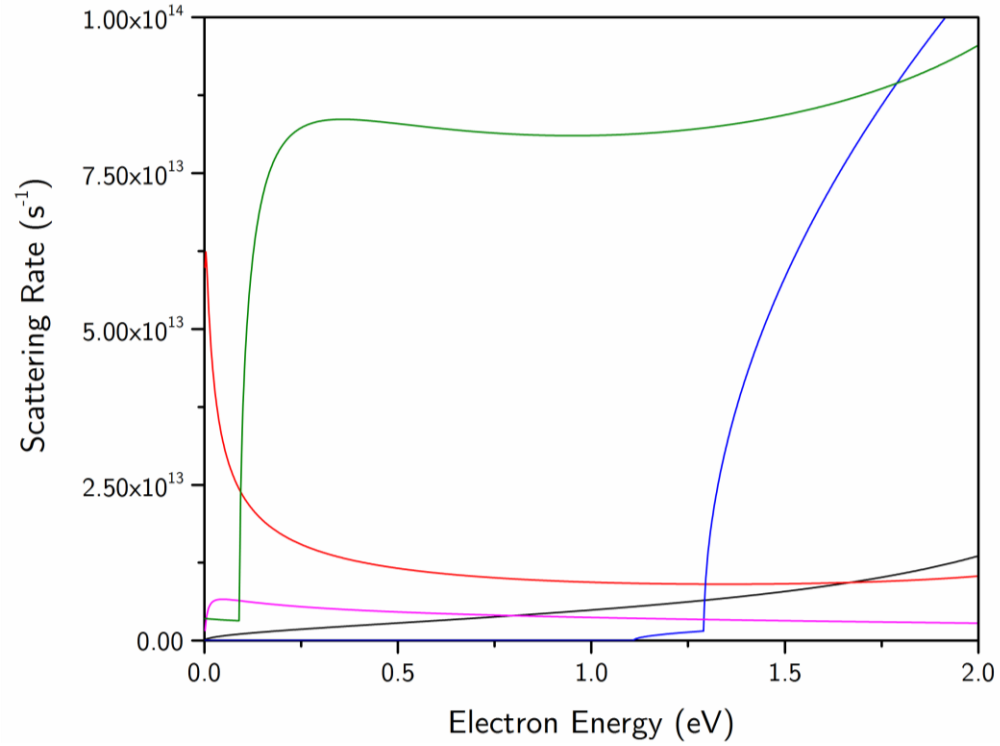

Figure 1.3 – Acoustic (black), impurity (red), intervalley (blue), piezoelectric (pink) and POP (green) scattering rates as a function of electron energy for GaN.

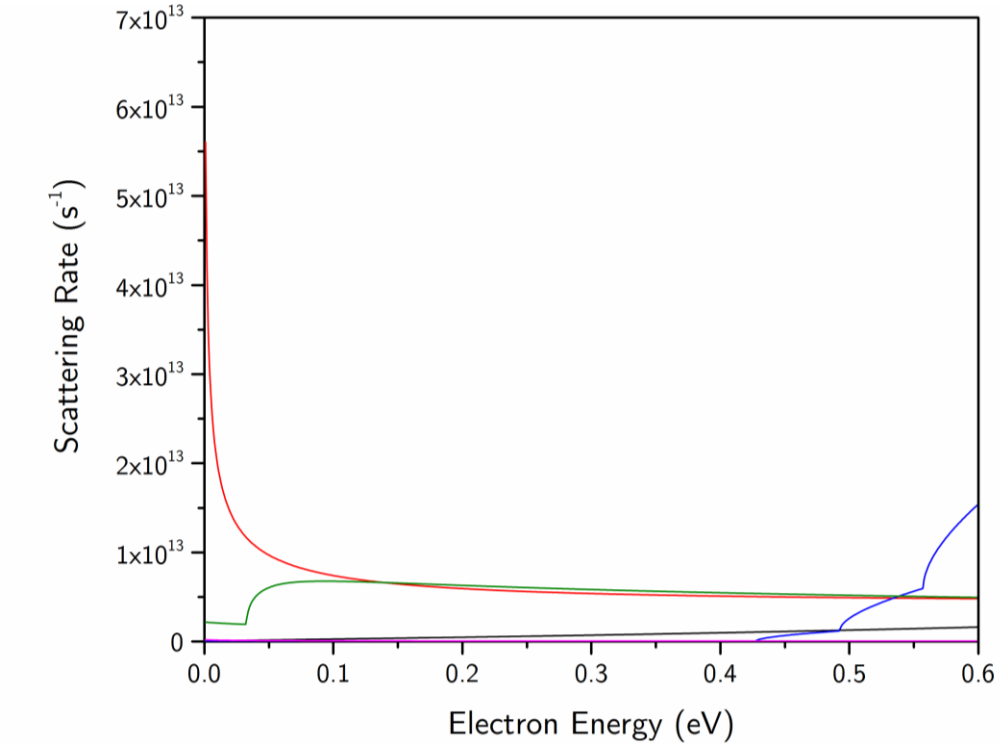

Figure 1.4 – Acoustic (black), impurity (red), intervalley (blue) piezoelectric (pink) and POP (green) scattering rates as a function of electron energy for $In_{0.53}Ga_{0.47}As$.

1.7. Gunn Effect

The large band gap, high break-down field and high electron mobility of many III-V and III-nitride semiconductors have made them the subject of research for use in high-frequency, high temperature and high power device applications. These materials also exhibit a negative differential mobility [35]. A combination of work by Kroemer, Hilsum, Ridley and Watkins explained how Negative Differential Mobility (NDM) could lead to highly inhomogeneous charge distributions and electric fields within two-terminal devices [36]. These effects can be utilised to create a group of devices known as Transferred Electron (TE) devices; one such device is known as the Gunn diode. Gunn diodes are two terminal devices which are generally made up of an intrinsic or lightly doped piece of semiconductor, sandwiched between n-doped materials, with contacts attached to the ends of the n-doped material (see Figure 1.5).

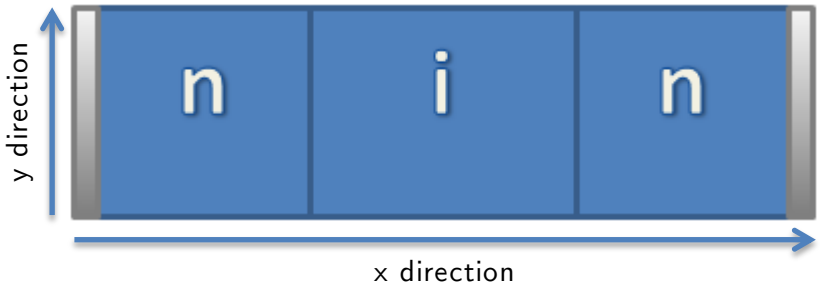

Figure 1.5 – A representation of a typical Gunn device.

When Gunn measured the voltage-current characteristics of n-doped GaAs he found that when the applied electric field (F) was greater than a critical value,

$$F = \frac{\varphi}{L} \qquad 1.37$$

(where φ is the applied potential and L is the sample length) microwave oscillations appeared which could be related to the transit times of electrons through the sample [37]. By measuring the potential distribution across the device Gunn found that high field domains were being formed within the device which nucleate near the cathode, propagate across the device at around the saturation velocity specific to the material, and annihilates at the anode. Once the domain has annihilated at the anode the process was then observed to repeat itself [35].

In order to fully explain how domains of high electron concentration are formed within a Gunn diode it is necessary to examine the relationship between average electron velocity (v) and electric field (F). The velocity of an electron within a semiconductor is dependent upon the applied electric field. In many III-V and III-Nitride materials there is a region in this relationship where an increase in electric field produces a reduction in average electron velocity producing a negative differential mobility (μ_d).

$$\mu_d = \frac{dv}{dF} \qquad 1.38$$

The electric field which results in the maximum average electron velocity is known as the critical field, the corresponding velocity is called the peak velocity, while the steady state velocity at high field is known as the saturation velocity. If we assume that a field higher than the critical field is applied across the active region of a device so that it is operating within the Negative Differential Resistance (NDR) region of the velocity-field relationship; and imagine that there is a flucatuation in the field, perhaps at the interface between the anode and the active region or due to a doping irregularity, then regions of high and low field are formed. Electrons in the low field region will travel faster than those at the higher field. This can result in an accumulation of charge which grows in size as it propagates towards the anode. The cause of the initial field fluctuation determines how the charge accumulates and whether accumulation layers or dipole domains are formed. In the following sub-chapter an explanation of the criterion for domain formation is given, followed by a discussion surrounding the physical processes responsible for dipole domain and accumulation layer formation.

1.7.1. *Kroemer Criteria*

For continuous and stable Gunn operation to be possible a number of conditions are required, many of which are material dependent. It is required that the initial growth time of the fluctuation (t_{gr}) is considerably smaller than the time it takes for the accumulation to propagate across the device, known as transit time (T)

[35]. Electrons within the charge accumulation create an area of high field meaning they will generally be travelling at around the saturation velocity [35]. The domain transit time is then given by:

$$T \sim \frac{L}{v_s} \tag{1.39}$$

Where L is the length of the active region and v_s is the saturation velocity. The transit time of charge accumulations or Gunn domains determines the operating frequency of the Gunn device. By using a smaller active region the transit time can be reduced and the operating frequency is hence increased. Smaller devices must be driven by a smaller potential compared to larger devices to avoid reaching breakdown field. In order to increase operating frequency it hence becomes desirable to use a material with a high breakdown field and a large saturation velocity.

The domain growth time (t_{gr}) is determined by the differential dielectric relaxation time (τ_{ddr}) of the material. The domain growth time must be larger than the dielectric relaxation time for domains to form and so it is shown that,

$$t_{gr} \sim |\tau_{ddr}| = \frac{\varepsilon_r \varepsilon_0}{q|\mu_d| n_0} \tag{1.40}$$

Where μ_d is the differential mobility of the NDR region and n_0 is the doping density of the active region. Using this expression we find that to ensure the formation of

stable propagating domains the following so-called Kroemer criteria must be met [38]:

$$n_0 L > \frac{\varepsilon_r \varepsilon_0 v_s}{q|\mu_d|} \tag{1.41}$$

It is widely recognised that domain growth lasts for at least 3 x τ_{ddr} [5][35] and so the Kroemer criterion is often given as,

$$n_0 L > \frac{3\varepsilon_r \varepsilon_0 v_s}{q|\mu_d|} \tag{1.42}$$

The $n_0 L$ product for each simulated device in the relevant results chapters appears in the device parameters table for comparison with the Kroemer criteria.

1.7.2. *Accumulation mode*

When devices operate in accumulation mode there is a clear build-up of charge which grows in size as it propagates across the active region towards the anode. The formation of accumulation layers is caused by a sharp dip in electric field, that that shown in the inset in Figure 1.6. If a field fluctuation like that shown in the inset in Figure 1.6 is assumed, the electrons occupying the device position at F_1 will, according to the velocity-field characteristics, have a higher average velocity compared to electrons in front and behind it at F_2. If the field profile presented in the inset in Figure 1.6 is static, perhaps due to the over-riding effects of the doping

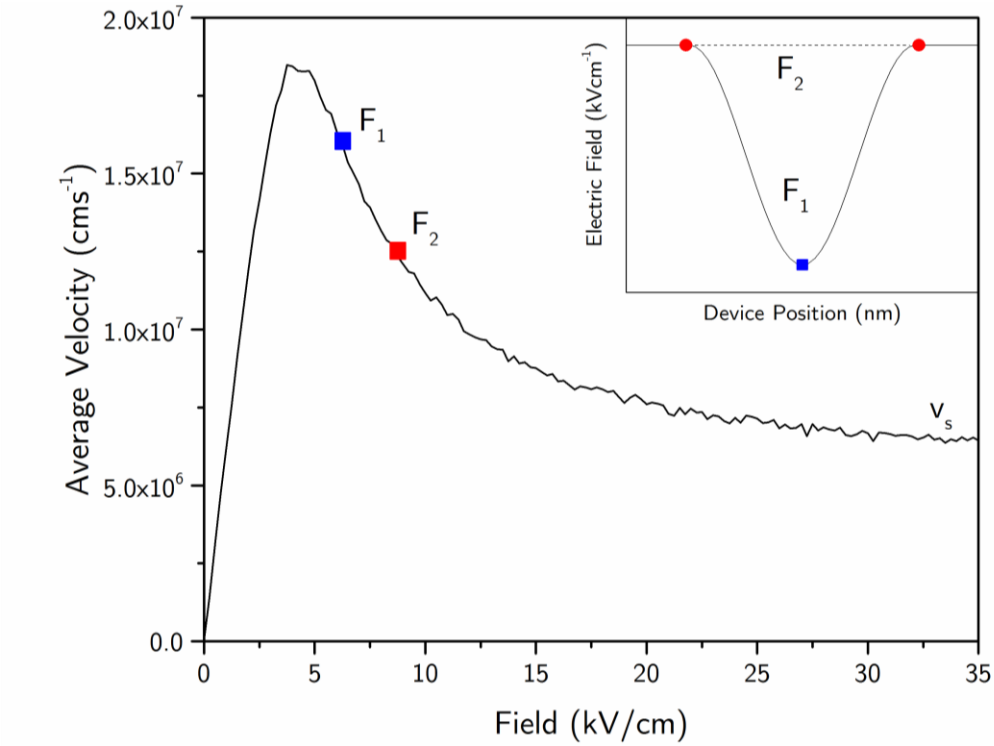

Figure 1.6 – Velocity field characteristics for bulk GaAs. The accompanying inset and labelled data points portray an example scenario leading to the formation of an accumulation layer.

profile of the device, then as the localised group of electrons travel forward at an increased velocity they will accumulate the charge in front. The accumulation layer then splits the active region into two distinct regions, a region of high field between the layer and the anode and a region of low field between the layer and the cathode. As the layer propagates across the active region the faster moving electrons at the cathode side of the layer will begin to join the accumulation. This effect causes an increase in the amount of charge accumulating in the layer which leads to a further increase in field at the expense of the region behind the charge accumulation. Accumulation layers generally have a gradually falling edge on the

cathode side of the domain caused by electrons joining the accumulation in contrast to the sharp gradient at the leading edge.

1.7.3. *Dipole mode*

To aid in the explanation of dipole domain formation let's assume that the average electric field across a two terminal device is higher than the critical field and within the NDR region of the velocity-field curve. If a small fluctuation in electric field is present near the cathode of the device, or at the interface between the contacts and the active region, then according to the velocity-field characteristics there will be differing electron velocities around the field fluctuation (see Figure 1.7). If the fluctuation in field manifests as a significant localised increase in electric field then the electrons interacting with the higher field at the fluctuation will have a lower velocity than those in front and behind the fluctuation. The increase in velocity for electrons in front of the fluctuation relative to the velocity of electrons within the fluctuations leads to a region of charge depletion in front of the fluctuation; while the increased velocity of electrons before the fluctuation leads to an accumulation of electrons. This accumulation and depletion of charges further increases the inhomogeneity of the electric field which results in a growing dipole domain which propagates towards the anode. A localised increase in electric field can be created within a device using a doping notch between the N++ cathode region and the

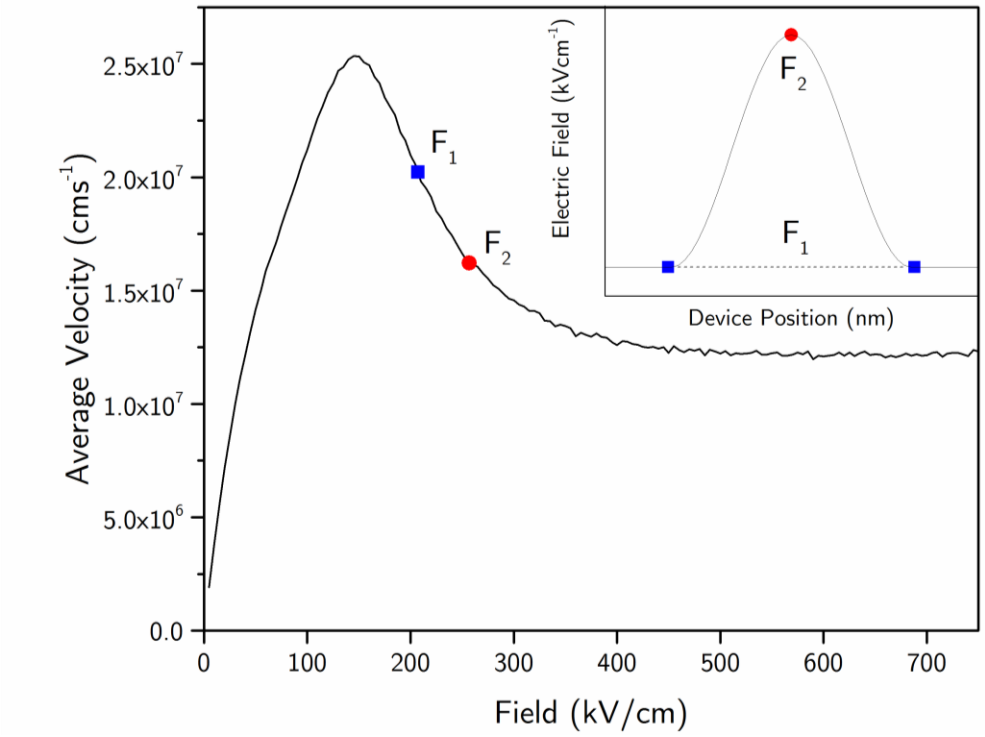

Figure 1.7 Velocity field characteristics for bulk GaAs. The accompanying inset and labelled data points portray an example scenario leading to the formation of dipole domain.

active region. Results for a GaN device with a doping notch is presented later in this thesis.

1.7.4. *Stationary anode domain*

In samples with a doping density above some critical value ($n_0 > n_{cr}$) and a constant, large applied potential, a stationary domain may appear near the anode [39][35]. For a device to operate with a stationary anode domain the field outside of the stationary domain must be smaller than the field required for domain formation. Under these circumstances a new domain cannot form, instead electrons continuously join the stationary domain so that it does not fully annihilate.

Stationary anode domains have been observed experimentally by Heinle [40]. When a stationary anode domain forms, an oscillating current is not present and so is not a desirable operating regime for Gunn oscillating devices. To avoid operating in the stationary anode regime a time varying potential is often applied. As the potential drops the domain begins to disperse and so the field reduces where the domain was previously present. It is then possible for the electric field to increase beyond threshold in other parts of the device when the potential increases again.

1.7.5. *Operating frequency*

With a constant applied bias the increase in electric field resulting from the growth of the charge accumulation or dipole domain comes at the expense of the field in the rest of the device. This reduction in electric field leads to a current drop during domain formation [35]. When the domain annihilates at the anode a temporary increase in current can be observed. The operating frequency (f) is hence dependant on the transit time (T) of the domain or charge accumulation according to [35],

$$f = \frac{1}{T} \sim \frac{v_s}{L} \qquad 1.43$$

Where L is the length of the active region and v_s is the saturation velocity.

The shape of the current waveform is then dependent on annihilation time and domain growth time. A wider or more slowly moving accumulation of charge will

take a longer time to fully annihilate at the anode resulting in a less sharp increase in current with time compared to a sharp, thin accumulation of charge with a high drift velocity. The domain growth time in turn affects how the current reduces with time. The slower the domain grows the less the current will be reduced with time. These effects mean current waveforms can have very different characteristics and can depend on operating regime, material and device design. Current waveforms specific to particular devices are explored as part of the results chapters within this thesis.

1.8. Outline of Thesis

Three Monte Carlo models have been used to gather the results for this thesis. Each model is based around the Ensemble Monte Carlo (EMC) method. An EMC model was originally developed to study electron transport in bulk materials and was used by Naylor et al. to investigate steady-state and transient transport properties in bulk GaN [22]. The EMC has since followed three distinct development routes. The first development route enables the EMC to investigate hot phonon effects in bulk materials. The second development route allows the simulation of 1-dimensional electronic devices, while the third allows simple 2-dimensional electronic devices to be simulated. Significant modifications to the original EMC model are required for each of these development routes. In the next chapter the EMC model is described

in detail. The modifications applied to the EMC model for each development route are significant and so are presented in individual sub-chapters.

The hot phonon model has been used by Dyson et al. to investigate hot phonon effects in GaN and AlN in [41]. $In_{0.53}Ga_{0.47}As$ is used for fabricating both electronic and photovoltaic devices. InGaAs channel Metal-Oxide-Semiconductor Field-Effect Transistors (MOSFETs) for example, are considered to be the most promising non silicon devices for next generation nanoscale CMOS technology [42]. Hot phonons are thought to be a responsible, at least in part, for reduced device performance and device degradation. The hot phonon model used by Dyson et. al in [41] has been used to investigate hot phonon effects in $In_{0.53}Ga_{0.47}As$ as part of this thesis; results are presented in Chapter 3.

In Chapter 4 the 1-dimensional device model is used to simulate vertical GaAs Gunn diodes. A lot of the modelling work surrounding GaAs Gunn devices was completed with relatively primitive computing power. Results from Tully [1] are re-created using a finer mesh and a larger number of superparticles. The characteristics of the new model are analysed and compared with the original publication. In Chapter 5 GaN Gunn diodes are investigated. In 2000 Pavlidis et al. [6] fabricated the first GaN NDR diode. The GaN device was shown to operate at almost double the frequency of a GaAs with the same active layer thickness and had a significantly higher output power. A GaN Gunn device operating in accumulation mode is

presented along with a device operating in dipole mode. These simulations employ an intervalley separation half of that used in the other works at 1.2eV. This value reflects the most recent experimental determination of this critical parameter [34]. In Chapter 6, results from the 2-dimensional model are presented. The device operating in accumulation mode presented in Chapter 5 is simulated with an extra dimension. Results from the 1-dimensional model and the 2-dimensional model are compared to ensure validity of the 2-dimensional model. Finally, in Chapter 7 the thesis draws conclusions from this work and discusses the potential for further development of the models which have been presented.

Chapter 2. Monte Carlo methods for simulating electron transport.

Monte Carlo simulations are computational algorithms which rely on many stochastic events to produce results. When using Monte Carlo methods to simulate electron transport electron free flight times and scattering events are determined using random numbers. Depending on the state of the system the probability of scattering and hence free flight time will change. By simulating a large number of events a realistic picture of how electrons behave when travelling through a semiconductor is produced.

The following chapter begins with an overview of how an Ensemble Monte Carlo (EMC) model works. The EMC model which is discussed in the following section is used as a base model from which further developments have been made. The basic EMC model has been developed further so that hot phonon effects can be investigated. A separate development route has also been pursued so that semiconductor devices can be modelled. The modifications required to investigate

hot phonon effects and semiconductor devices are significant and so the alterations required for each model are discussed in individual sub-chapters.

2.1. Ensemble Monte Carlo method

The EMC method simulates a large number of independent carriers (electron-electron interactions are not included) as they travel through a semiconductor material. The EMC simulates the movement of a number of electrons individually across a specific time step before allowing the simulation to run for the next time step. This is important as it allows the average behaviour of the system to be represented as a function of simulation time. To ensure a high level of precision the size of the time step is chosen so that any change in electron energy over a whole time step is small. The EMC can be used to study both steady state and transient behaviour. A flowchart depicting the structure of the simulation is presented in Figure 2.1.

Firstly, the Parameter sub routine pre-calculates the scattering rates for a range of electron energies. Each scattering rate is recorded in a scattering table for a range of chosen energy increments. These tables are then used throughout the simulation to determine an electrons free flight time and in the selection of a scattering event.

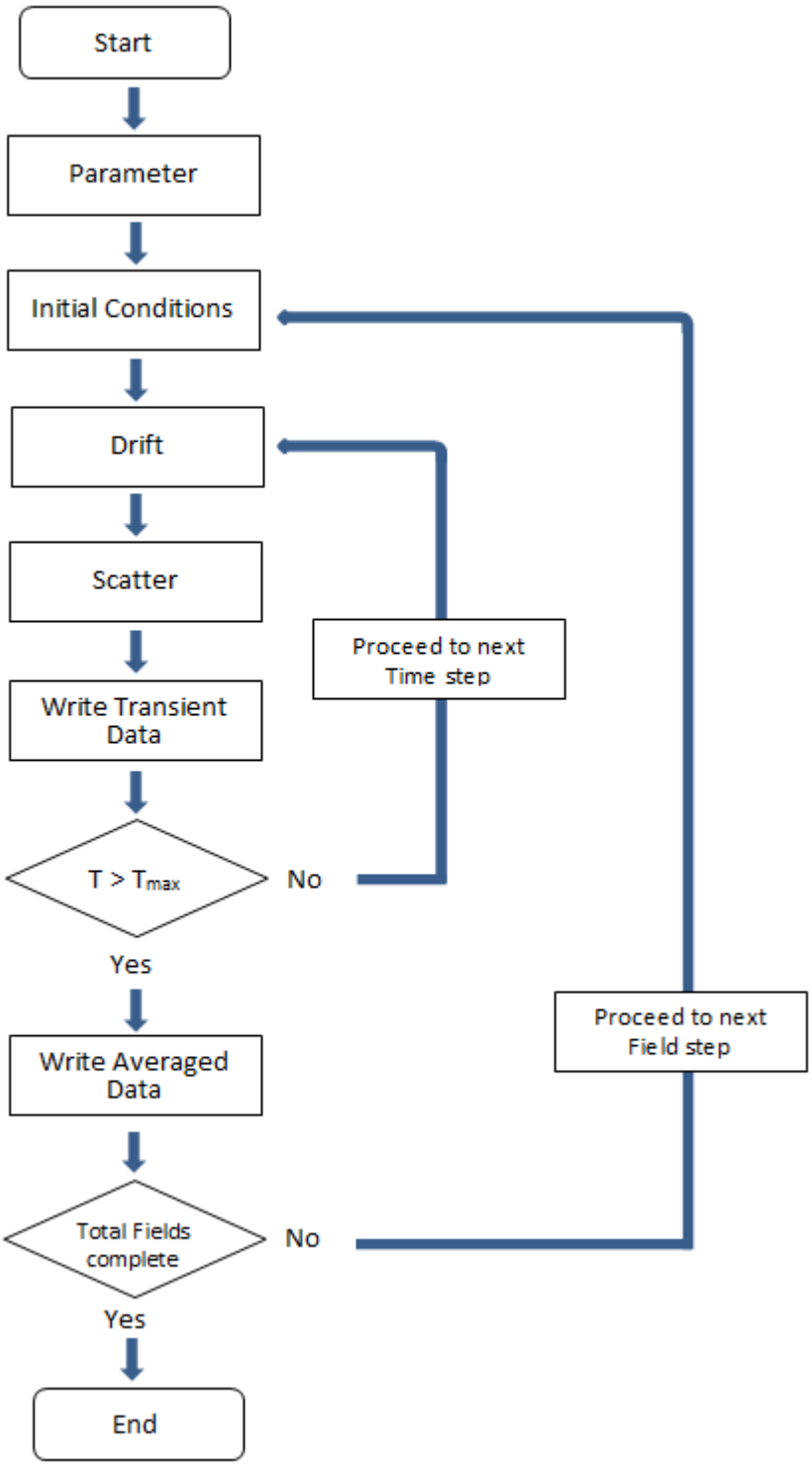

Figure 2.1 – Flowchart representing the basic model of an EMC used for simulating electron transport.

The probability per unit time, $P(\tau)$, of an electron traveling for a time τ and being scattered at the end of this time is given by [18]

$$P(\tau) = W_T(E_{\mathbf{k}}) \exp\left[-\int_0^{\tau} W_T(E_{\mathbf{k}})dt\right] \quad 2.1$$

where $W_T(E_{\mathbf{k}})$ is the total scattering rate for a given energy $E_{\mathbf{k}}$.

Since the electrons within the system will all have variable amounts of energy they will have a different probability of scattering and hence a different free flight time. It becomes convenient and computationally efficient to introduce a virtual scattering mechanism known as self-scattering [18]. Self-scattering is not a physical scattering mechanism, it is introduced in order to simplify equation 2.1. If it an electron is 'self-scattered' its properties will not be changed and the electron will be allowed to continue its drift as normal meaning the introduction of self-scattering for numerical convenience will not have an effect of electron behaviour. The self-scattering rate is chosen for each individual energy increment so that the total scattering rate is the same across all energy increments. Since the total scattering rate for all energies is now constant equation 2.1 can be expressed as:

$$P(\tau) = \Gamma e^{-\Gamma\tau} \quad 2.2$$

where Γ is the total scattering rate including self-scattering.

The parameter routine then takes the cumulative scattering rate for each energy step, normalises the total rate, and attaches a weighting for each scattering mechanism on the cumulative scale. When an electron scatters the appropriate scattering table is selected according to the electron energy and a scattering mechanism is selected from the weighted scattering table using a random number. The energy increment, ΔE is chosen such that the scattering rates differ only very slightly between energy E_1 and the next energy $E_1 + \Delta E$. By using self-scattering the expression for free flight time (discussed later) is the same for all electron energies which improves computational performance.

The Initial Conditions sub routine then defines the initial wave vector, direction of travel and initial free flight time of each electron in the system based on random numbers. A range of electron energies are also assigned at random, weighted according to the user-defined lattice temperature. All electrons are set to initially occupy the gamma valley. The initial electron $\mathbf{k}$ vector magnitude is determined from the energy distribution and is divided into k_x, k_y and k_z according to a random initial direction.

Within the Monte Carlo code the two sub routines Drift and Scatter work closely together. The drift routine uses a random number, r_1, between 0 and 1and the reciprocal of the total scattering rate to calculate a random free flight time τ:

$$\tau = -\frac{\ln(r_1)}{\Gamma} \tag{2.3}$$

where Γ is the total scattering rate, including self-scattering and r_1 is a random number between 0 and 1.

The sub routine Scatter uses a random number to determine a scattering mechanism from the scattering table and calculates the change in energy and wave vector before updating the simulation time to $t + \tau$. Drift is then called again to allow the electron to drift for the rest of the time step (assuming it does not scatter again). This process is repeated for each electron for the current time step before any electron is allowed to proceed to the next time step. Each electron is treated independently which means the drift and scattering of individual carriers can be calculated in parallel, significantly decreasing simulation time. Alternatively, if different applied fields are being investigated it is more efficient to run each applied field in parallel.

2.1.1. *Anisotropic scattering*

POP scattering is anisotropic so an equation is required that allows us to determine the angle between an electrons path before and after scattering. The probability of scattering between 0 and θ` can be found by dividing W(**k**) by W(θ`). This can be expressed as:

$$\frac{W(\theta`)}{W(\mathbf{k})} = \frac{\ln\left(\frac{\mathbf{q}_{\theta'}}{\mathbf{q}_{min}}\right)}{\ln\left(\frac{\mathbf{q}_{max}}{\mathbf{q}_{min}}\right)} \qquad 2.4$$

where θ` is the polar angle between **k** and **q**, illustrated in Figure 2.2.

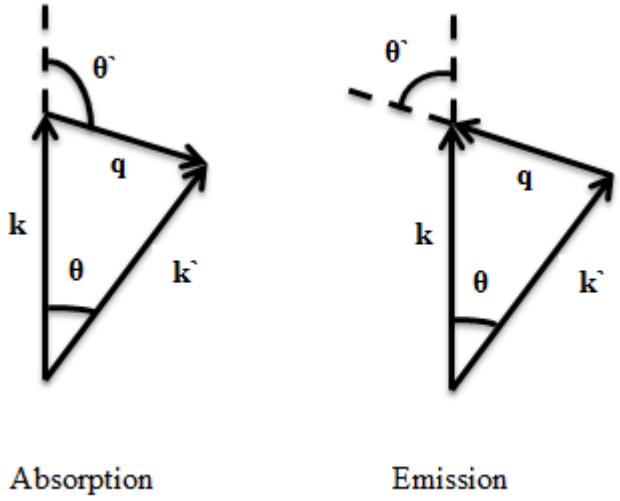

Figure 2.2 – Definition of the polar angle θ`.

The probability of scattering between 0 and θ` $\left(\frac{W(\theta`)}{W(\boldsymbol{k})}\right)$, lies between 0 and 1. Equation 2.4 can be equated to a random number (r) distributed between 0 and 1

and then used in Monte Carlo simulations, to generate a scattering angle stochastically; such that

$$r = \frac{\ln\left(\frac{\mathbf{q}_\theta}{\mathbf{q}_{min}}\right)}{\ln\left(\frac{\mathbf{q}_{max}}{\mathbf{q}_{min}}\right)} \qquad 2.5$$

The angle in the Monte Carlo model used for this thesis is θ rather than θ` and so we must solve equation 2.4 in terms of θ. We express the scattering angle probability in terms of $\mathbf{k}$, $\mathbf{k}'$ and cosθ using:

$$\mathbf{q}_\theta^2 = \mathbf{k`}^2 + \mathbf{k}^2 - 2\mathbf{k`k}\cos\theta \qquad 2.6$$

$\mathbf{q}_{min}$ and $\mathbf{q}_{max}$ can be obtained by setting θ equal to 0 and π such that

$$\mathbf{q}_{min}^2 = \mathbf{k`}^2 + \mathbf{k}^2 - 2\mathbf{k`k}$$
$$\mathbf{q}_{max}^2 = \mathbf{k`}^2 + \mathbf{k}^2 + 2\mathbf{k`k} \qquad 2.7$$

Substituting equations 2.6 and 2.7 into equation 2.5 it is found that [18]:

$$\cos\theta = \frac{1 + f - (1+2f)^r}{f} \qquad 2.8$$

Where $0 \leq r \leq 1$ to cover all possible values of $\cos\theta$ (r can be generated stochastically to provide a random scattering angle as part of the Monte Carlo

simulation) and f is a function of the electron energy before and after scattering, given as

$$f = \frac{2\sqrt{E_{\mathbf{k}}E_{\mathbf{k}'}}}{\left(\sqrt{E_{\mathbf{k}}} - \sqrt{E_{\mathbf{k}'}}\right)^2} \tag{2.9}$$

This dependence of scattering angle on electron energy must be considered when analysing the effects of electron-phonon interactions on carrier transport.

2.1.2. *Output*

At the end of each time step (or every x time steps) the simulation will record various characteristics of the electrons within the simulated system, notably average electron energy and velocity, energy and velocity distributions and valley occupancy. The average electron velocity in the direction of the applied field, during flight time T, is expressed mathematically as:

$$\langle v \rangle_T = \frac{1}{n}\sum_{a=1}^{n} \frac{1}{\hbar}\frac{\delta E(\mathbf{k})_a}{\delta \mathbf{k}_{x,a}} \tag{2.10}$$

While the average electron energy is expressed as:

$$\langle E(\mathbf{k}) \rangle_T = \frac{1}{n}\sum_{a=1}^{n} E(\mathbf{k})_a \tag{2.11}$$

Where n is the total number of particles within the simulation, $E(\mathbf{k})$ is the energy of an electron with wave vector $\mathbf{k}$ and $k_x$is the electron wave vector in the direction of the applied field. Using this data we can investigate how electron behaviour evolves with time for particular applied fields. The transient characteristics can be used to find the time it takes for the system to reach steady-state. Once the model has reached equilibrium the results for each applied field can be used to investigate steady-state transport characteristics.

2.2. Monte Carlo methods for simulating hot phonon effects

In the EMC model a static and thermal phonon population is assumed in order to derive the POP scattering rate. In reality, each time an electron emits a phonon this energy will be stored in the crystal lattice and would be available for re-absorption. As mentioned in chapter 1 a significant phonon population is likely in real electronic devices and may have a detrimental effect on electron transport characteristics. In this sub-chapter the modifications required so that hot phonon effects can be simulated using the EMC model are explained.

Hot phonon effects have been incorporated into our EMC model using the method of Jacoboni [43]. Each time an electron undergoes a POP scattering event it is recorded in a phonon occupation histogram defined over a grid in momentum space. Since the phonon distribution is no longer constant the pre-calculated POP scattering rate must be updated regularly throughout the simulation according to

the actual phonon distribution; vastly increasing the simulation time. An overview of the hot phonon simulation algorithm is presented in Figure 2.3.

After every POP scattering event the phonon wave vector must be calculated. A scattering angle is determined at random (See Equation 2.8) and the electron wave vector ($\mathbf{k}$) and phonon vector ($\mathbf{q}$) are calculated according to this angle, the initial electron energy and the phonon energy. The emitted phonons are spatially confined in momentum space, often referred to as $\mathbf{q}$-space. If we consider the field to be applied in the x-direction and the conduction band to be spherical then the y and z directions are equivalent. Phonon momentum can then be split into 2 directions, q_x and q_T . q_x is the component of the phonon momentum parallel to the field and q_T makes up the plane perpendicular to the field.

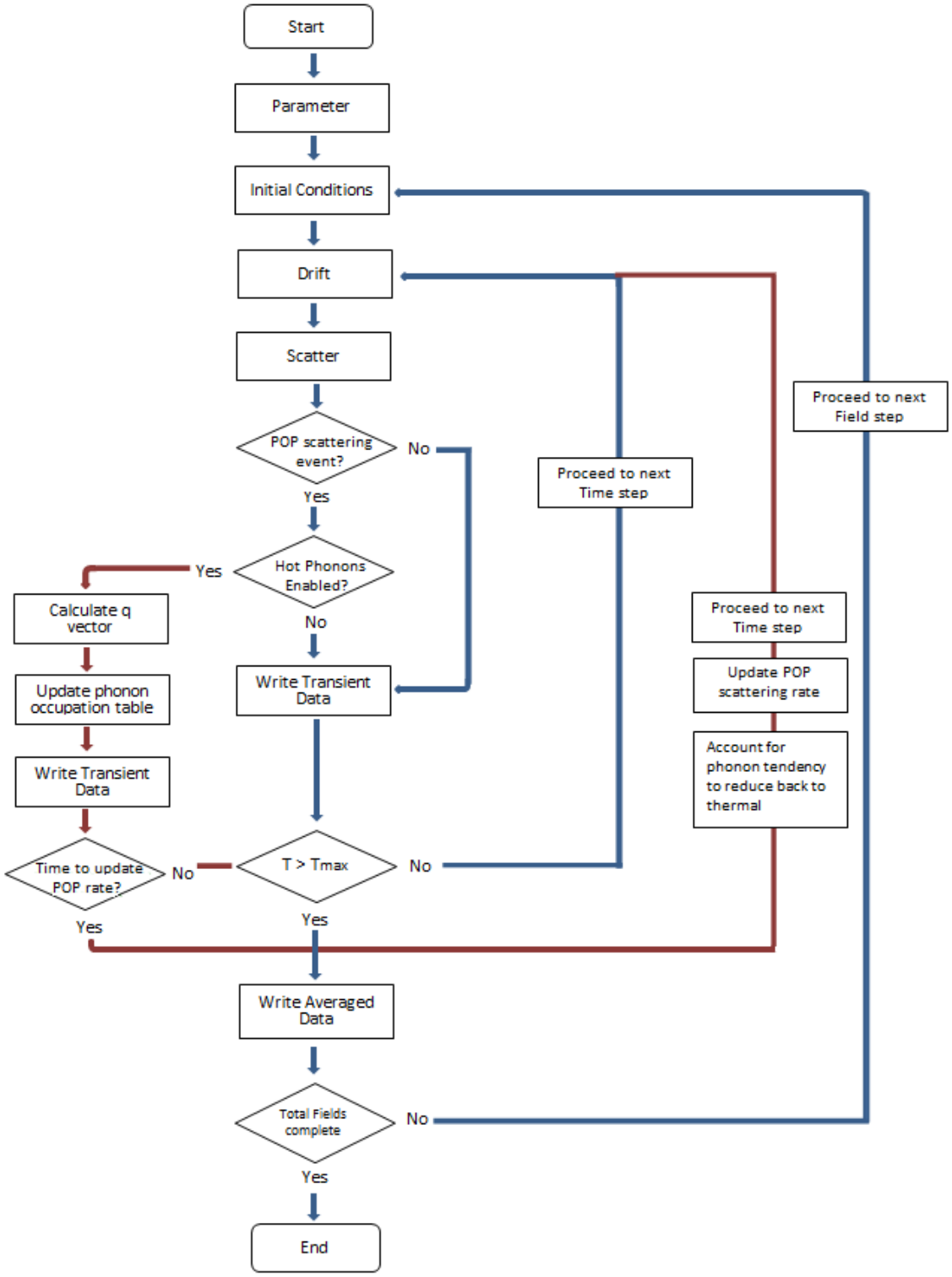

Figure 2.3 - Flowchart diagram how the Ensemble Monte Carlo algorithm can be modified to investigate hot phonon effects on electron transport.

Where:

$$q_T^2 = q_y^2 + q_z^2 \qquad 2.12$$

And

$$\mathbf{q^2} = q_x^2 + q_T^2 \qquad 2.13$$

The resultant $\mathbf{q}$-space is a set of concentric rings where each ring corresponds to a place in the phonon table (See Figure 2.4).

At fixed times $T = n\Delta t$ (where Δt is 1 time step and n is an integer) the model uses the phonon occupation table to update the POP scattering rate across a range of energies, essentially repeating the role of the parameter sub-routine as described in section 2.1. The number of time steps after which the scattering rates are to be updated and the energy range over which they are calculated are both user-defined parameters which must be tuned in order to reduce statistical instability.

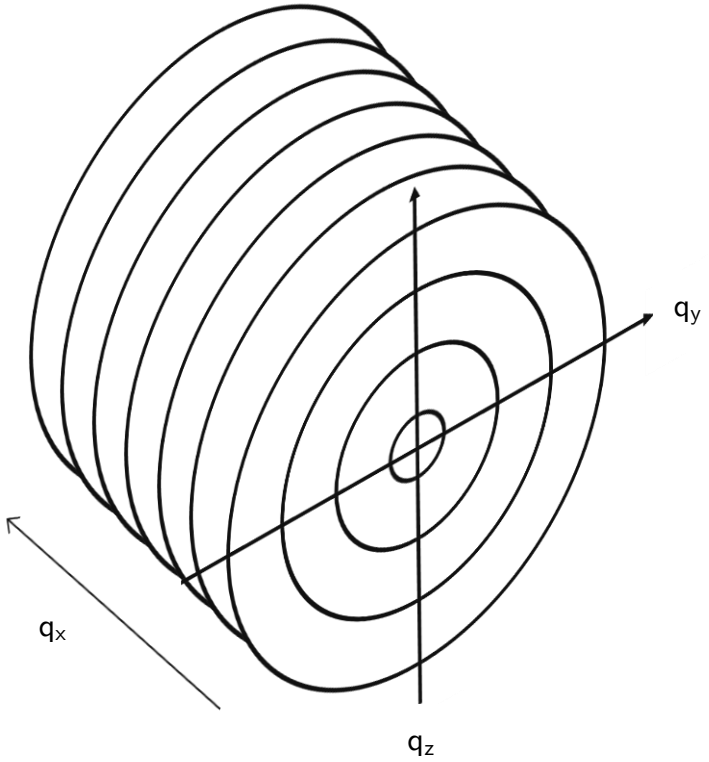

Figure 2.4 – A diagram showing the q-space volume.

In real devices hot phonon distributions decay via various phonon-phonon processes. This thermalisation is accounted for in the simulation by reducing the phonon distribution every n time steps, according to the phonon lifetime in the simulated material and the lattice temperature. The minimal phonon distribution and the initial condition of the model is thermal equilibrium, calculated using,

$$|N| = \frac{1}{\left(e^{\frac{E_{\mathbf{q}}}{kT_L}} - 1\right)} \qquad 2.14$$

Where, $|N|$ is the phonon occupation number, T_L is the lattice temperature and $E_{\mathbf{q}}$ is the phonon energy. Phonon lifetime is known to be dependent on material, carrier

density, lattice temperature, phonon distribution and decay mechanism [21]. The material and carrier density is constant throughout the hot phonon simulation which allows a constant phonon lifetime to be used. The phonon lifetime is an input parameter for the simulation and is taken from experiment.

The simulation requires the same user input as the original EMC with additional phonon specific parameters such as the $\mathbf{q}$-space volume and phonon lifetime. In this way the transient and steady state results can be compared between the two models to analyse the effects of a non-equilibrium phonon distribution. The hot phonon model will also provide the phonon distributions in $\mathbf{q}$-space, the maximum phonon occupation number as a function of time, the average phonon occupation as a function of time and the POP scattering rates at various simulation times. With this data the phonon behaviour can be investigated and any changes in electron characteristics can be analysed using the relevant phonon behaviour.

2.3. Monte Carlo simulations for modelling electronic devices in one spatial dimension

The EMC simulation can be used as a base and built upon in order to simulate electronic devices. The device model discussed in this sub chapter simulates electron motion in one spatial dimension which is a common simplification made when simulating vertical devices [44][45]. The model is used to simulate vertical Gunn diodes; the doping profiles of such devices are readily represented in one spatial

dimension and there are no significant physical effects expected to occur as a function of the non-simulated spatial directions.

The starting point for the device model discussed herein is based upon a 1D model described in a book written by Tomizawa, "Numerical Simulation of Submicron Semiconductor Devices" [18]. The model from Tomizawas book [18] was updated to utilise the latest FORTRAN syntax and was parallelised to improve performance. The cosine band structure approximation was also implemented in order to more accurately simulate transport in Gallium Nitride based devices [46]. In the following subchapter the modifications required to allow the basic EMC model to simulate electronic devices are explored in detail.

2.3.1. *1D device model Overview*

A flowchart providing an overview of the 1-dimensional device simulation algorithm is presented in Figure 2.5. The main differences between the 1-dimensional device model and the EMC are that electrons are now spatially restricted and the Poisson equation must be solved throughout the simulation to provide real-time evolution of the electric field. In solving the Poisson equation we must account for both the applied potential and the potential contribution of each electron within the device. It would be unrealistic and unnecessary to track the characteristics of every electron within a device. A common simplification in a device model is to simulate superparticles instead. A superparticle is a group of electrons which all share the

same characteristics and have a charge equal to the number of electrons within it. The number of electrons within a superparticle is a user-define parameter and must be tuned to ensure statistical stability. For the model discussed in this Thesis the number of electrons per superparticle is calculated according to the input parameter, 'number of superparticles per cell'. This allows the user to easily estimate how many particles are within the model and hence if it is computationally viable. The appropriate charge is assigned to each superparticle according the 'number of superparticles per cell' parameter and the doping profile of the device. The number of superparticles required to produce a statistically stable device simulation depends on the doping profile, the physical size of the device being simulated and the level of precision which is required. In 1-dimension, the boundary conditions for the device are fairly straight-forward in that electrons are injected and absorbed at the contacts to ensure charge neutrality.

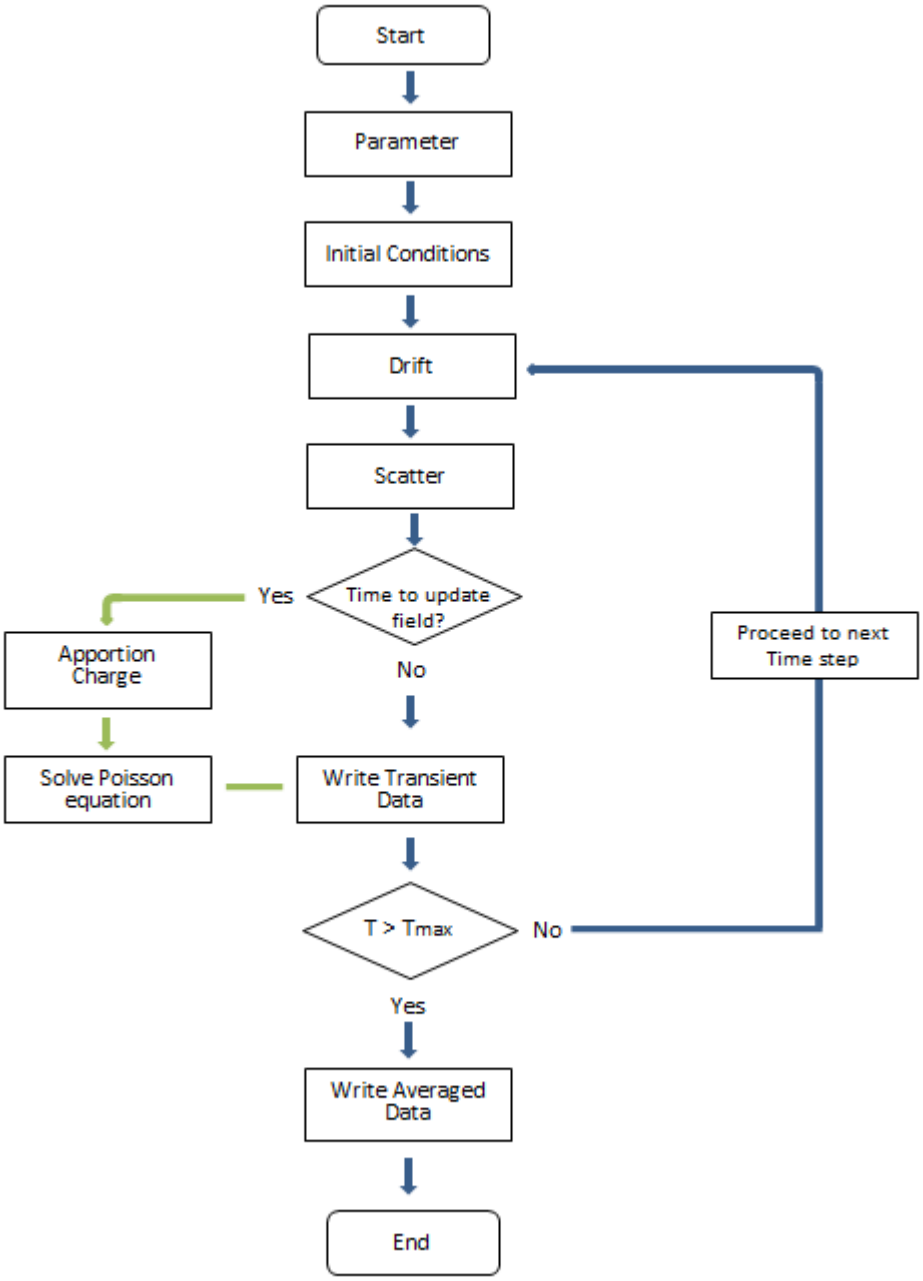

Figure 2.5 - Flowchart diagram showing an overview of how a Monte Carlo algorithm can be used to simulate electron transport in devices.

The Parameter subroutine remains largely unchanged when compared to the base EMC model. The only significant modification required is to account for the position dependent impurity scattering rate. Multiple scattering tables are now created to account for the doping profile of the device. A more specific explanation surrounding device design and doping profiles is included alongside the results presented in Chapters 4 and 5. The Initial Conditions sub-routine is responsible for assigning attributes to each electron within the system as is the case in the original EMC model. In addition to assigning an energy and $\mathbf{k}$ vector, the superparticles must also be distributed throughout a device according to the doping profile. An initial field profile is then calculated for use in the first drift routine. The Drift and Scatter routines must be updated to incorporate the appropriate boundary conditions. The position of each electron is checked to ensure that it has not drifted outside the boundaries of the device. Electrons within the vicinity of the contacts are counted to ensure charge neutrality. If more electrons are present around the contact than the doping profile would supply then they are removed; if too few are present then more electrons are injected.

Once electrons have been simulated for a whole time step the electric field must be updated. While it is possible to solve this many body problem directly according to the exact position of each electron it would be computationally expensive and would severely limit the number of particles which could be simulated. Instead, the device

area is divided into a uniform mesh. At the centre of each mesh spacing, Δx, is a grid point. Each superparticle then apportions its charge to its surrounding grid point(s) according to a charge apportionment scheme. The electric field between each gird point is then calculated using the 1-dimensional discretised Poisson equation.

2.3.2. *Charge apportionment*

To solve Poisson equation we create a discretised charge density profile based on the position of electrons within the device. The electron density profile is found by apportioning the charge of each superparticle to a particular grid point or multiple grid points, depending on the apportionment scheme. The simplest method of charge apportionment is the Nearest-Grid-Point (NGP) method. When using the NGP method the charge from each superparticle is assigned to its nearest grid point. The NGP method generally produces a noticeable amount of statistical noise, particularly at the boundaries and around the interfaces within the device.

The level of noise can be reduced by employing the Cloud-In-Cell (CIC) scheme. The CIC scheme treats each superparticle as though it is cloud of charge. The charge from each carrier is then appointed linearly to each surrounding grid point according to its position within the cell. A carrier equally spaced between 2 grid points for example would appoint 50% of its total charge to the two surrounding grid points, as is the case with the red carrier in Figure 2.6. Alternatively, the green

carrier in Figure 2.6 would apportion around 75% of charge to grid point φ_{i+1} while the remaining 25% would be apportioned to grid point φ_i.

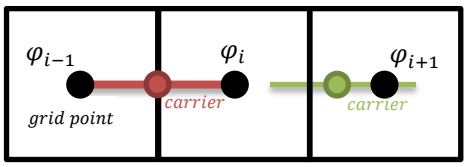

Figure 2.6 - Diagram representing the CIC charge apportionment scheme.

While investigating self-force, Laux et. al found that the CIC and NGP methods behave poorly near device contacts [47]. Self-force arises when using the NGP and CIC methods when either permittivity is not constant across a device or when a non-uniform mesh is used. Neither of these conditions is applicable to this work and so self-force is not explored further. Laux proposed the Nearest Element Centre (NEC) charge apportionment scheme as a way of reducing self-force, this scheme was also shown to perform better than the CIC scheme around contact areas [47]. Due to the improved performance around the interface and the contact areas, this is the charge apportionment scheme employed throughout this thesis. The nearest element centre scheme works in one-dimension by apportioning 50% of an electrons charge to the two closest grid points.

2.3.3. *Poisson solver*

Using the discretised Poisson equation and inputting the charge density profile and the applied potential at the boundaries the electric field between each grid point is calculated. The Poisson equation in one dimension takes the following form

$$\frac{\partial^2 \varphi}{\delta x^2} = -\frac{\rho}{\varepsilon_s} \tag{2.15}$$

This can be discretised for use on an equally spaced mesh to give

$$\frac{\varphi_{i-1} - 2\varphi_i + \varphi_{i+1}}{\Delta x^2} = -\frac{\rho_i}{\varepsilon_s} \tag{2.16}$$

Where φ_i is the potential value at the i-th grid point, Δx is the mesh size and ρ_i is the charge density at the i-th grid point. A fixed potential is implemented at each end of the device to create the contacts and so Dirichlet boundary conditions are applied. Equation 2.16 is then written as a set of linear equations in terms of φ. This can be represented in matrix form, for a set of grid points from 1 to nx, as:

$$\begin{bmatrix} -2 & 1 & & & & 0 \\ 1 & -2 & 1 & & & \\ & 1 & -2 & 1 & & \\ & & 1 & -2 & 1 & \\ & & & 1 & -2 & 1 \\ 0 & & & & 1 & -2 \end{bmatrix} \begin{bmatrix} \varphi_2 \\ \varphi_3 \\ \varphi_4 \\ \varphi_5 \\ \varphi_6 \\ \varphi_{nx-1} \end{bmatrix} = -\frac{\Delta x^2}{\varepsilon_s} \begin{bmatrix} \rho_2 - \varphi_1 \\ \rho_3 \\ \rho_4 \\ \rho_5 \\ \rho_6 \\ \rho_{nx-1} - \varphi_{nx} \end{bmatrix} \tag{2.17}$$

Where the left hand side matrix is zero in all cells apart from the three central diagonals. φ_1 is taken as the potential at the cathode (0V) and φ_{nx} is the applied potential at the anode as set by the user. Various numerical methods can then be used to solve equation 2.17. The two discussed as part of this thesis are LU decomposition and the Successive Over-Relaxation (SOR) method.

LU decomposition

The following sub-section explains the use of LU decomposition to solve equations of the form:

$$\mathrm{A}\,.\,\mathrm{x} = \mathrm{b} \qquad 2.18$$

Where x represents a set of unknown variables to be found, b is a set of known values and A is a tri-diagonal matrix of the form

$$\begin{bmatrix} b_1 & c_1 & & & & 0 \\ a_2 & b_2 & c_2 & & & \\ & . & . & . & & \\ & & . & . & . & \\ & & & a_{N-1} & b_{N-1} & c_{N-1} \\ 0 & & & & a_N & b_N \end{bmatrix}$$

Where a, b, and c can take the form of either numbers or matrices. The Poisson equation has conveniently been presented in this form in 2.17. By separating the matrix A into a lower (L) and upper (U) triangular matrix equation 2.18 can be re-written as

$$A \,.\, x = L.U.x = b \tag{2.19}$$

Where L takes the following form

$$L = \begin{bmatrix} \alpha_1 & & & & & 0 \\ \beta_2 & \alpha_2 & & & & \\ & \cdot & \cdot & & & \\ & & \cdot & \cdot & & \\ & & & \beta_{N-1} & \alpha_{N-1} & \\ 0 & & & & \beta_N & \alpha_N \end{bmatrix} \tag{2.20}$$

And U takes the following form

$$U = \begin{bmatrix} 1 & \gamma_2 & & & & 0 \\ & 1 & \gamma_2 & & & \\ & & \cdot & \cdot & & \\ & & & \cdot & \gamma_2 & \\ & & & & 1 & \gamma_2 \\ 0 & & & & & 1 \end{bmatrix} \tag{2.21}$$

A solution z can then be introduced as an intermediate solution and so equation 2.19 can be written as a set of two equations

$$\begin{aligned} L.z &= q \\ U.x &= z \end{aligned} \tag{2.22}$$

The values for the matrix A, are known from the left hand side of equation 2.17. By multiplying L and U relations can be made between the elements in the L and U matrices and the original A matrix so that:

$$\begin{aligned} a_i &= \beta_i \\ b_i &= \beta_i \gamma_{i-1} + \alpha_i \\ c_i &= \alpha_i \gamma_i \end{aligned} \qquad 2.23$$

Equations in 2.23 can then be used with forward and backward substitution processes to solve for φ.

LU decomposition was originally used in the 1-dimensional device model. As part of the 2-dimensional device model development (discussed later) the SOR routine was implemented into the 1-dimensional model to test functionality. It was found that the SOR routine produced results with a similar level of precision compared with the LU decomposition method with less computational expense and so the SOR method replaced LU decomposition as the Poisson solver in the 1-dimensional device model.

Successive Over-Relaxation (SOR)

Successive Over-Relaxation (SOR) is a relaxation method used for solving boundary value problems. Relaxation methods require the splitting of a sparse matrix (A in equation 2.18) which is then solved using an iterative procedure. Successive Over-Relaxation is derived from the Gauss-Seidel method. If we take the Gauss-Seidel

method and anticipate future corrections by applying an over-correction to the required value of each iteration then a faster convergence and a more efficient algorithm is achieved. The Gauss-Seidel method can be written as [48]

$$x^{(r)} = x^{(r-1)} - (L + D)^{-1}\xi^{(r-1)} \quad 2.24$$

Which, when over-corrected is given by [48]

$$x^{(r)} = x^{(r-1)} - \omega(L + D)^{-1}\xi^{(r-1)} \quad 2.25$$

Where $\xi^{(r-1)}$ is the residual vector and ω is the over relaxation parameter, L is the lower triangle of the matrix A and D is the diagonal part of the matrix A. The optimal choice of over-relaxation parameter is found from the spectral radius of the Jacobi iteration so that

$$\omega = \frac{2}{1 + \sqrt{1 - \rho_{\text{Jacobi}}^2}} \quad 2.26$$

Where in one dimension

$$\rho_{\text{Jacobi}} = \cos\left(\frac{\pi}{nx}\right) \quad 2.27$$

Where nx is the number of grid points in the x direction.

To apply this method to solve the Poisson equation we discretise the equation as shown below.

$$\varphi_{i-1} - 2\varphi_i + \varphi_{i+1} = -\frac{\Delta x^2 \rho_i}{\varepsilon_s} \quad 2.28$$

The iterative procedure of the SOR method is then defined by solving for φ_i.

$$\varphi_i^* = \frac{1}{2}\left(\frac{\Delta x^2 \rho_i}{\varepsilon_s} - \varphi_{i-1} - \varphi_{i+1}\right) \quad 2.29$$

So that the weighted averaged is

$$\varphi_i^{new} = \omega\varphi_i^* + (1-\omega)\varphi_i^{old} \quad 2.30$$

The residual ξ_i at each stage is calculated as follows

$$\xi_i = \varphi_{i-1} - 2\varphi_i + \varphi_{i+1} - \frac{\Delta x^2 \rho_i}{\varepsilon_s} \quad 2.31$$

So that the SOR algorithm becomes

$$\varphi_i^{new} = \varphi_i^{old} + \frac{\omega\xi_i}{2} \quad 2.32$$

The residual and a tuneable convergence parameter can then be used to determine when to terminate the calculation. Since the potential being calculated is only dependent on the two potentials on either side we are able to split the calculation over every other square resulting in one loop for the odd grid points and another for the even grid points. This modification enables the introduction of parallel computing and increases the efficiency of the algorithm.

2.3.4. *Mesh size and time step limitations*

The Monte Carlo device simulation is performed through an iterative procedure concerned with the movement of electrons across a device divided into a mesh of equal spacing, Δx; and is simulated for a total time divided into a number of time steps Δt. For the device simulation to be stable we must ensure an appropriate time step and mesh size is chosen. It is a physical requirement that the time step be smaller than the inverse of the plasma frequency ω_p [18], so that

$$\frac{1}{\Delta t} \gg \omega_p = \sqrt{\frac{e^2 n}{\epsilon_s m^*}} \qquad 2.33$$

Where e is electronic charge, ϵ_s is the dielectric constant of the simulated material, $m^*$is the effective mass and n is the charge density.

The mesh size, Δx, is used for determining the potential profile and so must be chosen according to the screening length, or the Debye length, λ_D. It is a requirement that Δx be smaller than λ_D so that [18],

$$\Delta x < \lambda_D = \sqrt{\frac{\epsilon_s k_B T_L}{e^2 n}} \qquad 2.34$$

Where k_B is the Boltzmann constant and T is taken as the lattice temperature.

The expected peak electron velocity must also be taken into account when choosing a suitable time step and mesh spacing, so that

$$\Delta x > v_{max}\, \Delta t \qquad 2.35$$

By ensuring electrons do not travel further than one mesh spacing in one time step the electric field will more accurately reflect the electron density profile. v_{max} is estimated using the bulk EMC model. If an electron drifts further than one mesh spacing in one time step, i.e. $v > v_{max}$, an error message is produced and the simulation will terminate. If electrons were allowed to travel too far in a single time step then significant changes in the charge distribution could occur between updates of the electric field profile, reducing the validity of the model.

2.3.5. *Output*

In the same way as the basic EMC the average electron energy, average electron velocity and valley occupancy is recorded as function of time. These characteristics are calculated within each individual mesh spacing in the device model so that energy, velocity and occupancy profiles are produced. The potential, charge density and electric field is also available as a function of device position. The number of electrons leaving the contacts is also recorded which can be analysed analogously to current.

2.4. Monte Carlo simulations of 2-dimensional Gunn diodes

The 1-dimensional device model described in the previous sub-chapter has been developed further so that simple 2-dimensional devices can be modelled. The developments required to expand the 1-d device model include, developing a 2-dimensional meshing system; altering the charge apportionment scheme to account for the extra nodes in the y-direction; implementing a 2-dimensional Poisson solver and ensuring electrons are properly represented in two dimensions using appropriate boundary conditions. The current 2-dimensional model is part of a development process which aims to simulate electronic devices with 2-dimensional geometries such as Heterostructure Field Effect Transistors (HFETs) and High-Electron-Mobility Transistors (HEMTs). In its current form the model is capable of simulating vertical devices with an extra dimension. This step in the development

process is essential to ensure electrons are being properly modelled in 2-directions. The following sub-chapter discusses the 2-dimensional model within the context of simulating 2-dimensional vertical electronic devices which take the form shown in Figure 2.7.

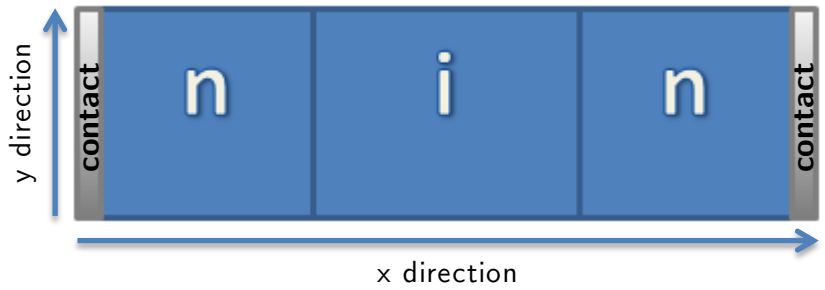

Figure 2.7 – A representation of the 2-dimensional planar device which is modelled.

2.4.1. *Boundary conditions*

In the 1-dimensional model electrons are injected and absorbed at the contacts to ensure charge neutrality. This same process is implemented in the 2-dimensional model at the contact cells for all values of y. We must also restrict the movement of electrons in the direction parallel to the contacts; if any electron passes outside of the device in the y-direction it is elastically reflected back into the device in accordance with the conditions given in equation 2.36.

$$\begin{aligned} &\text{If } y < 0 \quad \text{then } y' = -y \\ &\text{If } y > y_{max} \quad \text{then } y' = y_{max} - (y - y_{max}) \end{aligned} \qquad 2.36$$

In addition to the physical constraints there are additional boundary conditions associated with the field calculation, these are discussed in more detail in the 'Poisson solver' sub-section.

2.4.2. *Charge apportionment*

For the 2-dimensional simulation the NEC charge apportionment scheme has been used. The scheme was modified to account for the extra dimension so that each electron apportions 25% of its total charge to the 4 nearest grid points. As an example, all electrons which are within the area outlined in red in Figure 2.8 will apportion 25% of their charge to each grid point, $\varphi_{i,j}$, $\varphi_{i-1,j}$, $\varphi_{i-1,j+1}$ and $\varphi_{i,j+1}$.

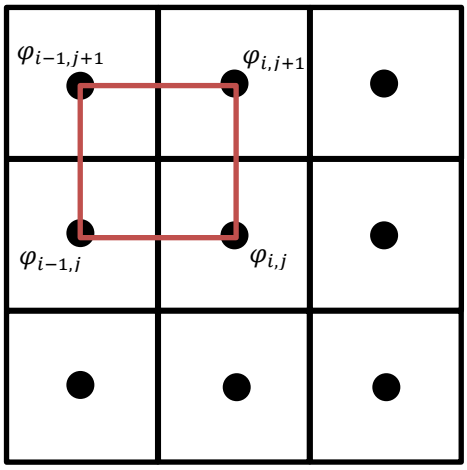

Figure 2.8 – A diagram used for the description of the NEC scheme in two dimensions

2.4.3. *Poisson solver*

With the introduction of a second spatial dimension the Poisson equation is now solved across a 2-dimensional charge density profile $\rho_{i,j}$. The boundary conditions of

the calculation are also changed. To model 2-dimensional vertical devices mixed boundary conditions are required which assume a zero field at the top and bottom edges (Neumann boundary); and a fixed potential at the contacts (Dirichlet boundary). The numerical implementation of these boundary conditions are discussed in the following section. The 2-dimensional Poisson equation is given by

$$\frac{\partial^2 \boldsymbol{\varphi}}{\delta x^2} + \frac{\partial^2 \boldsymbol{\varphi}}{\delta y^2} = -\frac{\boldsymbol{\rho}}{\varepsilon_s} \qquad 2.37$$

Where $\boldsymbol{\varphi}$ is electric potential, x and y are positions in real-space and $\boldsymbol{\rho}$ is the charge density. This can be discretised on an equally spaced 2 dimensional mesh to give:

$$\frac{\varphi_{i-1,j} - 2\varphi_{i,j} + \varphi_{i+1,j}}{\Delta x^2} + \frac{\varphi_{i,j-1} - 2\varphi_{i,j} + \varphi_{i+1,j+1}}{\Delta y^2} = -\frac{\rho_{i,j}}{\varepsilon_s} \qquad 2.38$$

Where i and j identify the grid points within the mesh and Δx and Δy is the mesh spacing in the x and y direction.

In matrix form this can still be represented using the form shown in equation 2.19 $(A \,.\, x = b)$. Matrix A is now more complex due to the second dimension and so using LU decomposition is no longer viable. The sparse matrix A can be split into a strictly lower (L), upper (U) and diagonal (D) matrix so that relaxation methods such as the SOR method can be used to find a solution. The product $A.\,x$ for a

device with 5 grid points in the x direction and 3 grid points in the y direction is given as an example in equation 2.39.

The matrices are presented assuming a uniform mesh spacing in each direction and with Dirichlet boundaries implemented; where the potentials at x =1 and nx are known values according to the applied potential. Neumann Boundary conditions are applied within equation 2.39. This process is explained in detail later in this section.

$$\begin{bmatrix} -4 & 1 & & & 1 & & & & & & & \\ 1 & -4 & 1 & & & 1 & & & & & & \\ & 1 & -4 & 1 & & & 1 & & & & & \\ & & 1 & -4 & & & & 1 & & & & \\ 1 & & & & -4 & 1 & & & 1 & & & \\ & 1 & & & 1 & -4 & 1 & & & 1 & & \\ & & 1 & & & 1 & -4 & 1 & & & 1 & \\ & & & 1 & & & 1 & -4 & & & & 1 \\ & & & & 1 & & & & -4 & 1 & & \\ & & & & & 1 & & & 1 & -4 & 1 & \\ & & & & & & 1 & & & 1 & -4 & 1 \\ & & & & & & & 1 & & & 1 & -4 \end{bmatrix} \cdot \begin{bmatrix} \varphi_{2,1} \\ \varphi_{3,1} \\ \varphi_{4,1} \\ \varphi_{nx-1,1} \\ \varphi_{2,2} \\ \varphi_{3,2} \\ \varphi_{4,2} \\ \varphi_{nx-1,2} \\ \varphi_{2,ny} \\ \varphi_{3,ny} \\ \varphi_{4,ny} \\ \varphi_{nx-1,ny} \end{bmatrix} = \frac{\Delta x^2}{\varepsilon_s} \begin{bmatrix} \rho_{2,1} - \varphi_{1,1} - \varphi_{1,0} \\ \rho_{3,1} - \varphi_{1,0} \\ \rho_{4,1} - \varphi_{1,0} \\ \rho_{nx-1,1} - \varphi_{nx,1} - \varphi_{1,0} \\ \rho_{2,2} - \varphi_{1,2} \\ \rho_{3,2} \\ \rho_{4,2} \\ \rho_{nx-1,2} - \varphi_{nx,2} \\ \rho_{2,ny} - \varphi_{1,ny} - \varphi_{2,ny+1} \\ \rho_{3,ny} - \varphi_{2,ny+1} \\ \rho_{4,ny} - \varphi_{2,ny+1} \\ \rho_{nx-1,ny} - \varphi_{nx,ny} - \varphi_{2,ny+1} \end{bmatrix} \quad 2.39$$

Successive Over-Relaxation (SOR)

The potential calculation required for the SOR routine is made quite different with the introduction of the second dimension. The relaxation parameter ω is found using the same equation as for the 1-dimensional SOR. The calculation of the Jacobi spectral radius ρ_{Jacobi} must be updated and is given by [48]

$$\rho_{\text{Jacobi}} = \frac{\cos\left(\frac{\pi}{nx}\right) + \left(\frac{\Delta x}{\Delta y}\right)^2 \cos\left(\frac{\pi}{ny}\right)}{1 + \left(\frac{\Delta x}{\Delta y}\right)^2} \quad 2.40$$

Where nx is the number of grid points in the x direction and ny is the number of grid points in the y direction.

Solving for $\varphi_{i,j}$ must also account for the potentials above and below according to the discretised Poisson equation shown in equation 2.39. The iterative procedure of the SOR in 2 dimensions, assuming $\Delta x = \Delta y$ is then given by [48]

$$\varphi_{i,j}^{*} = \frac{1}{c_{i,j}}\left(\frac{\rho_{i,j}\Delta x^2}{\varepsilon_s} - a_{i,j}\varphi_{i-1,j} - b_{i,j}\varphi_{i+1,j} - d_{i,j}\varphi_{i,j-1} - e_{i,j}\varphi_{i+1,j+1}\right) \quad 2.41$$

Where, according to the matrix A in equation 2.39, a=b=c=e=1 and e=-4.

The weighted average must then account for the second dimension so that [48]

$$\varphi_{i,j}^{new} = \omega\varphi_{i,j}^{*} + (1-\omega)\varphi_{i,j}^{old} \quad 2.42$$

Where the residual ξ_i at each stage is calculated as follows [48]

$$\xi_i = a_{i,j}\varphi_{i-1,j} + b_{i,j}\varphi_{i+1,j} - c_{i,j}\varphi_{i,j} + d_{i,j}\varphi_{i,j-1} + e_{i,j}\varphi_{i+1,j+1} - \frac{\rho_{i,j}\Delta x^2}{\varepsilon_s} \quad 2.43$$

So that the SOR algorithm becomes [48]

$$\varphi_{i,j}^{new} = \varphi_{i,j}^{old} + \frac{\omega\xi_i}{4} \quad 2.44$$

In the same way as the 1-dimensional algorithm the residual and a convergence parameter can be used to terminate the algorithm at the final result. In a similar way to the 1-dimensional model the mesh is split into odd and even meshes much like the red and black squares of a chess board. Since the red squares only depend on the black squares and black on the red squares it is possible to parallelise this process to improve performance.

The boundary conditions for the 2-dimensional problem are more complex than in the 1D model. Mixed boundary conditions are implemented with Neumann boundary conditions at the top and bottom and Dirichlet boundary conditions at the contacts. The Dirichlet conditions are readily implemented in the same way as the 1 dimensional model. The Neumann conditions must be incorporated into the Poisson equation and followed through to the set of linear equations for use in the SOR routine.

To implement the Neumann boundary conditions we create a row of buffer cells above the top layer ($\mathrm{y} = \mathrm{ny} + 1$) and below the bottom layer ($\mathrm{y} = 0$) on the device mesh. To ensure a zero field the following conditions must be applied $\varphi_{\mathrm{i},0} = \varphi_{\mathrm{i},1}$ and $\varphi_{\mathrm{i,ny+1}} = \varphi_{\mathrm{i,ny}}$ for all i. These identities are implemented into the SOR method using coefficients a,b,c,d and e in equation 2.43. If j=1 then j-1=0 and hence we are referring to a buffer mesh point, in which case $d_{1,i}$=0 and $c_{1,i}$=3 for all i. If j=ny

then j+1 = ny+1 which again refers to a buffer mesh point so $e_{ny+1,i}$=0 and $c_{ny+1,i}$ = 3 for all i.

2.5. Summary

In this chapter the EMC method of simulating electron transport has been described. Three development routes based around the EMC model have then been discussed. Firstly, the modifications required to investigate hot phonon effects in bulk semiconductors have been explained. These include tracking the phonon population and updating the POP scattering rate accordingly. Secondly, the modifications required to simulate 1-dimensional electronic devices have been explained. Electrons are under spatial constraints within a meshed area; their position is tracked so that the Poisson equation can be solved to produce a self-consistent electric field profile. The importance of mesh size and time step was discussed along with the implementation of the appropriate boundary conditions. Finally, the modifications required to simulate simple 2-dimensional electronic devices have been explained. Electrons are now able to move in an additional spatial dimension which requires the implementation of more complex boundary conditions. The method behind solving the more complex 2-dimensional Poisson equation was also covered.

The remaining chapters of this thesis are concerned with using these models in various investigations. In Chapter 3 the hot phonon model is validated against

published data before results are presented which investigate hot phonon effects in bulk $In_{0.53}Ga_{0.47}As$. In Chapter 4 the 1-dimensional device model is used to investigate GaAs Gunn devices. Results from the model are compared with a Monte Carlo simulation under taken by Tully et. Al [1] in 1983. In Chapter 5 the 1-dimensional device model has been used to investigate GaN Gunn devices. Results are presented for a device operating in accumulation mode and a device operating in dipole mode. In Chapter 6 the 2-dimensional device model has been used to simulate a 2-dimensional GaN Gunn diode with the same design as the 1-dimensional model presented in Chapter 5 as a proof of concept exercise.

Chapter 3. Hot phonon effects in $In_{0.53}Ga_{0.47}As$

$In_{0.53}Ga_{0.47}As$ is widely used for fabricating both electronic and photovoltaic devices. InGaAs channel Metal-Oxide-Semiconductor Field-Effect Transistors (MOSFETs) are considered to be the most promising non silicon devices for next generation nanoscale CMOS technology [42]. Even today, circuits based on InGaAs MOSFETs are widely used in smart phones, wireless technologies and fibre optical communication systems.

In devices such as Hot Carrier Solar Cells (HCSCs) hot electrons are required for proper device function[49]; while for electronic devices such as High Electron Mobility Transistors (HEMTs) or MOSFETs hot electrons can limit device performance [50][51]. Recent work for GaN based devices suggests that hot electrons are responsible for limiting device performance at large applied fields. Electron temperatures have been measured experimentally at 2600 and 5000K [13][52]. While the Longitudinal Optical (LO) phonon energy is larger in GaN than for InGaAs and so hot phonon effects are likely to be more pronounced, it is clear

that hot phonon effects should not be neglected when discussing electron transport. We report on how a hot phonon distribution can affect both steady state and transient transport characteristics in $In_{0.53}Ga_{0.47}As$.

Three valleys are simulated (Γ-L-X) using the $\mathbf{k}.\mathbf{p}$ approximation. The scattering mechanisms included in the model are polar optical, non-polar optical and acoustic phonons, ionised impurity, intervalley and piezoelectric. The scattering and phonon tables are updated every 25fs. We simulate 100,000 particles at 300K for both the equilibrium and non-equilibrium phonon simulations. Phonon dispersion is currently ignored since it is small. Screening and degeneracy effects are not included. Although $In_{0.53}Ga_{0.47}As$ is a ternary compound we use the common approximation that we have a single LO mode. Phonon energy was determined in [27] from the two binary materials, InAs and GaAs using the interpolation methods of Adachi. The LO phonon lifetime of $In_{0.53}Ga_{0.47}As$ is still unknown [53], so the LO phonon lifetime in GaAs (τ_{LO}= 3ps at 300K [54]) has been used instead. We assume a zinc blende crystal structure. Other material parameters required for the simulation can be found in Table 3.1 below.

Parameter (units)	$In_{0.47}Ga_{0.53}As$
Density (kg/m^3)	5500
Impurity Concentration (cm^{-3})	1×10^{16}
Longitudinal sound velocity (ms^{-1})	4740
Transverse sound velocity (ms^{-1})	2690
Non-polar optical deformation potential coupling constant (eV/m)	10^{11}
Intervalley scattering coupling constant (eV/m)	10^{11}
Acoustic deformation potential (eV)	9.2
Piezoelectric constant e_{14} (Cm^{-2})	-0.09905
Energy gap (eV)	0.77
Energy separation between L valley and Γ valley (eV)	0.46
Energy separation between X valley and Γ valley (eV)	0.59
Number of equivalent L valleys	4
Number of equivalent X valleys	3
Effective mass in Γ valley (m_0)	0.041
Effective mass in L valley (m_0)	0.29
Effective mass in X valley (m_0)	0.68
Polar optical phonon energy (eV)	0.0327
Lattice constant (Å)	5.8687

Table 3.1 – Material parameters for $In_{0.47}Ga_{0.53}As$ at 300K. [27][28]

In the following chapter the behaviour of phonons within the model will be analysed and compared to the literature. The effects of a non-equilibrium phonon distribution on the steady state and transient transport characteristics will then be explored.

Average electron velocity, average electron energy and fractional valley occupancy are analysed as a function of applied electric field and simulation time. Momentum and energy relaxation times and Polar Optical Phonon (POP) scattering rates are also presented to support the analysis.

3.1. Demonstration of phonon behaviour

Before investigating the effects a non-equilibrium phonon distribution will have on the transport characteristics of $In_{0.53}Ga_{0.47}As$, it is essential to ensure that realistic phonon behaviour is being simulated. The literature relating to both electron transport and phonon behaviour is quite sparse but there are two studies which investigate hot phonon effects in GaAs that can be used for comparison [43][55]. By analysing how the phonon distribution changes with time the thermalisation of the phonon distribution is characterised which can then be compared to the phonon distributions presented by Mickevicius [55].

At low fields and early simulation times the phonon population is expected to be around thermal since not many phonons will have been emitted. Using equation 3.1,

$$|N| = \frac{1}{\left(e^{\frac{E_q}{kT}} - 1\right)} \qquad 3.1$$

where N_q is the phonon occupation number and E_q is the phonon energy, the

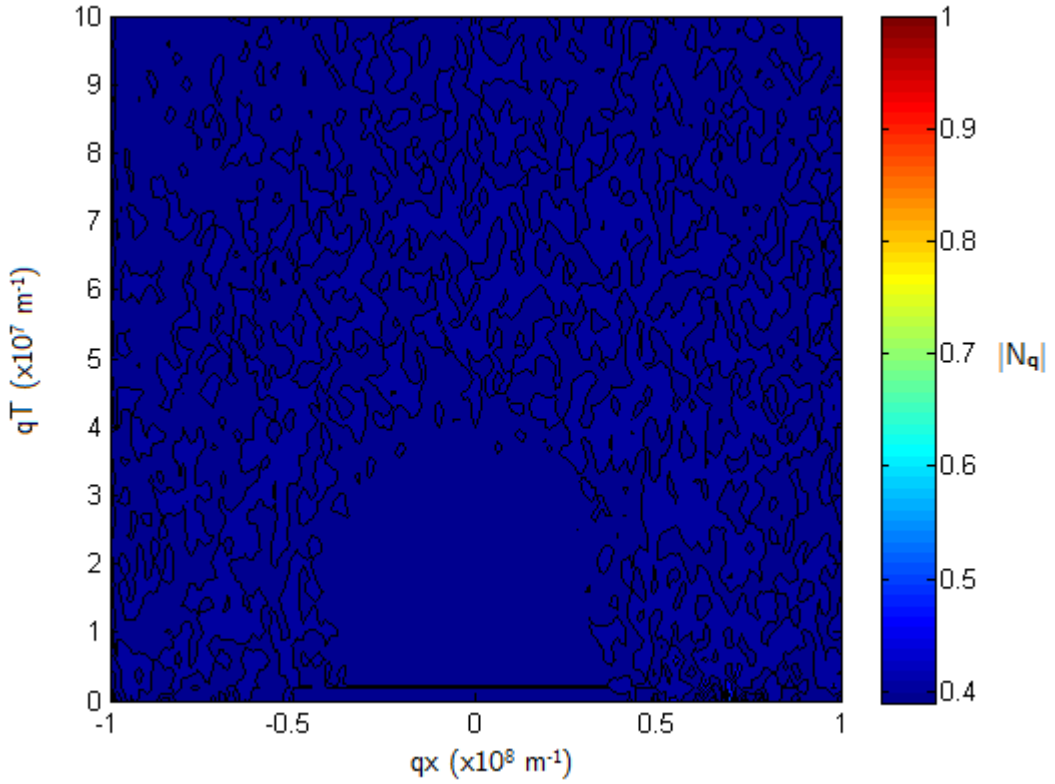

Figure 3.1 – Phonon distribution as a function of phonon wave vector for an applied field of 0.5kv/cm after 1ps, where qx is the phonon wave vector in the direction of the applied field and qT is the component in the perpendicular plane.

phonon occupation number is calculated for 300K. For InGaAs, |N| in equilibrium at 300K is 0.39. In Figure 3.1 the phonon population (|N|) for each qx and qt in q-space is presented and is found to be approximately thermal (0.39) for t > 1ps. The electric field is applied across the material at t=0 with a value of 0.5kV/cm. Attention can now be turned to the evolution of the phonon distribution with time. In [55] Mickevicius represents the time evolution of the maximum phonon occupation number (N_{max}) and the phonon population averaged over the entire

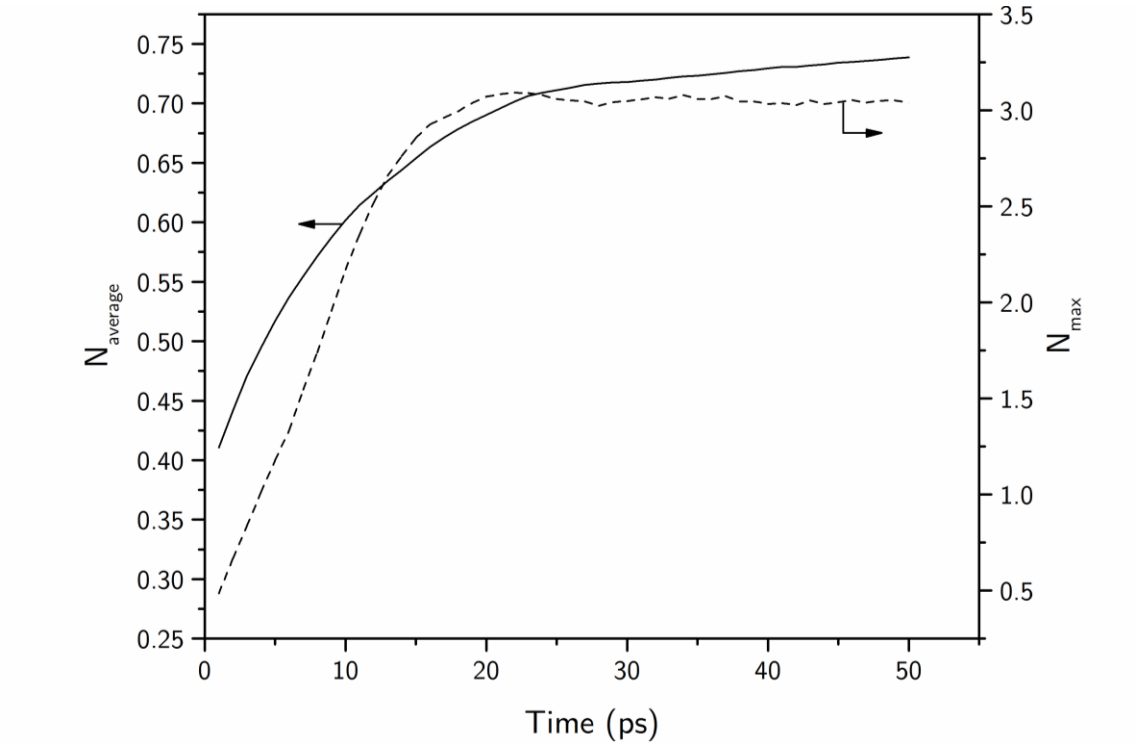

Figure 3.2 – The time evolution of the average phonon population (left axis) and maximum phonon occupation number (right axis) with an applied field of 5kv/cm.

simulated $\mathbf{q}$-space ($N_{average}$). N_{max} is the maximum phonon occupation number from all grid points in q-space defined by qx and qt. $N_{average}$ is the mean phonon occupation number calculated from all values of qx and qt. At t=0 the electric field is applied across the material. It was found that the maximum phonon occupation saturates faster than the average phonon occupation. Phonon evolution can then be analysed as a 2 stage process; the first is associated with the preference for phonons to be emitted in the direction of the applied field and the second associated with the redistribution of phonons in momentum space. Figure 3.2 is a re-creation of figure 1 presented in [55] using our results obtained for InGaAs which confirms the same findings. The average phonon occupation after 1ps is around thermal as expected. Both the average and maximum phonon occupation numbers sharply

increase with time as phonons are emitted. We can see the maximum phonon occupations (Nmax) saturate after ~15ps, whereas the average phonon occupation (Naverage) continues to increase as phonons are redistributed throughout q-space. The two stage process can be observed directly in Figure 3.3. The phonon distribution increases in magnitude in the forward direction between 1 and 10ps. After 10ps the magnitude of the occupation doesn't noticeably increase, whilst areas of $\mathbf{q}$ with previously thermal phonon occupation numbers begin to display significant phonon occupation. The 2 stage process is a consequence of the anisotropic angular dependence of scattering angle on electron energy.

A noticeable characteristic of the phonon distributions presented in Figure 3.3 is the consistently thermal phonon occupation between $q_x = -0.25\text{x}10^8 m^{-1}$ and $0.25\text{x}10^8 m^{-1}$ and $q_T < 3\text{x}10^7 m^{-1}$. This is consequence of energy and momentum conservations laws applied to the electron phonon interaction. There is a minimum energy associated with the emission of a phonon which in turn leads to a minimum phonon momentum ($\mathbf{q}_{\min}$). We can see that the lack of phonon occupation is found within a seemingly constant radius which is expected since $\mathbf{q^2} = q_x^2 + q_T^2$ and the conservation laws result in a minimum allowed value for $\mathbf{q}$.

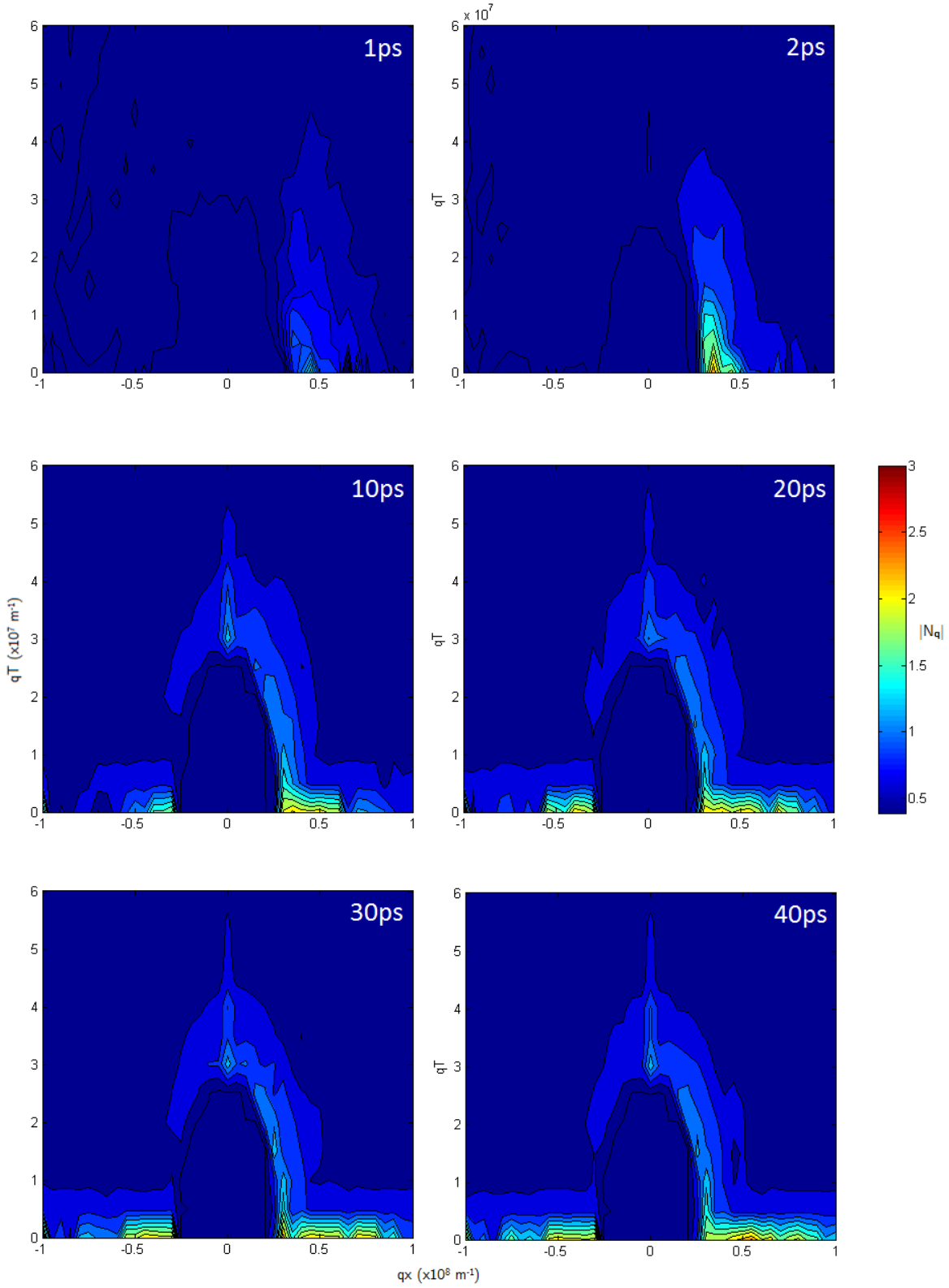

Figure 3.3 – Phonon distributions as a function of phonon wave vector for an applied field of 5kv/cm after 1, 2, 10, 20, 30 and 40ps, where qx is the phonon wave vector in the direction of the applied field and qT is the component in the perpendicular plane.

3.2. Steady State Characteristics

Since the phonon population is no longer constant throughout our simulation the POP scattering rate changes, which in turn affects the steady state transport characteristics. Several hot phonon effects have been suggested in the literature. The effects are complex and vary depending on lattice temperature, electron density, material, impurity concentration, applied field and more. In the following section the effects of a non-equilibrium phonon distribution on the steady state transport characteristics in bulk $In_{0.53}Ga_{0.47}As$ is investigated.

3.2.1. *Electron energy*

Analytical investigations by Ridley [56] conclude that one of the general effects of a hot phonon distribution on high field transport is to slow the rate of energy relaxation. Previous Monte Carlo investigations into hot phonon effects in bulk GaAs have all found that hot phonons increase the average electron energy in time [55][57]. The accepted theory is that a higher population of phonons increases the rate of electron-phonon interaction. Phonons cannot be emitted when electrons have energies less than the phonon energy meaning the increased electron-phonon interaction favours phonon absorption. In the case of Monte Carlo simulations this effect should manifest itself in the POP scattering rates; these are not published for the two Monte Carlo studies mentioned previously.

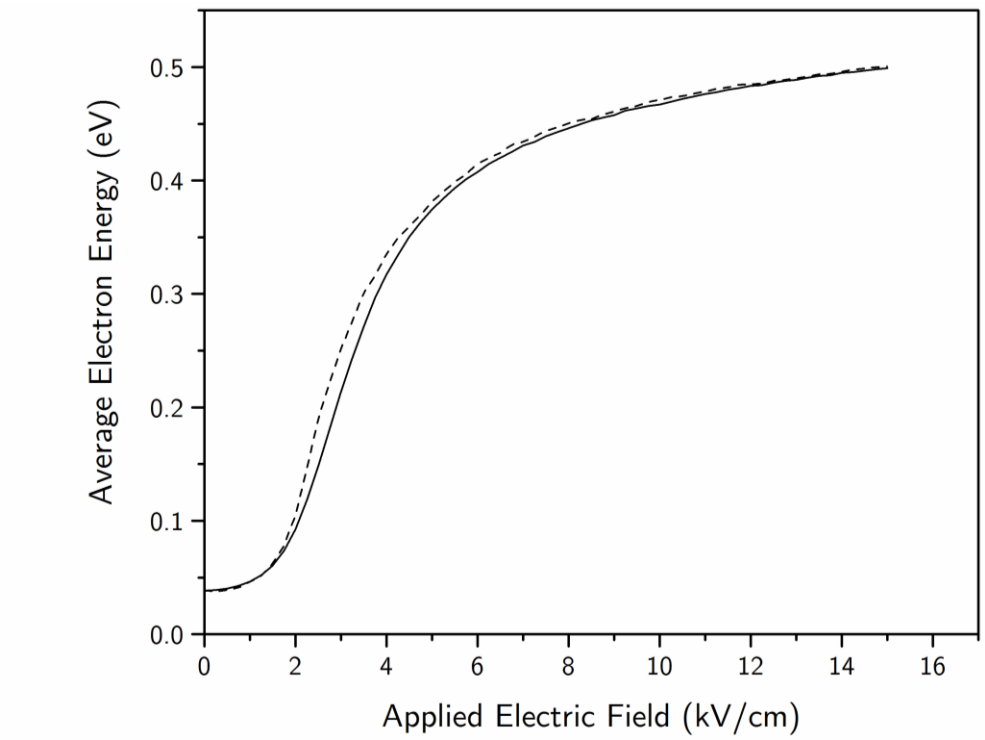

Figure 3.4 Energy field characteristics for the simulation with a static phonon population (solid line) and the non-equilibrium phonon simulation (dashed line).

The average electron energy as a function of field from the simulation with non-equilibrium phonons is compared to the model with equilibrium phonons in Figure 3.4. The difference in average electron energy at small applied fields is slight. This behaviour is expected since the phonon population will not be considerably different from thermal. As the field increases so does the difference in electron energy. The energy difference reaches a maximum of 31% around the critical field (~2.5kV/cm) in $In_{0.53}Ga_{0.47}As$ and then begins to reduce. At the critical field a significant number of electrons are beginning to transfer to the upper valleys. For fields higher than the critical field intervalley scattering becomes the dominant scattering mechanism and so the effects of POP scattering become less significant. Hot phonon effects in GaN

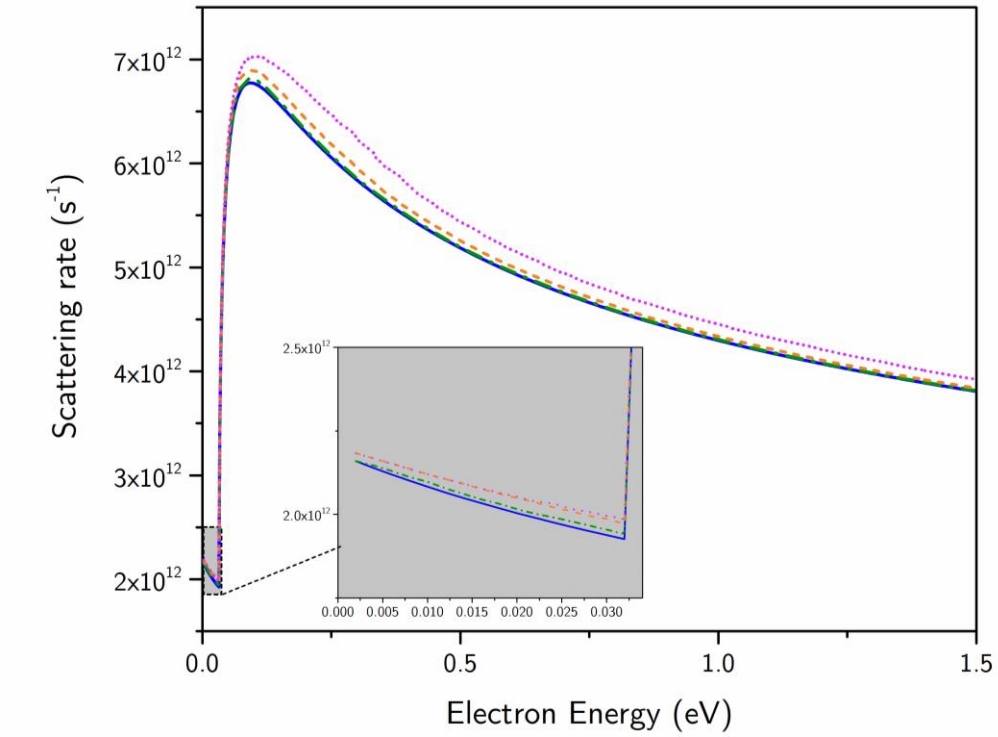

Figure 3.5 Comparison of POP scattering rates at different applied fields. Results presented for an equilibrium phonon distribution (blue solid line) and the non-equilibrium phonon simulations after 20ps at applied fields of 0.5kV/cm (dot-dashed green line), 1.5kV/cm (dashed orange line) and 2.5kV/cm (dotted purple line). The inset provides a zoomed in view of the POP rate at energies less than the phonon energy (0.0327eV).

have been studied by Dyson et. al which, in accordance with the previously mentioned GaAs studies, show that hot phonons increase average electron energy [41]. Dyson presents the POP scattering rate for different simulation times [41]. There is an increase in POP absorption when a non-equilibrium phonon distribution is accounted for. The POP absorption rate increases with phonon occupation and hence simulation time. The POP scattering rate as a function of energy for InGaAs is presented in Figure 3.5 for different applied fields. In the same way the POP rate increases with time in the study by Dyson [41], due to an increased phonon occupation, we find that the POP rate increases with applied electric field. This

effect can be observed from the scattering rates in Figure 3.5 for energies both above and below the phonon energy. The increase in phonon absorption relative to phonon emission explains why the average electron energy increases in the steady state regime when hot phonons are accounted for.

In order to fully investigate the effects of an increased POP scattering rate the energy relaxation time has been calculated for both the simulation with a thermal phonon population and the non-equilibrium phonon simulation using equation 3.2, from Bulutay [58],

$$\tau_e = \frac{\langle E \rangle - E_0}{eF\langle \mathbf{v}_x \rangle} \qquad 3.2$$

where τ_e is the energy relaxation time, E_0 is the thermal energy, $\langle E \rangle$ is the average electron energy, $\langle \mathbf{v}_x \rangle$ is the average electron velocity in the direction of the applied electric field and F is the applied electric field. The energy relaxation times are presented in Figure 3.6. For energies lower than the phonon energy, relaxation times are around 5% longer when a non-equilibrium phonon distribution is simulated. The difference in energy relaxation time is at its maximum at higher electron energies. Energy relaxation times for the equilibrium phonon simulation and non-equilibrium at the point of maximal difference are around 3.5ps and 4.2ps respectively, a 15% change.

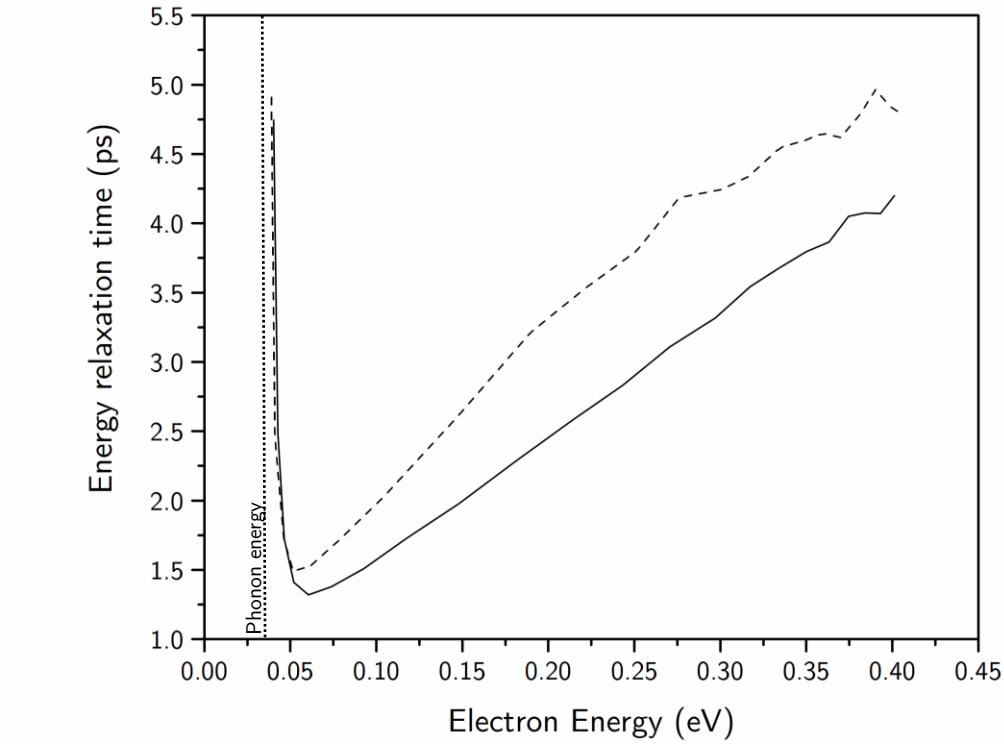

Figure 3.6 Energy relaxation time for electrons in the equilibrium simulation (solid line) and non-equilibrium phonon simulation (dashed line). The phonon energy for InGaAs is given by the dotted line for reference.

The energy relaxation time is a good indicator for how significant any transient effects will be. The average electron energy has been shown to increase in Figure 3.4 for the mid-field regime when hot phonons are accounted for. An increasing phonon population with applied field is shown to increase phonon absorption which in turn affects the average electron energy. In the same way that the phonon occupation, and phonon reabsorption, increases with applied field, it is expected that the phonon population will increase with time for any particular applied field. It is expected then that a non-equilibrium phonon distribution will increase electron energy, or increase the energy relaxation time, in the transient regime, especially at

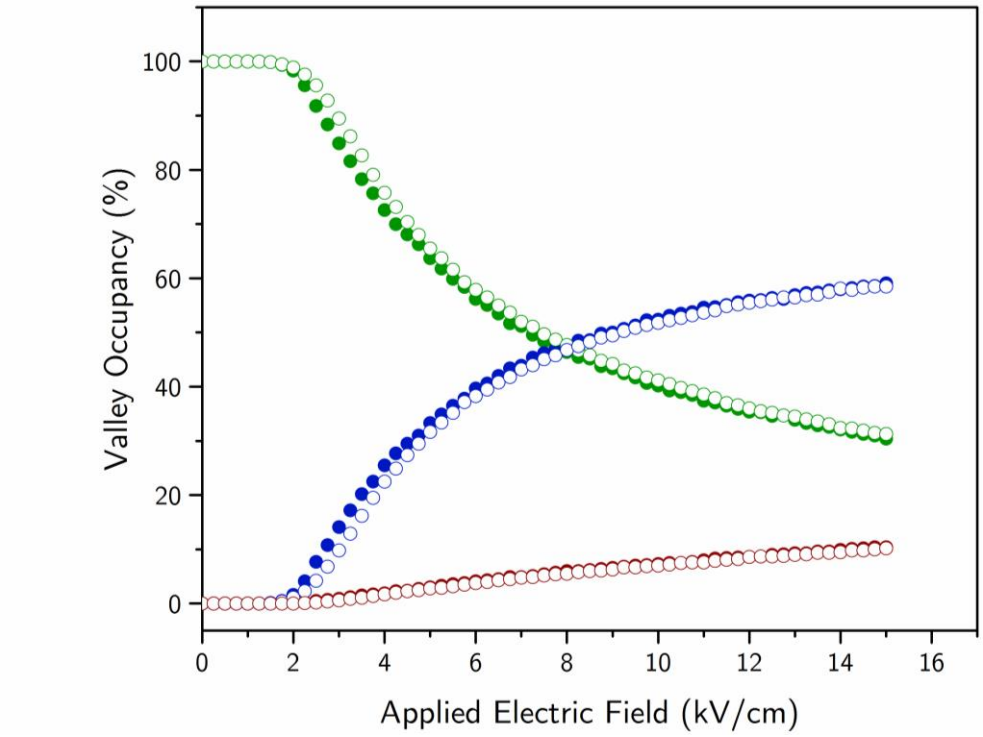

Figure 3.7 Occupancy of Γ valley (Green circles) L valley (blue circles) and X valley (red circles) for equilibrium phonons (hollow circles) and non-equilibrium phonons (filled circles) as a function of applied electric field.

high fields where a significant number of high energy electrons are present. An increase in average electron energy for a particular applied field will reduce the field at which electrons begin to transfer from the Γ valley to the upper L valley. This effect will manifest itself as a reduction in the critical field when velocity-field characteristics are observed.

The fractional valley occupancy is presented in Figure 3.7 and shows a slight reduction in the field at which electrons begin to transfer. The number of electrons occupying the upper valleys is then higher in the non-equilibrium phonon case for every applied field. Electrons in the upper valleys have a higher effective mass and

hence a lower mobility. This effect will contribute to any changes in electron velocity caused by the inclusion of a non-equilibrium phonon distribution.

3.2.2. *Electron velocity*

Hot phonons have been shown to have various effects on the mobility and velocity of electrons within a material depending on carrier concentration, impurity concentration, lattice temperature and applied electric field [55][57]. The exact cause of the changes in velocity can be difficult to pinpoint since the velocity can be affected directly by the increased phonon distribution, as well as indirectly by the changes in electron energy. In the following section the different effects which have been reported in the literature are explained. Results collected using the model outlined in this thesis are presented then for InGaAs. Hot phonons have the ability to increase an electrons velocity through 'hot phonon drag'. The 'hot phonon drag' effect is caused by a phonon temperature gradient within a material which causes phonons to drift in a particular direction. As the phonons move they can 'drag' electrons with them, increasing their velocity. In [59] this effect was shown to increase velocity by up to 20% in some circumstances; while 'phonon drag' was said to be the overriding hot phonon effect on electron velocity at sub-critical fields in pure GaAs at room temperature in [55]. Electron mobility in pure GaAs at room temperature was also found to increase in [57] when non-equilibrium phonon distributions are accounted for. When the lattice temperature was decreased in each

of these studies to 77K, hot phonons reduced electron mobility. The authors claimed that the reduction in lattice temperature narrows the phonon distribution eradicating phonon drag.

Hot phonons have also been shown to reduce electron mobility in [55] due to increased electron-phonon interaction. The increase in electron-phonon interaction leads to an increased randomisation of electron momentum. This is known as diffusive heating and has been shown in [55] to speed up momentum relaxation times, reducing the electron velocity. When lattice temperatures were reduced to 77K for pure GaAs and phonon drag wasn't present, hot phonons were shown to reduce electron mobility for sub critical fields in [55] and [57]. At sub critical fields the only way mobility could be reduced is due to an increased electron phonon interaction. This result is quite surprising since a significant phonon population is not expected at low fields and so hot phonon effects should be minimal. Both [55] and [57] are Monte Carlo simulations, any increased electron-phonon interaction would manifest itself as an increase in scattering rate. Unfortunately scattering rates are not presented in either publication.

As electron energy increases the impurity scattering rate, decreases. The increase in electron energy for a particular applied field caused by a hot phonon distribution in turn reduces the dominance of impurity scattering at low fields, increasing electron mobility. In doped GaAs at 77K, Mickevicius [55] finds that electron mobility

increases. This result implies that the decreased effect of impurity scattering in is more dominant than the effects of an increased POP scattering rate. At higher lattice temperatures with measurable impurity concentrations all of the effects mentioned will be competing and the situation becomes quite complicated. The most clear effect of a non-equilibrium phonon distribution is that the increase in electron energy will increase intervalley scattering, reducing electron mobility in the mid field regime and reducing the critical field. This is found to some extent for all conditions in [55] and [57].

The velocity field characteristics from our simulation with non-equilibrium phonons are compared to our model with equilibrium phonons in Figure 3.8. At very low fields the difference in velocities between the two models is insignificant. This difference is expected since at low fields the electron energy will be small and as such not many electrons will be capable of emitting a phonon, meaning the phonon population will not differ much from thermal.

Between 1kV/cm and 2.25kV/cm, we see a minor but noticeable reduction in average electron velocity when hot phonons are included. This can be attributed to the increase in electron phonon interaction. The peak velocity is around 18% lower

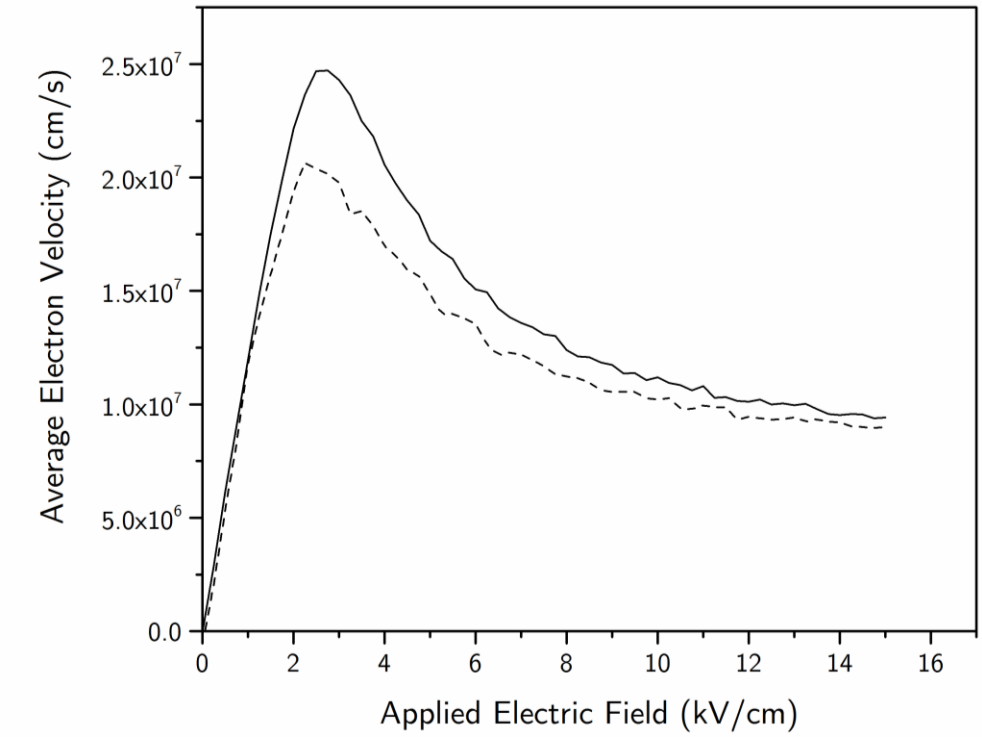

Figure 3.8 Velocity-field characteristics for equilibrium simulation (solid line) and non-equilibrium phonon simulation (dashed line).

when hot phonon effects are accounted for and the critical field is reduced by around 10%. Both of these effects are expected following the energy and occupancy relationships found in the previous section. The increase in average electron energy causes electrons to transfer to the upper valley at lower applied fields, reducing the critical field. More electrons will transfer to the upper valleys for any particular applied field, reducing the peak velocity. In the high field regime we find a consistent reduction in average electron velocity. The combination of increased electron energy, increased intervalley transfer and increased POP scattering rates will all be responsible for this. Figure 3.5 depicts the POP scattering rate as a function of electron energy at an applied field of 0.5kV/cm, 1.5kV/cm, 2.5kV/cm,

after a simulation time of 20ps. We notice that compared to thermal there is a significant increase in POP scattering for all energies. This increase in the POP scattering rate increases the rate of electron momentum randomisation which in turn reduces the electron velocity. This can be proven by analysing the momentum relaxation times for electrons at energies lower than that required for intervalley scattering.

The momentum relaxation time as a function of electron energy is found in Figure 3.9.has been calculated using equation 3.3 from [58],

$$\tau_m = \frac{\langle p_x \rangle}{eF} \qquad 3.3$$

where $\tau_m$is the momentum relaxation time $\langle p_x \rangle$ is the average electron momentum in the direction of the applied electric field ($\langle p_x \rangle = \langle v_x \rangle m^*$) and F is the applied electric field.

Electron momentum is found to relax faster when hot phonon effects are included. Figure 3.9 describes relaxation time as a function of energy and so allows us to single out the effect an increased POP rate has on electron momentum. It is clear that this effect is significant and decreases with energy. The increase in scattering rate is shown to be smaller at larger energies in Figure 3.5. This behaviour is

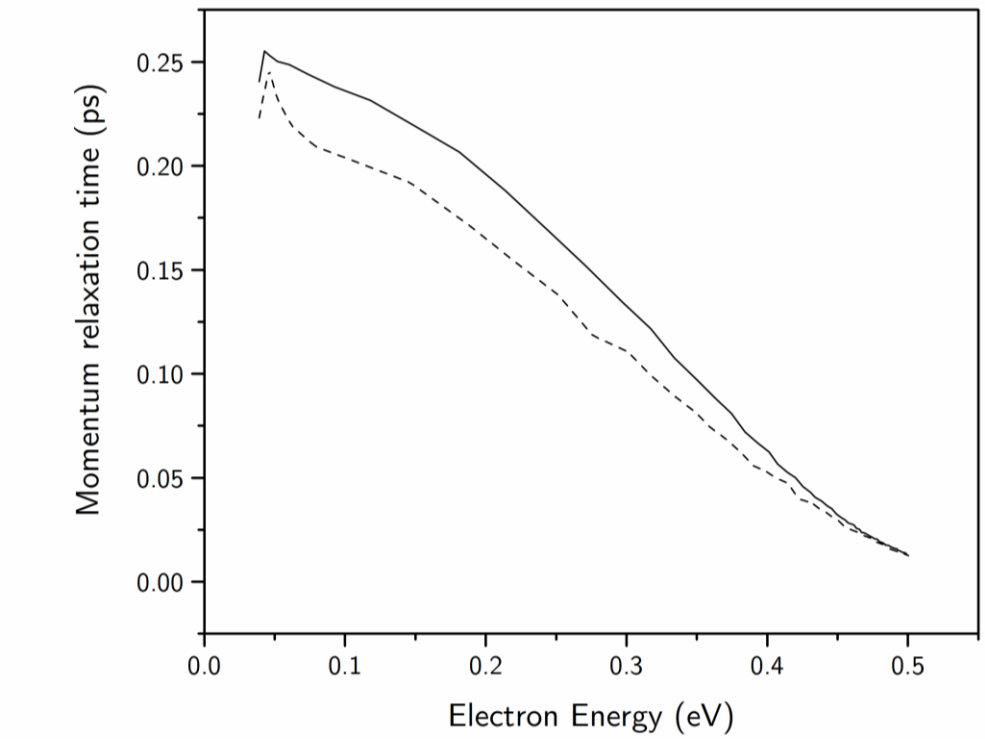

Figure 3.9 Momentum relaxation time for equilibrium simulation (full line) and non-equilibrium phonon simulation (dashed line).

consistent with the decreased difference between momentum relaxation rates in Figure 3.9. The steady state transport characteristics are clearly affected by the inclusion of phonon tracking within our simulation; though as expected the effects are not as pronounced as for GaN and AlN as presented Dyson [41].

3.3. Transient Characteristics

It is clear from the steady state analysis that the magnitude of hot phonon effects changes with applied electric field. In order to investigate the difference between the low-field, mid-field and high-field regimes, we analyse the transient characteristics of electron transport in $In_{0.53}Ga_{0.47}As$ for a variety of applied fields. The average electron energy as a function of simulation time is presented in Figure 3.10 and the

average electron velocity is presented as a function of simulation time in Figure 3.11. To aid in the analysis of electron velocity and energy the POP scattering rate is presented for an applied field of 2.5kV/cm after 1, 10 and 20ps in Figure 3.12.

3.3.1. *Low-field (0.5 kV/cm)*

At low applied fields the phonon population is not so different from thermal. The result is a very similar scattering rate for both the equilibrium and non-equilibrium simulations and a mostly insignificant level of phonon reabsorption. Consequently there is a negligible change in electron energy and a very slight decrease in electron velocity. Although any difference in each is not massively significant the minor differences are consistent with increased levels of phonon absorption and diffusive heating. As discussed earlier, according to the literature, it is in the low field regime where the phonon drag effect would be evident. The low field results for $In_{0.53}Ga_{0.47}As$ here do not exhibit any sign of 'phonon drag'.

3.3.2. *Mid-field (2.5kV/cm)*

The analysis of steady state results indicate that hot phonon effects are most prominent in the mid field regime. Figure 3.10 describes the average electron energy as a function of simulation time. The results show that hot phonons have minimal effect on electron energy in the mid field regime until around 5ps when the electron

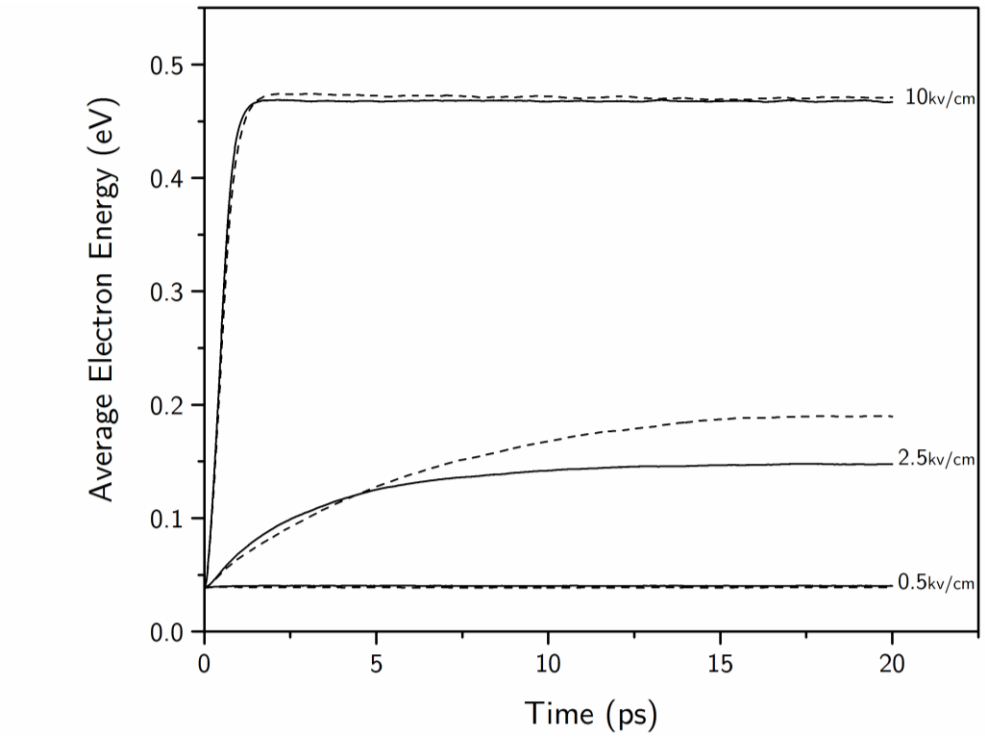

Figure 3.10 Average electron energy as a function of time for applied fields of 0.5, 2.5 and 10kV/cm. Dashed lines show non-equilibrium effects, solid lines signify equilibrium phonon model.

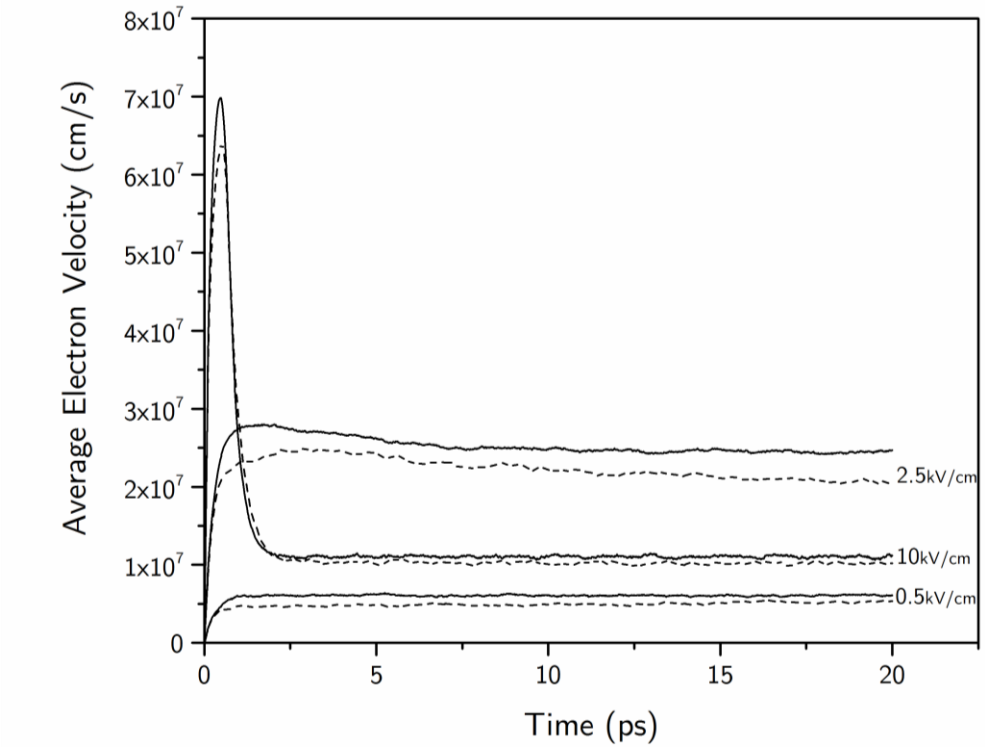

Figure 3.11 – Average electron velocities as a function of time for applied fields of 0.5, 2.5 and 10kV/cm. Dashed lines show non-equilibrium effects, solid lines signify equilibrium phonon model.

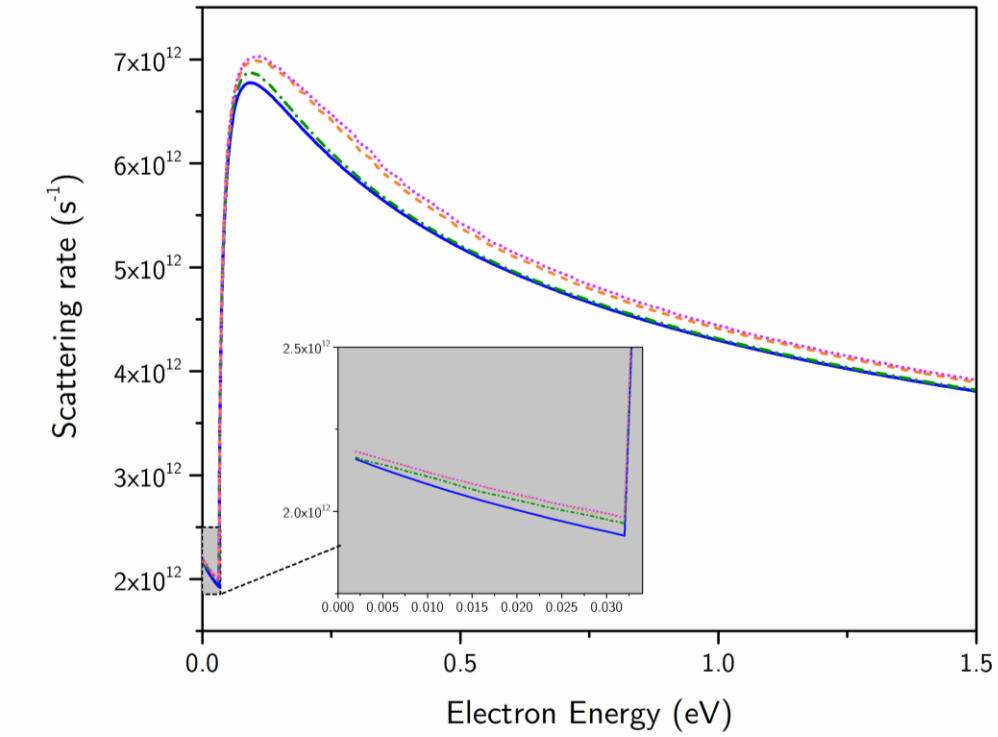

Figure 3.12 – Comparison of POP scattering rates at different simulation times. Results presented for an equilibrium phonon distribution (blue solid line) and the non-equilibrium phonon simulation at an applied field of 2.5kV/cm after 1ps (dot-dashed green line) 10ps (dashed orange line) and 20ps (dotted purple line). The inset provides a zoomed in view of the POP rate at energies less than the phonon energy (0.0327eV).

energy begins to increase relative to the thermal phonon simulation. After 20ps the electron energies of the equilibrium phonon simulation and non-equilibrium phonon simulation are 0.15eV and 0.19eV respectively. The POP scattering rate with an equilibrium phonon distribution is compared against the POP scattering rate from the non-equilibrium phonon simulation at an applied field of 2.5kV/cm after 1ps, 10ps and 20ps in Figure 3.12. For all energies the total scattering rate increases with simulation time. The increased scattering rate at energies lower than the phonon energy is associated with an increase in phonon absorption. This mechanism is shown to be responsible for the increase in electron energy in the hot phonon

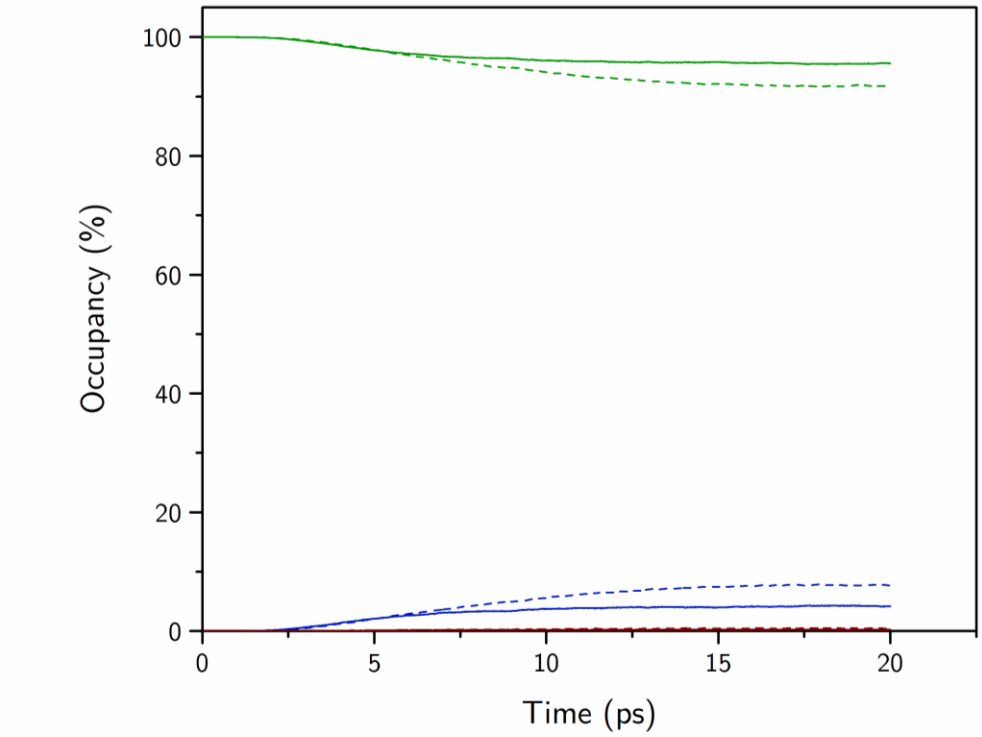

Figure 3.13 – Occupancy of Γ valley (Green lines) L valley (blue lines) and X valley (red lines) for equilibrium phonons (solid lines) and non-equilibrium phonons (dashed lines) as a function of simulation time for an applied field of 2.5kV/cm.

simulation. This increased absorption will also contribute to the redistribution of electron momentum which will in turn affect the electron velocity. Figure 3.11 shows the average electron velocity for the simulation with an equilibrium phonon distribution and a non-equilibrium phonon distribution as a function of simulation time. Electron velocity at 2.5kV/cm is significantly reduced when hot phonons are accounted for, at all times after around 1ps. At 5ps, in Figure 3.10, the electron energy for both simulations is the same, as is the valley occupancy (see Figure 3.13). At this point then we can say that any change in electron velocity is caused by a change in electron-phonon interaction. The average velocity of electrons in the equilibrium phonon simulation and the non-equilibrium phonon simulation at 5ps is

$3.25x10^7 cms^{-1}$ and $3x10^7 cms^{-1}$ respectively. Diffusive heating is therefore shown to be responsible for reducing electron velocity by around 7%. By the end of the simulation hot phonon effects have reduced the electron velocity from $3x10^7 cms^{-1}$ to $2.5x10^7 cms^{-1}$, more than a 17% reduction. By this point the increase in electron energy in the hot phonon simulation is significant, increasing the rate of intervalley transfer. This increase in intervalley transfer is presented explicitly in Figure 3.13. As would be expected from observing the electron energy it can be seen that more electrons are transferring to the upper valleys for increased electron energies at simulation times after 5ps. The increased upper valley occupancy is responsible for the further reduction in average electron velocity shown in Figure 3.11.

In [55] results are presented for GaAs under similar conditions. It is shown that for GaAs both average electron velocity and average electron energy increase because of hot phonon effects [57]. Contrary to the results shown here for $In_{0.53}Ga_{0.47}As$ Mickevicius [55] implies that the combined effects of phonon drag and the 'runaway' from impurity scattering in energy space is more significant than the transferred electron effect and diffusive heating. The results presented for InGaAs using the model outlined in this thesis for the mid-field regime have not found any evidence of a significant phonon drag effect.

3.3.3. *High-field (10 kV/cm)*

An important characteristic of the high field transient regime for III-V semiconductors and their ternaries is the velocity overshoot they exhibit. Velocity overshoots in the transient regime are observed at high applied fields when electrons rapidly acquire energy, entering the high energy regime where momentum relaxation times are smaller than energy relaxation times. Hot phonon effects were found to reduce the peak velocity of electrons in GaN and AlN in [41]. We show a similar effect in $In_{0.53}Ga_{0.47}As$ which is expected since the momentum relation time is decreased when hot phonons are accounted for as shown in Figure 3.9. The average electron energy shown in Figure 3.10 for the simulation with a thermal phonon distribution is almost identical to that from the non-equilibrium phonon simulation when a 10kV/cm field is applied. The electron energy rapidly increases with a high applied field meaning the dominant scattering mechanism quickly becomes intervalley scattering. When intervalley scattering is dominant the increases in the POP scattering rate caused by the increased phonon population is not significant enough to have an effect. With the same average energy electrons should start to transfer into the upper valleys at the same simulation time. In the high field regime with high electron energy we expect a significant phonon population. Diffusive heating from the broadened phonon distribution and increased scattering rate is hence shown to be the cause of the reduced peak velocity and saturation velocity.

Both [55] and [57] show the same reduction in the saturation velocity which is consistent with our findings.

3.4. Summary

In this chapter hot phonon effects on steady state and transient transport characteristics in $In_{0.53}Ga_{0.47}As$ have been investigated. Firstly, a reduction in critical field, peak velocity and saturation velocity was found in the steady state regime. In the transient regime the peak and saturation velocities were found to be lowered by a hot phonon distribution. We have shown that the dominant hot phonon effects in our simulation are diffusive heating and phonon re-absorption. Phonon drag is not found to be present. The energy difference in our two simulations does not manifest itself until relatively large energies when compared to previous works on GaAs in [55][57] meaning any 'runaway' from impurity scattering is not found to be significant.

Chapter 4. GaAs Gunn Devices

The demand for electronic devices capable of operating in the millimetre frequency range at room temperatures, with a low power consumption and manufacturing cost is growing [60][61]. GaAs Gunn technology is a relatively mature technology with many devices available from commercial vendors. Despite the amount of knowledge amassed surrounding GaAs based Gunn technology it remains an active area of research [62]–[64]. Within a research environment devices with an active region length of 1μm have been shown to operate at frequencies of up to 120 GHz [64].

While Monte Carlo works surrounding GaAs devices are available in the literature they tend to have been undertaken a number of years ago. Limitations on available computer resources at that time mean that these models have been limited to tens of thousands of particles [65][1]. Due to the statistical nature of Monte Carlo techniques a more precise result can be obtained using an improved resolution. This can be achieved by using a finer mesh or by increasing the number of simulated particles [66]. A GaAs Gunn device originally simulated by Tully in 1983 [1] is then

simulated using the in-house developed device simulator described in Chapter 2 with a finer mesh and more superparticles. Results from the two models are then compared to ensure validity of the model described in Chapter 2. The model described in chapter 2 uses a finer mesh and more superparticles than the original study by Tully. The effect that this has on the results will be explored.

4.1. Results

In this chapter a Monte Carlo simulation of an N++ - N - N+ - N++ notched GaAs Gunn diode undertaken by J. Tully in 1983 [1] is recreated with a finer mesh and considerably more superparticles. A schematic of the device design is presented in Figure 4.1. The original simulation found that when the device interacted with an external circuit it oscillated in accumulation mode at 70 GHz[1]. Electrons are shown to overshoot peak average velocities and a 'dead zone' between the cathode and the charge accumulation, where electrons are not able to gain sufficient energy to transfer to the upper valleys is found. A 50% doping notch is included at the cathode side of the active region to provide an initial high field region designed to accelerate electrons across the active region; in theory reducing the size of the 'dead zone'[1].

The simulation performed by Tully contains 17295 superparticles and 144 cells each with a width of 0.18×10^{-5}cm [1]. In the following simulation approximately 3.9×10^{6} superparticles are present within the device, 2052 cells are simulated each with a

width of $1x10^{-7}$cm. To account for the reduced cell spacing the time spacing must also be reduced to ensure that electrons do not travel further than one grid point over a single time step. The simulation undertaken by Tully uses a time step of $0.5x10^{-14}$s, this has been reduced to $0.5x10^{-15}$s for the following simulation.

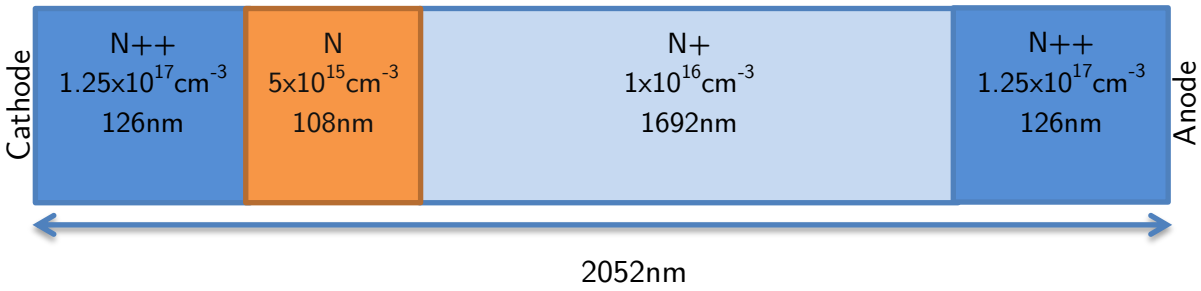

Figure 4.1 - Schematic of 1-dimensional GaAs Gunn device simulated by Tully [1] (not to scale).

Device structure and device specific simulation parameters are summarised and presented in Table 4.1. Three valleys are simulated (Γ-L-X) using the $\mathbf{k}.\mathbf{p}$ approximation. It is not clear from the original study what material parameters were used for the simulation. The material parameters used to collect the results presented in this thesis are presented in Table 4.2. The investigation by Tully pre-dates the sources of these material parameters and so it is likely that the device characteristics will be slightly different due to an assumed discrepancy in material parameters used. Any slight discrepancy in material parameters could manifest itself as a change in electron mobility with a difference in valley separation producing a different rate of intervalley scattering. Any differences found between the two models will be discussed as part of the relevant analysis.

Parameter (units)	Device
Total length of device (nm)	2052
Length of anode and cathode (nm)	126
Length of active region (nm)	1800
Total number of grid spaces	2052
Length of grid spacing - dx (nm)	1.0
Doping density at anode and cathode (cm^{-3})	$1.25x10^{17}$
Doping density in active region (cm^{-3})	$1.0x10^{16}$
Number of particles per cell	10000
Time step – dt (fs)	0.5
Lattice temperature (K)	300
Applied potential (V)	3V
Number of time steps	120,000
$n_0 L$ (cm^{-2})	$1.8x10^{12}$

Table 4.1 - Simulation parameters used for the re-creation of the device modelled by Tully [1].

The saturation velocity and critical field are useful when analysing device behaviour and are material dependent. Rather than assume these values from Tully [1], the basic EMC model described in Chapter 1 has been used to investigate the bulk transport characteristics of GaAs using the exact material parameters used in the device model. The saturation velocity and critical field have been found from Figure 1.6 and the Kroemer criterion has been calculated; these results are summarised in Table 4.3.

Parameter (units)	GaAs
Density (kg/m^3)	5360
Longitudinal sound velocity (ms^{-1})	5240
Transverse sound velocity (ms^{-1})	2480
Non-polar optical deformation potential coupling constant (eV/m)	10^{11}
Intervalley scattering coupling constant (eV/m)	10^{11}
Acoustic deformation potential (eV)	7
Piezoelectric constant e_{14} (Cm^{-2})	-0.16
Energy gap (eV)	1.424
Energy separation between L valley and Γ valley (eV)	0.296
Energy separation between X valley and Γ valley (eV)	0.52
Number of equivalent L valleys	4
Number of equivalent X valleys	3
Effective mass in Γ valley	0.067
Effective mass in L valleys	0.35
Effective mass in X valleys	0.58
Polar optical phonon energy (eV)	0.0353
Lattice constant (Å)	5.186

Table 4.2 - Material parameters for GaAs at 300K [67]–[70] .

Parameter	Value
Saturation velocity (v_s)	$6.7\text{x}10^{6}\text{cms}^{-1}$
Critical Field	4.25kV/cm
Differential mobility in NDR region (μ_d)	$6.36\text{x}10^{-6}\text{cm}^{2}\text{V}^{-1}\text{s}^{-1}$
Static dielectric constant for GaAs (ε_r)	12.9
Kroemer criteria $\left(\frac{3\varepsilon_r\varepsilon_0 v_s}{q\lvert\mu_d\rvert}\right)$	$2.26\text{x}10^{11}\text{cm}^{-2}$

Table 4.3 – Transport properties of GaAs taken from Figure 1.6.

In the original investigation Tully presents charge density, electric field and average electron velocity as a function of device position for various simulation times. The evolution of these same characteristics is analysed for the in-house model and compared to the characteristics presented by Tully [1]. The number of electrons leaving the anode as a function of time is presented and compared to the current waveform, presented in Figure 4 in the original research by Tully [1]. The study by Tully assumes a contact area which has been used to scale the number of electrons leaving the contact into an electrical current. We feel that for a 1-dimensional simulation this scaling is largely arbitrary and so present the number superparticles leaving the anode during each time step as a function of simulation time instead.

The charge density as a function of device position for simulation times between 4 and 24ps is presented in Figure 4.2. Charge density is calculated using the number of superparticles within each cell and the size of that cell. It is represented as the number of carriers per cm^3. It is found that an accumulation of charge is present

around the middle of the active region after 4ps. This accumulation of charge grows with time as it propagates towards the anode. It is expected that as the charge accumulation travels towards the anode that an increasing electric field leads to an increasing difference in velocity between electrons within the domain and electrons outside of it. This effect causes the charge distribution to become steeper close to the anode as can be seen in Figure 4.2. Once the charge accumulation makes contact with the anode after approximately 20ps it is found that the charge accumulation does not fully annihilate and becomes trapped. This phenomenon is known as a stationary or trapped anode domain. It has been shown that the existence of a trapped domain depends on doping notch length, applied potential and doping density [71]. Under a constant applied bias a stationary anode domain is expected within a GaAs device when the n_0L product is greater than $5x10^{11}cm^{-2}$ or if the doping density is greater than $5x10^{14}cm^{-3}$ [40]. Both of these conditions are met, the n_0L product of the device presented here is $1.8x10^{12}cm^{-2}$ and the doping density of the active region is $1.0x10^{16}cm^{-3}$. This is a clear contradiction with the results presented by Tully [1]. Before investigating the reasoning behind the different mode of operation which has been observed the electric field and number of electrons leaving the anode each time step is investigated to ensure the simulation is working as intended.

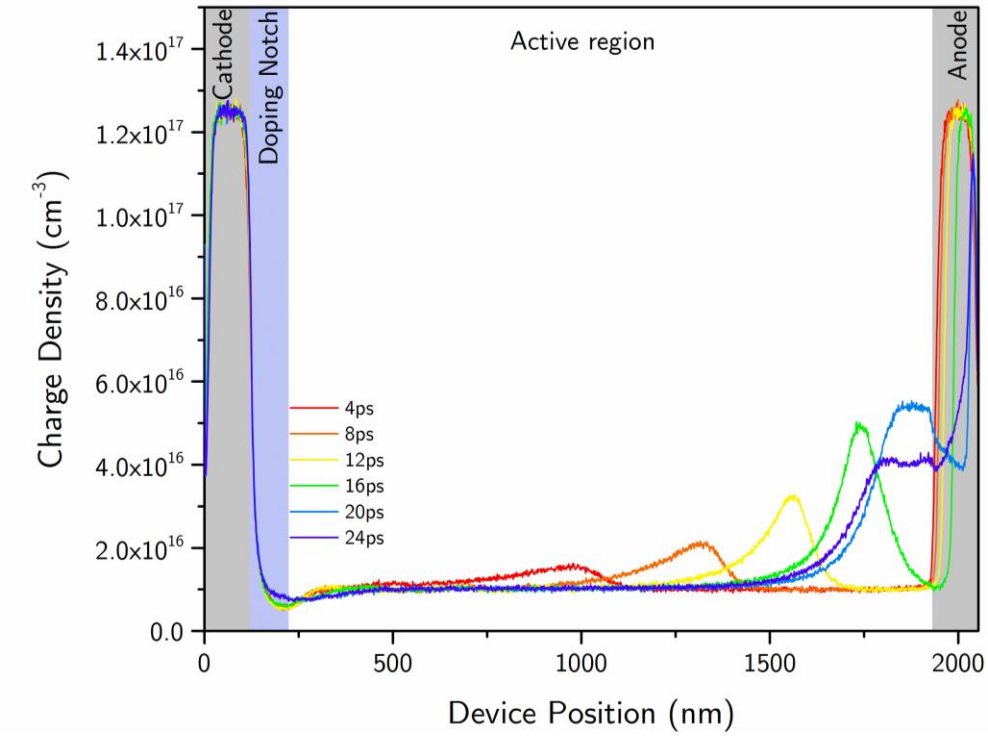

Figure 4.2 - Charge density as a function of device position for simulation times between 4 and 24ps.

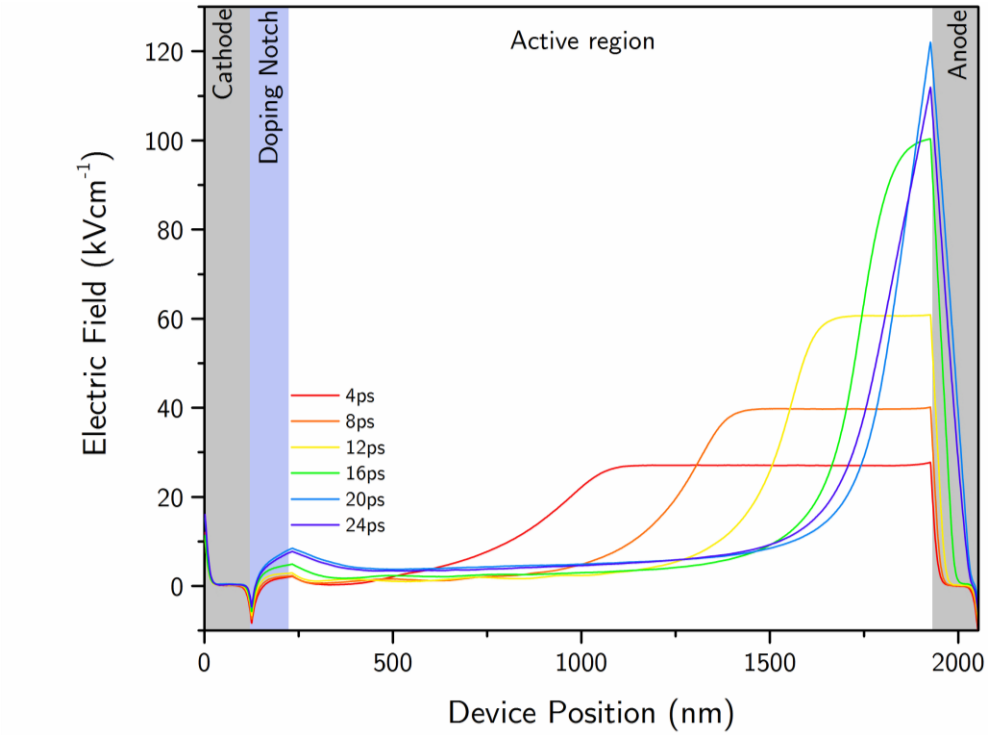

Figure 4.3 - Electric field as a function of device position for simulation times between 4 and 24ps.

The electric field profiles presented here have been calculated using the charge density profile and the Successive Over-Relaxation (SOR) method as outlined in Chapter 2. As expected a peak in electric field is found around the doping notch. The electric field behaviour is also consistent with the charge density profile. An increase in electric field is found at the device position where an accumulation of charge can be found.

In the space between the accumulation and the anode the field is shown to remain high until the anode when it reduces. As the charge densities increases in size the magnitude of the electric field in the accumulation region also increases. Between 20 and 24ps the electric field stays around the same, confirming the presence of a stationary anode domain.

The number of electrons leaving the anode as a function of simulation time is presented in Figure 4.4. The number of superparticles leaving the anode each time step is found to sharply increase around 20ps. This spike is consistent with the time at which the domain begins to interact with the anode contact region. This behaviour is consistent with the background literature which states that the current spikes when a charge accumulation annihilates at the anode region of a device and should drop during domain formation [38]. It can be seem from Figure 4.4 that the number of electrons leaving the anode doesn't drop significantly after 20ps further demonstrating the presence of a stationary anode domain.

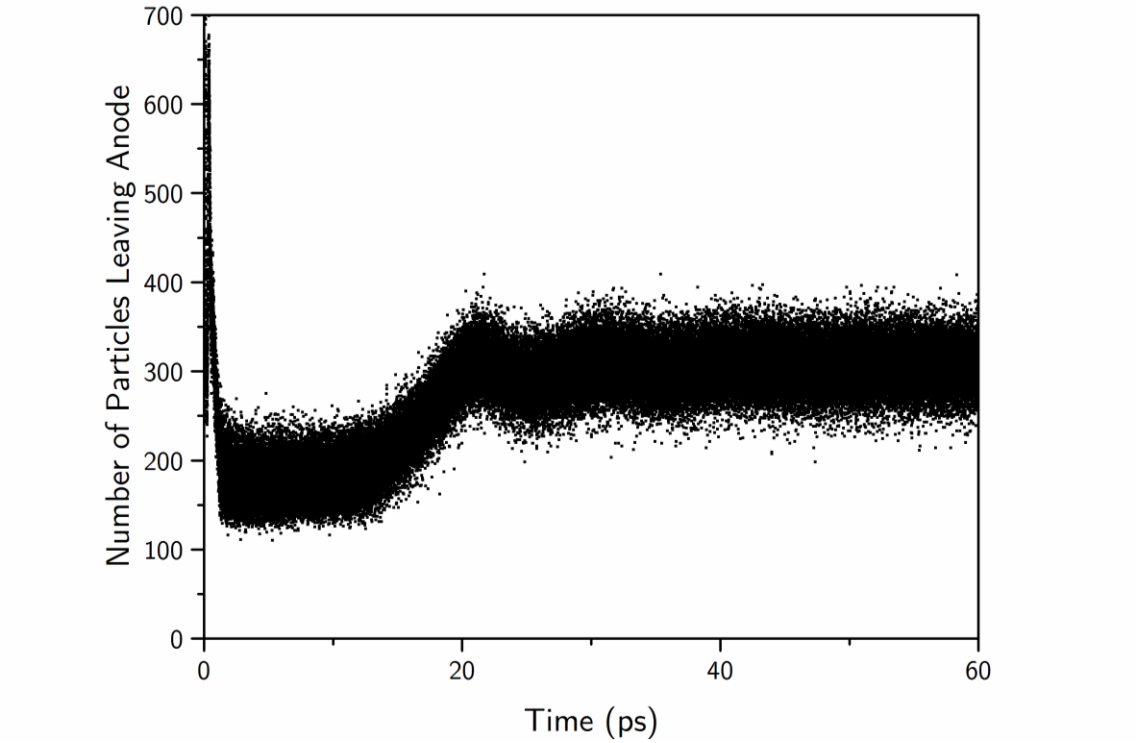

Figure 4.4 The number of electrons leaving the device at the anode every time step as a function of simulation time.

The results published by Tully [1] show a sinusoidal current with charge accumulations growing periodically within the centre of the device, propagating towards the anode where they annihilate. The two models clearly do not agree. The device which was simulated by Tully [1] is subject to an external oscillator circuit whereas the results presented here have been produced by applying a constant voltage of 3V across the device. In an attempt to un-trap the stationary anode domain and replicate the function of an external oscillating circuit a sinusoidal potential has been applied to the device.

4.1.1. *Sinusoidal Applied Potential*

An RF potential (V_{AC}) is imposed onto the DC bias (V_{DC}) as is standard practise when modelling Gunn diodes [72][73]. The sinusoidal potential has been tuned using equation 4.1 to best reflect the potential being applied to the device in the original publication. The sinusoidal potential applied to the device takes the form:

$$V = V_{DC} - V_{AC}\sin(2\pi ft) \tag{4.1}$$

Where V is the applied potential, V_{DC} is the DC offset and V_{AC} is the AC component of the potential, f is the desired frequency of the applied potential and t is simulation time. The values used to replicate the potential profile presented by Tully are given in Table 4.4. The resulting potential profile is represented in Figure 4.5 and was used to compare with figure 4 in the original research paper by Tully [1].

Parameter	Value
V_{DC} (V)	3.4
V_{AC} (V)	2.6
Frequency (Hz)	7×10^{10}

Table 4.4 – The Parameters used to replicate the potential profile presented by Tully.

Charge density as a function of device position for simulation times between 23 ps and 34 ps are presented in Figure 4.6 and Figure 4.7.

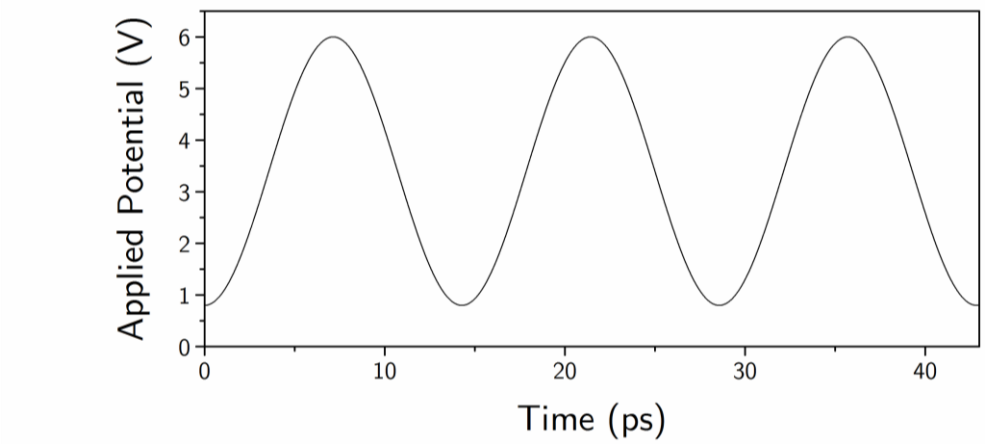

Figure 4.5 – Applied potential as a function of simulation time.

After 23ps a significant accumulation of charge is present within the active region. After 24ps the applied potential is reducing and the amount of charge within the accumulation is shown to reduce until around 28ps when the charge accumulation makes contact with the anode, at which point the potential reaches its minimum. At 29ps a domain is shown to slowly begin to grow until a significant accumulation of charge is present after 34ps and the process repeats itself. The general behaviour of the charge density is in agreement with the results published by Tully [1]. In the original Tully publication the net change in electrons per mesh spacing is presented as a means of communicating charge density [1]. Since the number of particles simulated by Tully was significantly different to the number used in this simulation a direct comparison is difficult. Instead a direct comparison of electric field profiles is undertaken.

The electric field as a function of device position for simulation times between 22ps and 28ps is presented in Figure 4.8. The electric field profiles are presented in figure

5 in the publication by Tully [1]. The peak fields presented in the publication by Tully [1] are around 80kV/cm, these occur for potentials of 5.9V and 4.15V as seen in the voltage waveform presented by Tully. From this point, as the potential reduces with time the peak electric field gets smaller reaching around 20kV/cm at 0.8V. Using the potential profile given in Figure 4.5 the simulation times at which these potentials are applied across my model can be found. The peak electric fields at these applied potentials are then compared with those presented by Tully to check equivalency. In Figure 4.8 the electric field at 22ps represents the electric field at 5.9V. The electric field is at its maximum at this potential and stays the same when the potential drops to 4.15V, following the same trend as the results published by Tully [1]. The electric field then drops with time until it reaches its minimum after 28ps with an applied potential around 0.8V, again, following the same trend as the results presented by Tully. The maximum electric field shown in Figure 4.8 is 120kV/cm compared with 80kV/cm in Tully [1].The minimum electric field is around 55kV/cm in Figure 4.8 compared with 20kV/cm in the original Tully publication [1]. The discrepancy between the magnitudes of the electric fields is expected due to the assumed differences in material parameters used in each simulation and the difference in number of simulated superparticles. With the relatively small number of particles used in the original Tully simulation [1] the peak electric field is calculated according to the accumulation of only a few hundred particles compared to the thousands of particles present in the results presented

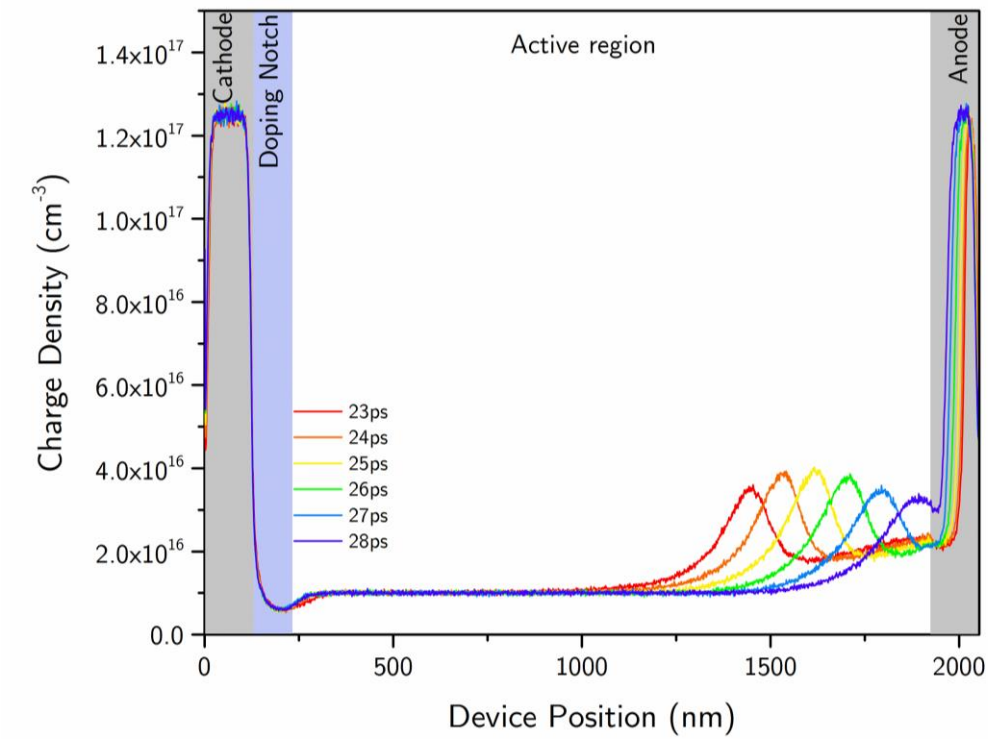

Figure 4.6 - Charge density as a function of device position for simulation times between 23ps and 28ps

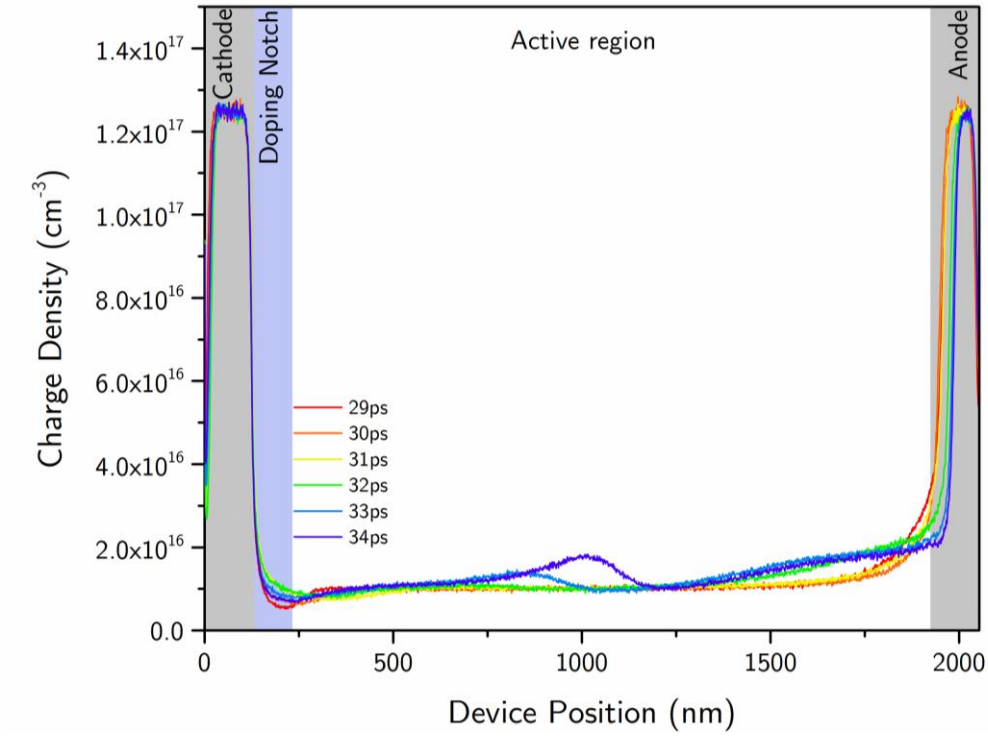

Figure 4.7 - Charge density as a function of device position for simulation times between 29ps and 34ps

here. Despite the discrepancy in the size of the electric fields, the evolution of the potential and electric field is consistent between the two models.

Fundamental to the analysis of how Gunn devices operate is the electron velocity profile. The average electron velocity per mesh spacing as a function of device position for simulation times between 23ps and 27ps is presented in Figure 4.9. The average electron velocity profile is similar when the results in Figure 4.9 are compared with those from the original study by Tully [1]. For both sets of results the electron velocity peaks around the doping notch. It then reduces to a stable value until a charge accumulation is present when electron velocities drop to around the saturation velocity. While the velocity profile for each set of results is the same the magnitude of electron velocities is different. Most notably the charge accumulation in Tully [1] is shown to travel at around $1.1 \times 10^{7} cms^{-1}$ while the charge accumulation in

Figure 4.9 is shown to travel at around $6.7 \times 10^{6} cms^{-1}$. An investigation into the recent literature on GaAs suggests that the saturation velocity in doped GaAs at room temperature is much less than the $1.1 \times 10^{7} cms^{-1}$ used by Tully [1]. Two Monte Carlo models undertaken in 2011 [74] and 2013 [75] present saturations velocities of around $V_s \sim 8.0 \times 10^{6} cms^{-1}$ while a full band Monte Carlo model has found saturation velocities of around $6.5 - 7.0 \times 10^{6} cms^{-1}$ [76]. These results are shown to

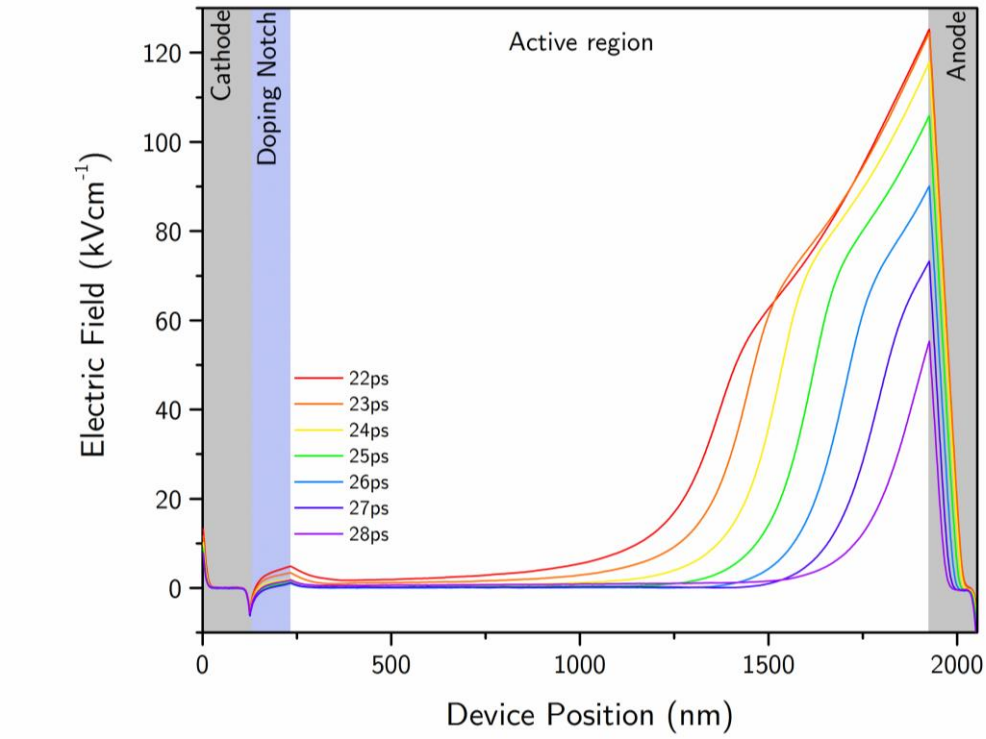

Figure 4.8 – Electric field as a function of device position for simulation times between 23ps and 28ps

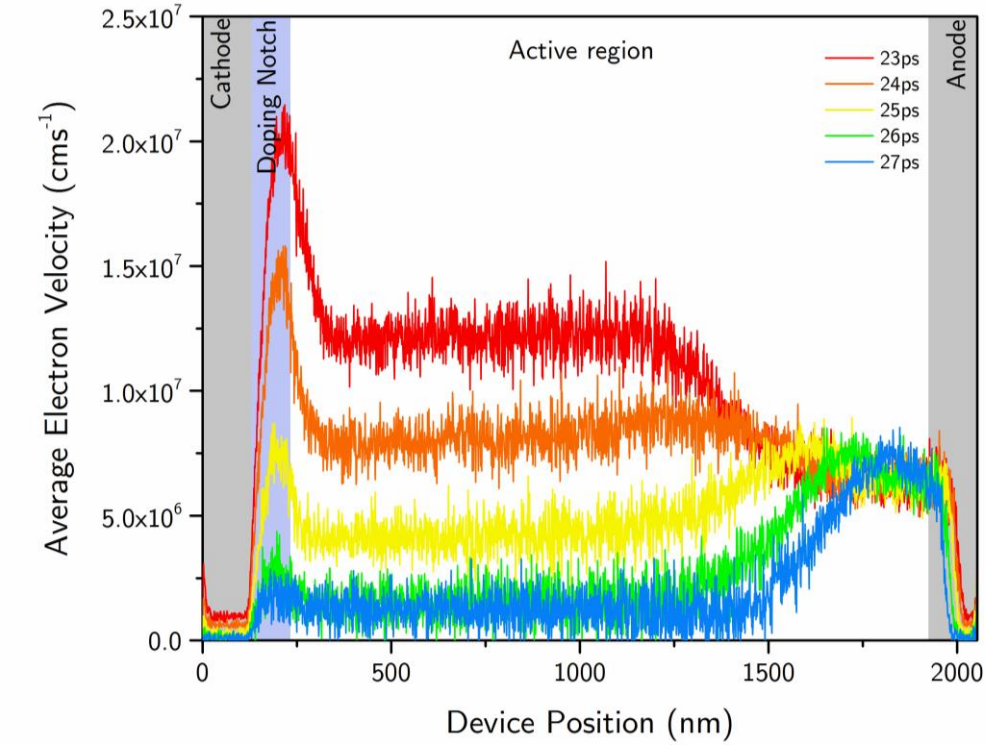

Figure 4.9– Average electron velocity per cell as a function of device position for simulation times between 23 and 27ps.

be consistent with data taken from a drift diffusion model and with experimental data in [76].

In order to explain how the size of the charge accumulation evolves, the velocity profile of electrons within the device is investigated for various simulation times. As was seen in Figure 4.6 there is a significant accumulation of charge at 23ps. The number of particles within the charge accumulation stays around the same until 26ps when the number of electrons within the accumulation starts to reduce. For simulation times of 23ps and 24ps the electrons in the space behind the charge accumulation are travelling faster than the saturation velocity (See Figure 4.10), meaning electrons will be joining with the charge accumulation. At simulation times 25ps and onwards in Figure 4.9 it can be seen that the average velocity of electrons in the space behind the accumulation is less than the velocity of the domain due to the reduced applied potential and so electrons will begin to drop out of the accumulation. This can be observed in Figure 4.6 as the number of electrons within the accumulation begins to reduce.

The operating frequency of the Gunn device is also investigated and compared with the results published by Tully [1]. The number of particles leaving the anode as a function of time is plotted alongside the potential in Figure 4.10 (A re-creation of Figure 4 in Tully [1]). When a charge accumulation meets the anode a sharp increase in current can be observed. The number of electrons leaving the anode is

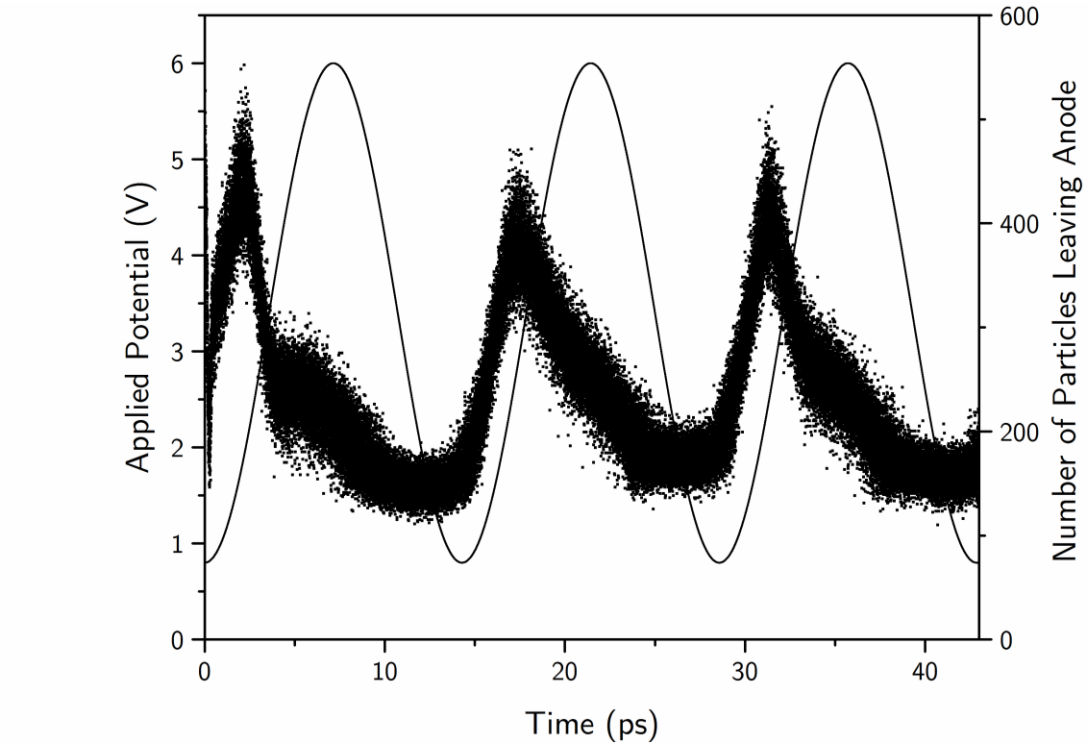

Figure 4.10 – A scatter plot showing the number of superparticles leaving the anode every time step as a function of simulation time. The scatter plot is accompanied by a line representing the applied potential as a function of simulation time.

analogous to the current and so can be used to estimate operating frequency, rather than estimating transit time from charge density plots. It is shown that the number of superparticles leaving the anode is in agreement with the current waveform published by Tully. Using the times at which the number of particles leaving the anode peaks, the transit time of the accumulation mode is found to be around 13.9ps which corresponds to an operating frequency of around 72 GHz.

The phase difference between the current and applied voltage is an important characteristic of Gunn devices. For the best negative resistive response, the current would be out of phase with the applied potential by 180 degrees. Dunn and Kearney [72] investigated the effects of active region length on the phase difference between

current waveform and the applied potential. By using different active region lengths they attempted to manipulate the transit time for the charge accumulation so that it annihilated at the anode at the same time as the driving potential was at its smallest. Such an investigation into GaAs is outside of the scope of this thesis.

4.2. Summary

Results from a Monte Carlo model have been presented for a recreation of a 70 GHz Gunn device originally simulated by Tully in 1983 [1]. The device is shown to operate in accumulation mode with a considerable 'dead zone'. It has been shown that with a constant applied potential this device operates with a stationary anode domain. A time dependent potential is shown to be required for a device of this design to function in accumulation mode. The model presented here is shown to agree with the results presented by Tully to a reasonable estimate considering the uncertainty surrounding material parameters. Significantly less noise is present in average electron velocity data showing the increased precision offered by a Monte Carlo model with a finer mesh and an increased number of superparticles.

Chapter 5. GaN Gunn Devices

GaN has been suggested as a material for use in Gunn devices due to its large band gap, high electron mobility and the large range of fields which exhibit negative differential mobility. GaAs diodes have been shown to oscillate at frequencies between 25-166.7 GHz [63], [64], [77], depending on channel length. InP based Gunn diodes have been shown to oscillate between 56.3-375 GHz depending on channel length [63][78][79]. To achieve such high operating frequencies using GaAs or InP small channel lengths must be used. The small channel lengths mean only a small potential can be applied across the device before it fails which limits the available output power. In an attempt to maintain high frequency operation and increase power output, innovative device designs such as synchronising the domains from multiple transit regions have been investigated [80][39]. In 2000 Pavlidis et al. [6] fabricated the first GaN NDR diode. GaN NDR diodes provided double the frequency of a GaAs diode with the same active layer thickness (65-95 GHz rather

than 27-40 GHz) and an increased output power density ($2x10^5$ W/cm^2 for the GaN device compared to ~10^3 W/cm^2 for GaAs devices [6]).

A number of theoretical studies on Gunn devices are available within the literature. Pavlidis et al. modelled a GaN Gunn diode using the commercial simulator Medici [6]. Voltage and current plots are presented which, while useful, do not provide a detailed analysis of the physical mechanisms responsible for Gunn behaviour. In 2008 Pilgrim published results obtained from Monte Carlo simulations, showing charge density and electric field as a function of device position. Pilgrim simulates 10,000 particles and the devices are shown to only operate in the charge accumulation regime. In 2012 GaN based Gunn diodes were re-visited by Momox using Drift Diffusion (DD) and Hydrodynamic (HD) based models [81]. Momox presents field and charge density plots as a function of device position. The simulated devices are shown only to operate in the accumulation mode. Notched devices are not investigated and only the active region is simulated. To the best of our knowledge a theoretical study showing a Gunn device working in dipole mode is not available within the literature.

The energy separation between the Γ valley and the L valley used in the studies by Momox [81] and Macpherson [44] is around 2eV. In 2011 this valley separation was revised down to 1.2eV [34]. Intervalley transfer is fundamental to the operation of Gunn diodes which makes the energy separation a critical parameter for any related

simulations. The energy separation used to obtain the results presented in this thesis is the much lower revised value of 1.2eV. Latest research has indicated that the energy separation is around 0.9 +/- 0.08eV [82].

In the following chapter results are presented for a GaN Gunn diode operating in accumulation mode. The processes responsible for devices operating in dipole mode are then explored before detailing the modifications required to the GaN Gunn device so that dipole domains are formed. Results are then presented for a GaN Gunn diode operating in dipole mode obtained using our in-house developed Monte Carlo model designed specifically for investigating electronic devices.

5.1. Results - Bulk GaN

Before simulating a GaN device it is important to find various transport characteristics to be used as part of device design and analysis. Using the EMC model described in Chapter 2 with the same material parameters which are used throughout the following chapter (See Table 5.3), the steady state characteristics of bulk GaN are found (Figure 5.1). A cosine band approximation is used for the gamma valley while a parabolic approximation is used for the M-L and A valleys. The steady state results have been used to calculate both differential mobility (μ_d) in the region of negative differential mobility and saturation velocity (v_s). These values can then be used to calculate the Kroemer criteria. This data is summarised in Table 5.1.

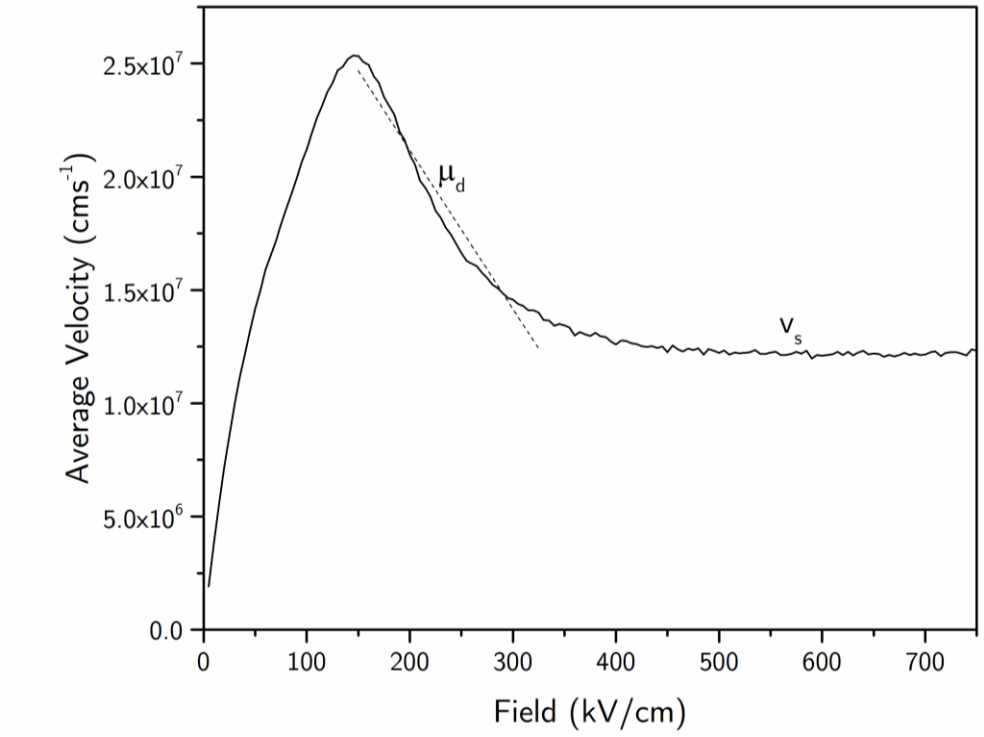

Figure 5.1 - Velocity field characteristics for bulk GaN. V_s represents the saturation velocity (v_s) while the dashed line, μ_d, is used to represent the differential mobility (μ_d) in the region of negative differential mobility.

Parameter	Value
Saturation velocity (v_s)	$1.22\text{x}10^{7}\text{cms}^{-1}$
Differential mobility in NDR region (μ_d)	$7.01\text{x}10^{1}\ \text{cm}^2\text{s}^{-1}\text{V}^{-1}$
Kroemer criteria $\left(\frac{3\epsilon v_s}{q\lvert\mu_d\rvert}\right)$	$2.57\text{x}10^{12}\text{cm}^{-2}$

Table 5.1 - Values for v_s,μ_d and the Kroemer criteria for GaN.

5.2. Results – Accumulation mode

In the following section results are presented using the methods outlined in chapter 2.3 for a GaN based Gunn device. Using different device designs we are able to simulate Gunn diodes operating in both accumulation mode and dipole mode. A table outlining the device parameters for each operating regime will be presented at the beginning of the relevant section. The material parameters for Wurtzite GaN at

300K have been taken from [19], [29]–[34] and are presented in Table 5.3. Material parameters are the same for both the accumulation mode and dipole mode simulations. Simulation specific parameters such as doping density, device size, mesh spacing and time step are presented in Table 5.2. A schematic of the simulated device operating in accumulation mode is presented in Figure 5.2.

Parameter (units)	Device
Total length of device (nm)	2100
Length of anode and cathode (nm)	420
Length of active region (nm)	1260
Total number of grid spaces	1000
Length of grid spacing - dx (nm)	2.1
Doping density at anode and cathode (cm^{-3})	$2x10^{18}$
Doping density in active region (cm^{-3})	$2x10^{17}$
Number of particles per cell	10,000
Time step – dt (ps)	$5x10^{-4}$
Lattice temperature (K)	300
Applied potential (V)	40
Number of time steps	60,000
$n_0 L$ (cm^{-2})	$2.52x10^{13}$

Table 5.2 – Simulation parameters used for 1D 3k GaN Gunn device operating in accumulation mode.

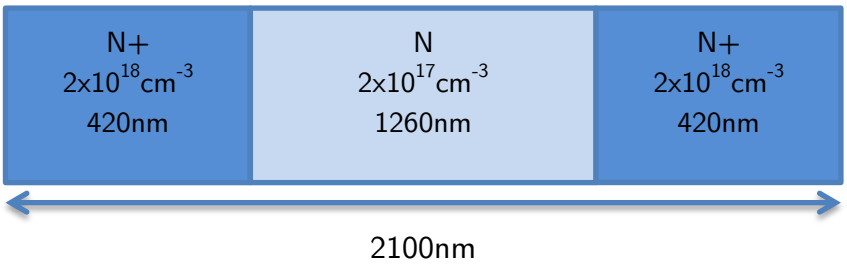

Figure 5.2 – Schematic of 1-dimensional Gunn device operating in accumulation mode.

The number of particles per cell given in Table 5.2 refers to the number of superparticles per cell in the N+ areas of the anode and cathode. According to the size and doping density of the device we estimate that around 9.5×10^6 superparticles are present within the device.

In the following section charge density, electric field and average electron velocity are all presented as a function of device position. The presented data is used to analyse the formation of accumulation layers before analysing the operating frequency of the device and testing the validity of the Kroemer criteria.

Charge density as a function of device position is presented in Figure 5.3 for simulation times between 1 and 6ps. Charge is shown to accumulate around the cathode and then propagate towards the anode. Unlike the Monte Carlo study by Pilgrim [44] the charge accumulation is present without a doping notch. The sharpness and magnitude of the accumulations is comparable with the results

Parameter (units)	GaN
Density (kg/m^3)	6150
Longitudinal sound velocity (ms^{-1})	7641
Transverse sound velocity (ms^{-1})	4110
Non-polar optical deformation potential coupling constant (eV/m)	10^{11}
Intervalley scattering coupling constant (eV/m)	10^{11}
Acoustic deformation potential (eV)	8.3
Piezoelectric constant e_{15} (Cm^{-2})	-0.3
Piezoelectric constant e_{31} (Cm^{-2})	-0.36
Piezoelectric constant e_{33} (Cm^{-2})	1
Energy gap (eV)	3.39
Energy separation between M-L valleys and Γ valley (eV)	1.2
Energy separation between A valley and Γ valley (eV)	2.1
Number of equivalent M-L valleys	6
Number of equivalent A valleys	6
Effective mass in Γ valley (m_0)	0.2
Effective mass in M-L valleys (m_0)	1
Effective mass in A valleys (m_0)	1
Polar optical phonon energy (eV)	0.0912
Lattice constant (Å)	5.186

Table 5.3 – Material parameters for GaN at 300K [19], [29]–[34].

presented by Momox [81]. There is a clear trailing edge of charge visible at the cathode side of the layer while the front edge has a much sharper gradient. The

trailing edge represents the electrons which have a high average velocity and are beginning to join the charge accumulation. As these electrons enter regions of high field their velocity will saturate, and begin to move at the same velocity as the charge accumulation, hence the sharp leading edge at the front of the accumulation.

The electric field as a function of device position is presented in Figure 5.4 for simulation times between 1 and 6ps. We see the field is clearly separated within the active region resulting in a high field region at positions in front of the accumulation layer and a low field region at positions before the layer. The field separation is much more pronounced than that shown by Pilgrim [44], this can be explained by the difference in the number of superparticles simulated in the active region. With fewer particles the statistical noise associated with the Monte Carlo method becomes more prominent, essentially reducing the resolution of the simulation. The sharpness of the field separation in Figure 5.4 is consistent with the results presented by Momox [81] and the background theory [83]. The increase in electric field due to the accumulation of charge is fundamental to the device function. In order for accumulation layers to form the high field regime must be above the critical field while the low field region must be below critical. Electrons in the high field regime are more likely to occupy the upper valleys where they have a

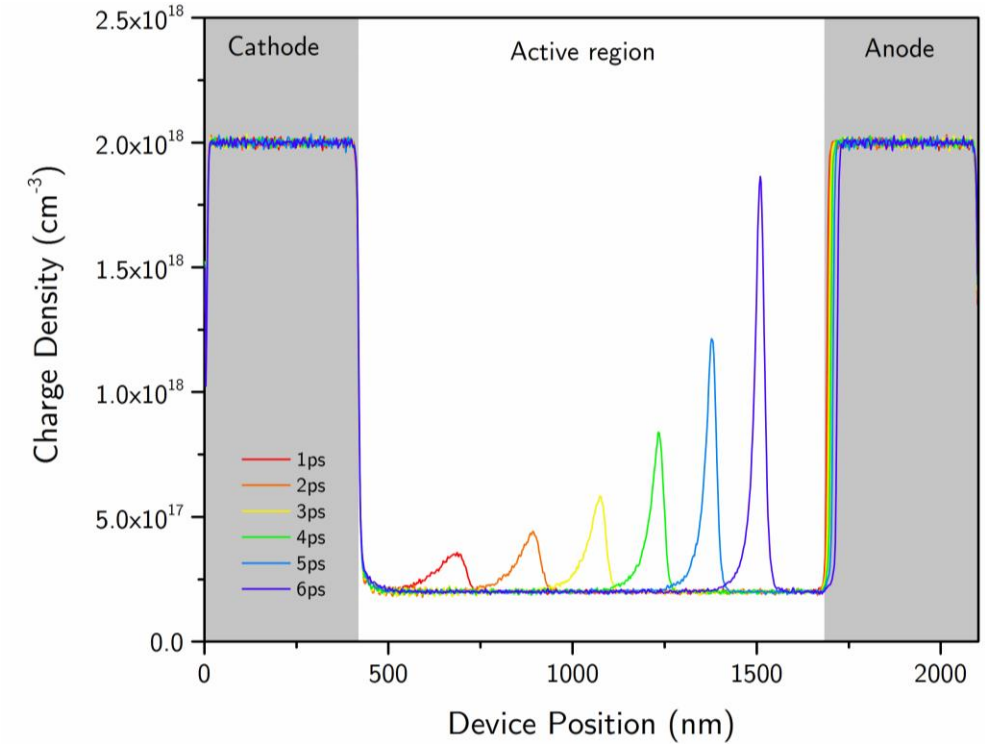

Figure 5.3 – Charge density as a function of device position for simulation times between 1 and 6ps.

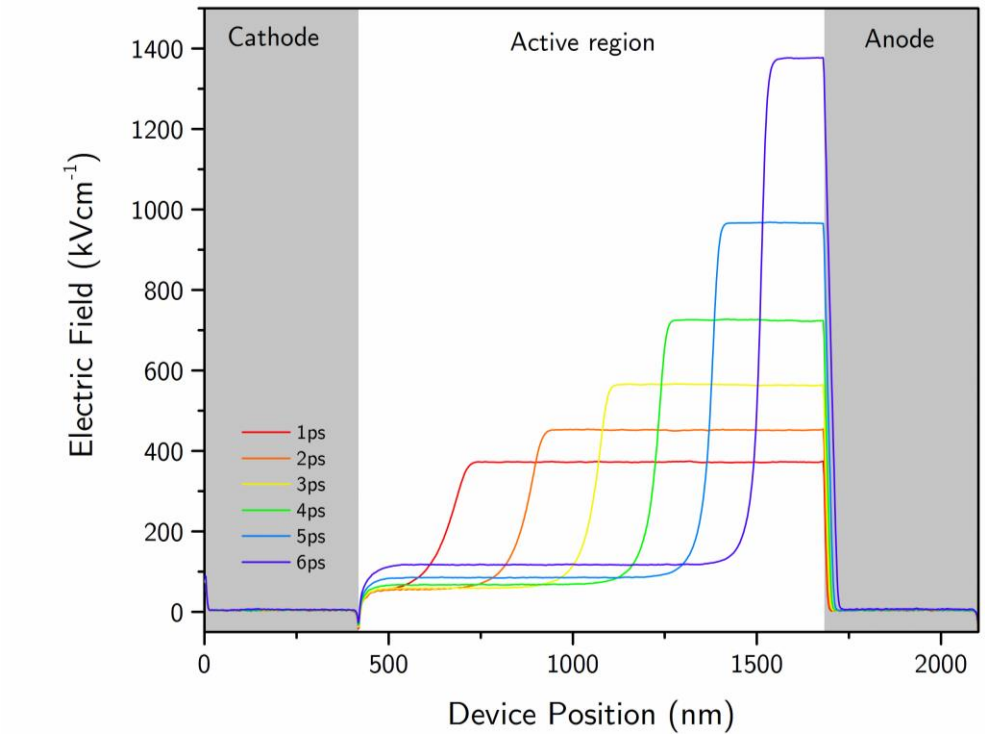

Figure 5.4 – Electric field as a function of device position for simulation times between 1 and 6ps.

larger effective mass and hence will be travelling slower when compared the 'lighter' electrons in the lower valleys in the low field regime.

The average electron velocity of electrons within each cell, as a function of device positon, for simulation times 1 to 6ps is presented in Figure 5.5. We see that at device positions preceding the accumulation layer we have an increased electron velocity. The average velocity of carriers within and in front of the accumulation layer stays around the same and is consistent with the saturation velocity ($v_s \sim 1.2 \times 10^7 \mathrm{cms}^{-1}$) found in the bulk results presented in Figure 5.1. Since the field prior to the domain is sub critical we see that at later simulation times, as the field increases the average electron velocity increases. This explains why the rate of charge accumulation increases closer to the anode in Figure 5.3. In order to confirm the physical processes behind the velocity profile the Γ valley occupancy is also investigated.

The Γ valley occupancy as a function of device positon for simulation times 1 to 6ps is presented in Figure 5.6. Electrons in the high field area of the active region, where the average electron velocity is around v_s, are shown to have mostly transferred out of the Γ valley. The Γ valley occupancy drops from 100% to between 10 and 25% depending on simulation time.

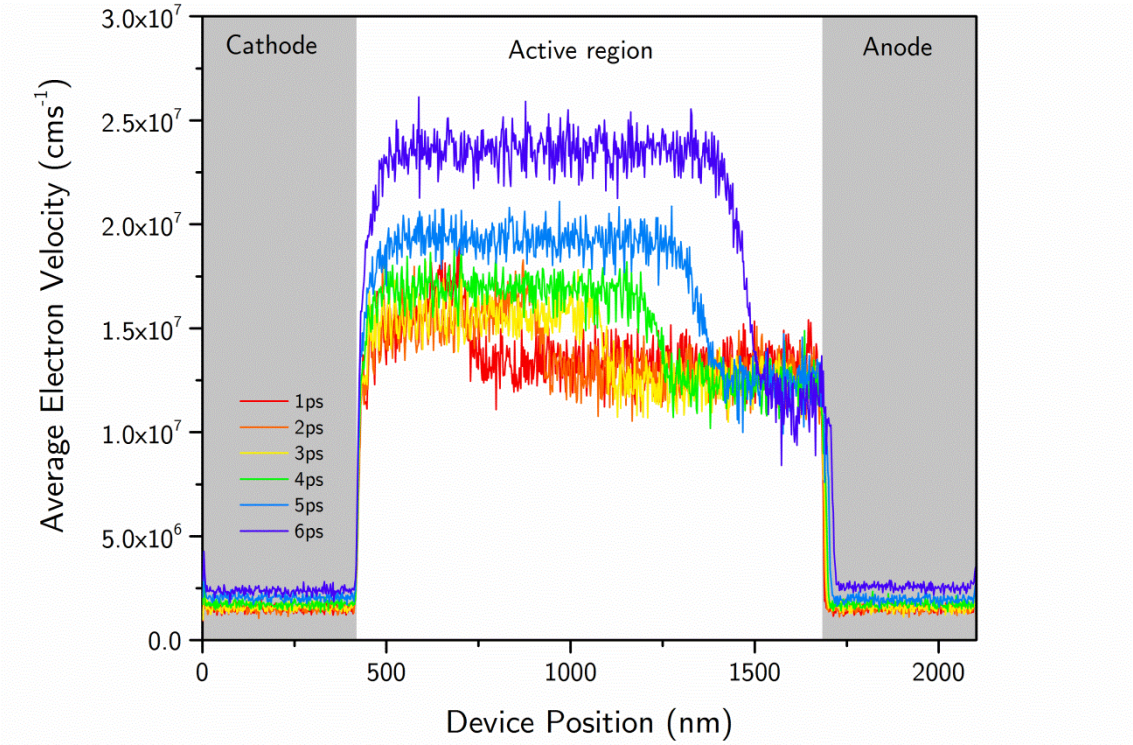

Figure 5.5 – Average electron velocity vs device position for simulation times between 1 and 6ps.

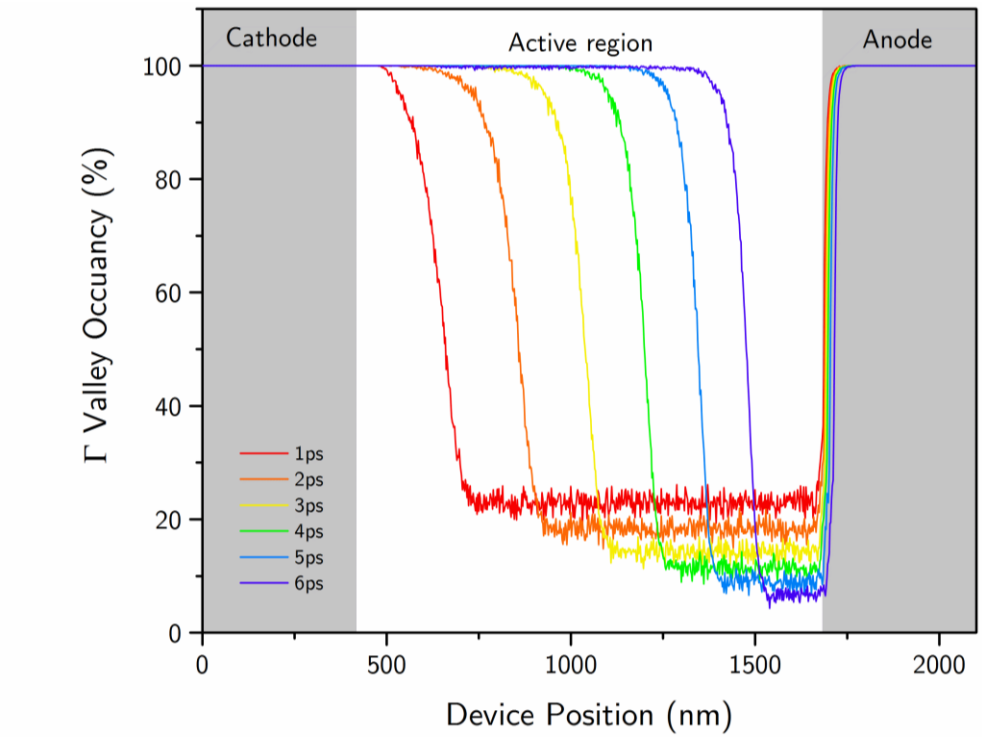

Figure 5.6 – Γ valley occupancy vs device position for simulation times between 1 and 6ps.

5.2.1. *Operating frequency*

Current oscillations are produced when Gunn domains or accumulation layers are present within a device. When charge is beginning to accumulate the current drops and then increases when the accumulation annihilates at the anode until charge begins to accumulate again [35]. We can estimate the frequency of the current oscillations by investigating the times at which charge begins to accumulate. In

Figure 5.7 we see that small amounts of charge has started to accumulate at x~800nm after 7.8ps and becomes significant by around 8.4ps. New accumulation layers are being formed at the same time as the established layers are making contact with the anode. Because the annihilation of the charge accumulation takes a measurable amount of time to occur any determination of transit time or operating frequency is approximate.

Charge density as a function of device position for various simulation times is presented with a reduced charge density scale in Figure 5.8 for a more accurate view of domain formation. It can be seen that a very small amount of charge is accumulating at 7.2ps, and a similar amount is accumulating after 13.4ps. An estimated transit time of 6.2ps is found and hence an operating frequency of f~161 GHz. We can also use the number of electrons leaving the anode as a function of simulation time to investigate operating frequency.

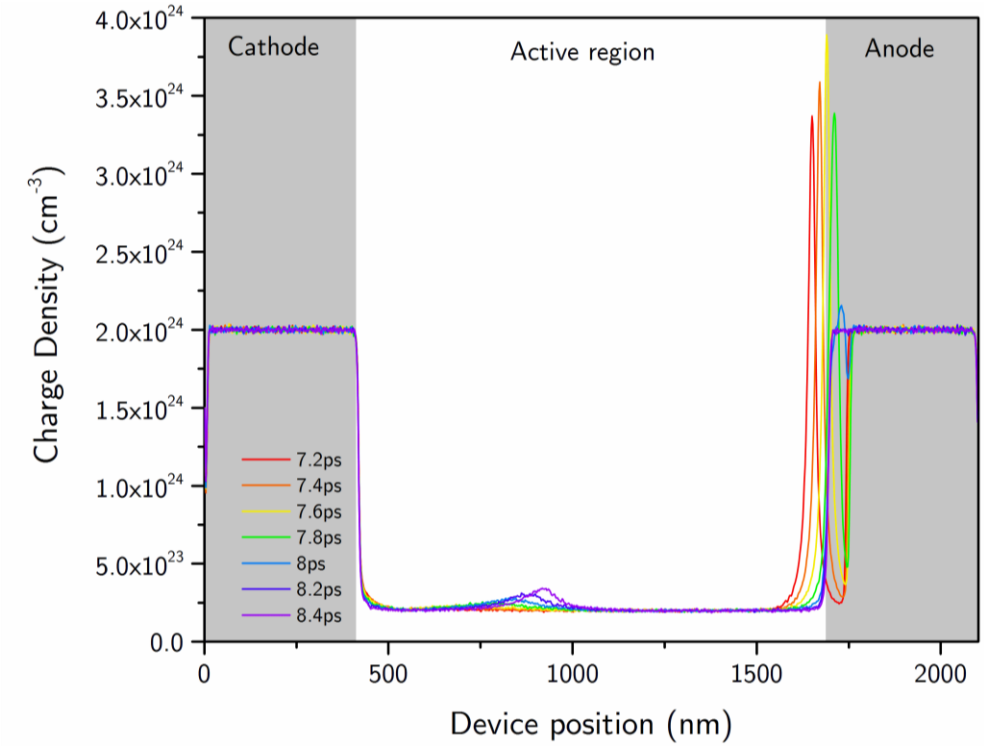

Figure 5.7 – Charge density as a function of device position for simulation times showing the interaction between the domain and the anode.

Several studies of a similar nature have assumed a contact area and have used this to scale the number of electrons leaving the contact into an actual current. We feel that for a 1-dimensional simulation this scaling is largely arbitrary and so present the number superparticles leaving the anode during each time step as a function of simulation time; this data can be found in Figure 5.9.

The shape of the current waveform is dependent on the width, transit time and growth time of the charge accumulation. A wider accumulation layer will take longer to fully annihilate at the anode meaning the spike in current will last for longer. While a reduction in transit time will increase the frequency oscillation by reducing the time between current spikes. A longer growth time will result in a less

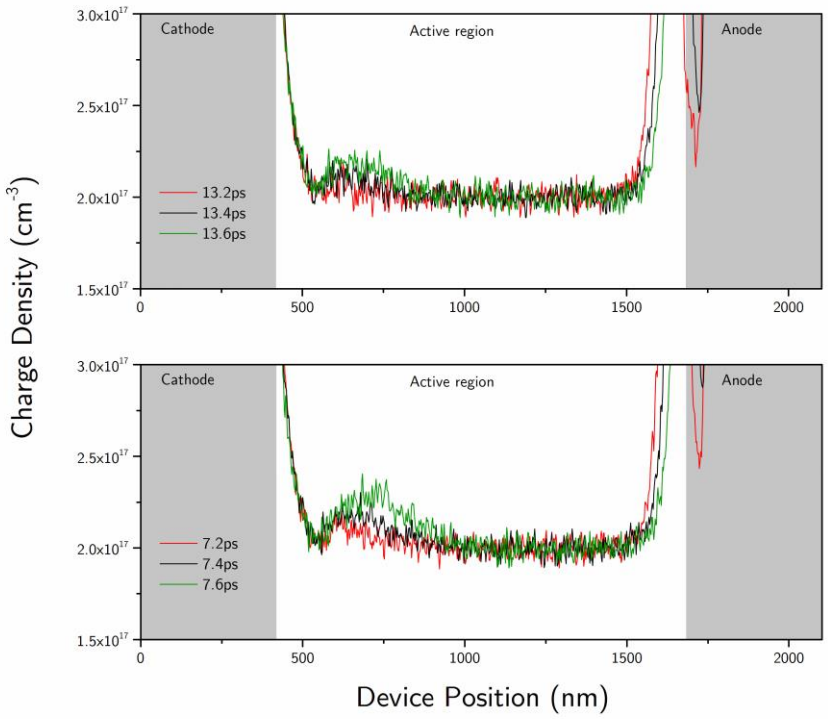

Figure 5.8 - Charge density as a function of device position for simulation times showing initial accumulation of charge.

sharp decrease in current after the spike. The accumulation layers are shown to be thin in Figure 5.3 and Figure 5.7 when they interact with the anode and so the sharp current spikes in Figure 5.9 are consistent with the background theory [38]. Accumulation layers are also shown to form as soon as the previous layer begins to annihalte. This short formation time is consistent with the sharp decrease in current following the peak. We see a clear increase in the number of electrons leaving the cathode at simulation times of around 7.2ps, 13.3ps, 19.4ps and 25.5ps. The transit time of the accumulation layer is around t~6.1ps which corresponds to an operating frequency of f~164 GHz.

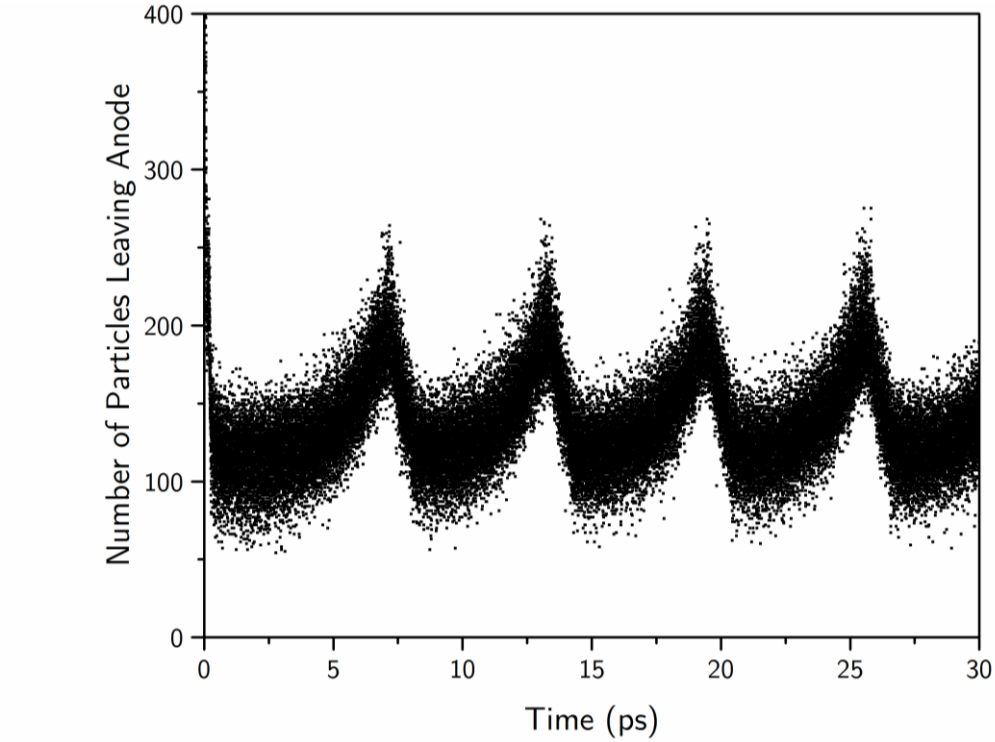

Figure 5.9 – The number of superparticles leaving the device at the anode every time step as a function of simulation time for a device operating in accumulation mode.

5.2.2. *Kroemer criteria not met*

In order to test the Kroemer criteria for our GaN device the doping density of the active region was reduced to $1\text{x}10^{16}\text{cm}^{-3}$. The n_0L product for the device becomes $1.26\text{x}10^{12}\text{cm}^{-2}$, around half that ($\left(\frac{3\epsilon v_s}{q|\mu_d|}\right) = 2.57\text{x}10^{12}\text{cm}^{-2}$) required for Gunn operation according to the Kroemer criterion. In the following sub-section charge densities and electric fields are presented as a function of device position for varying simulation times in addition to a figure showing the number of superparticles leaving the cathode. In Figure 5.10 accumulation layers are seen to form almost immediately. The charge density does grow as in the previous simulation but the rate of growth is much smaller. This is also noticeable in the electric field, presented

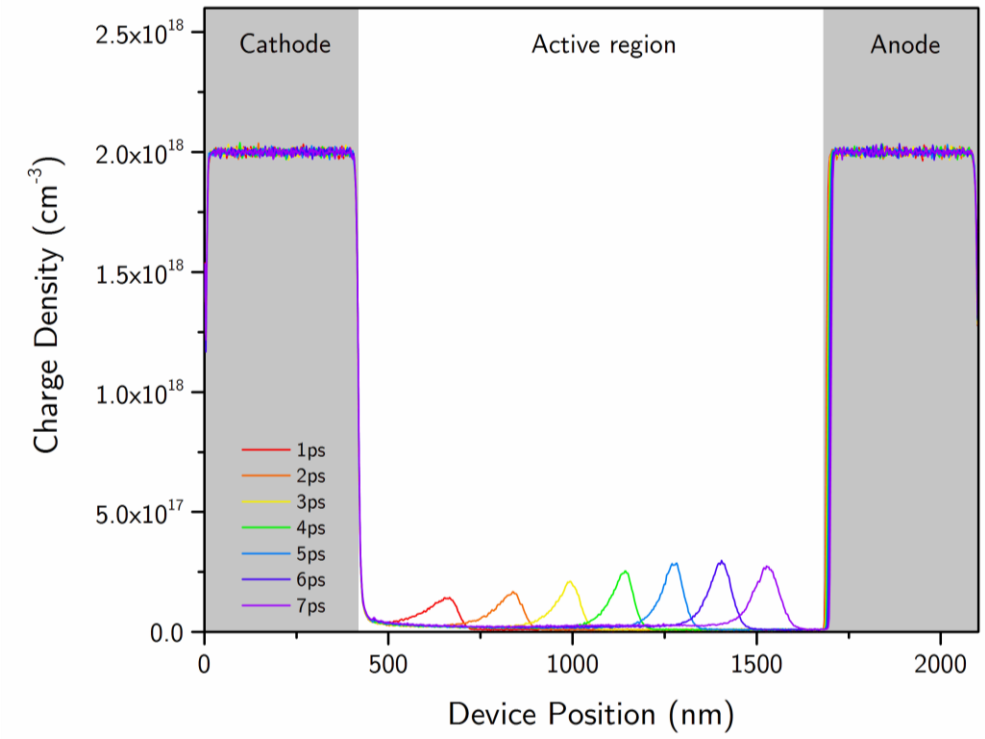

Figure 5.10 – Charge density as a function of device position for simulation times between 1 and 7ps when the Kroemer criteria is not met.

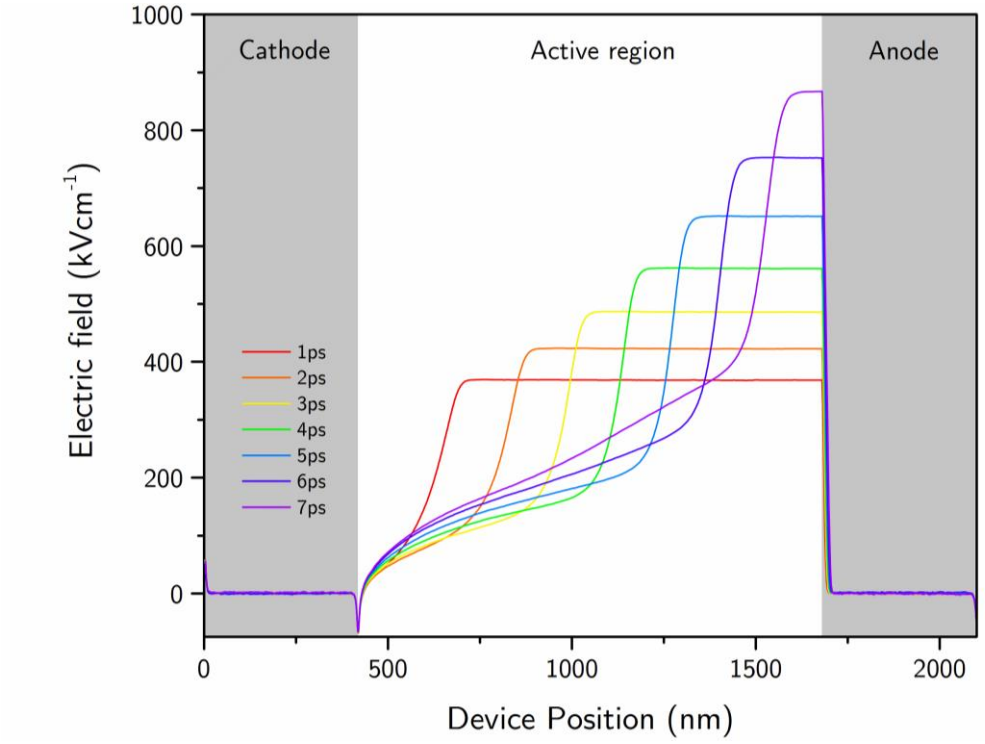

Figure 5.11 – Electric field as a function of device position for simulation times between 1 and 7ps when the Kroemer criteria is not met.

in Figure 5.11. The most important feature of this device is that after the initial charge accumulation has annihilated at the anode another does not form within the 30ps simulation time as is shown in Figure 5.12.

The critical field for GaN, taken from the bulk results presented in Figure 5.1 is around 150kV/cm. We can see from both figures Figure 5.11 and Figure 5.13 that the fields are high enough for Gunn effects to be produced. The lack of stable domain formation is due to the increased dielectric relaxation time τ_{dr} caused by a reduction in the doping of the active region. Since the dielectric relaxation time increases so does the domain formation time t_{gr}. When the domain formation time is sufficiently large it is more difficult for enough charge to accumulate to impose a field fluctuation above those already created by the normal movement of electrons within the system. At t=0 the electron distribution is largely consistent with the device doping profile with relatively minimal amounts of noise, in these conditions the initial charge accumulation is able to form.

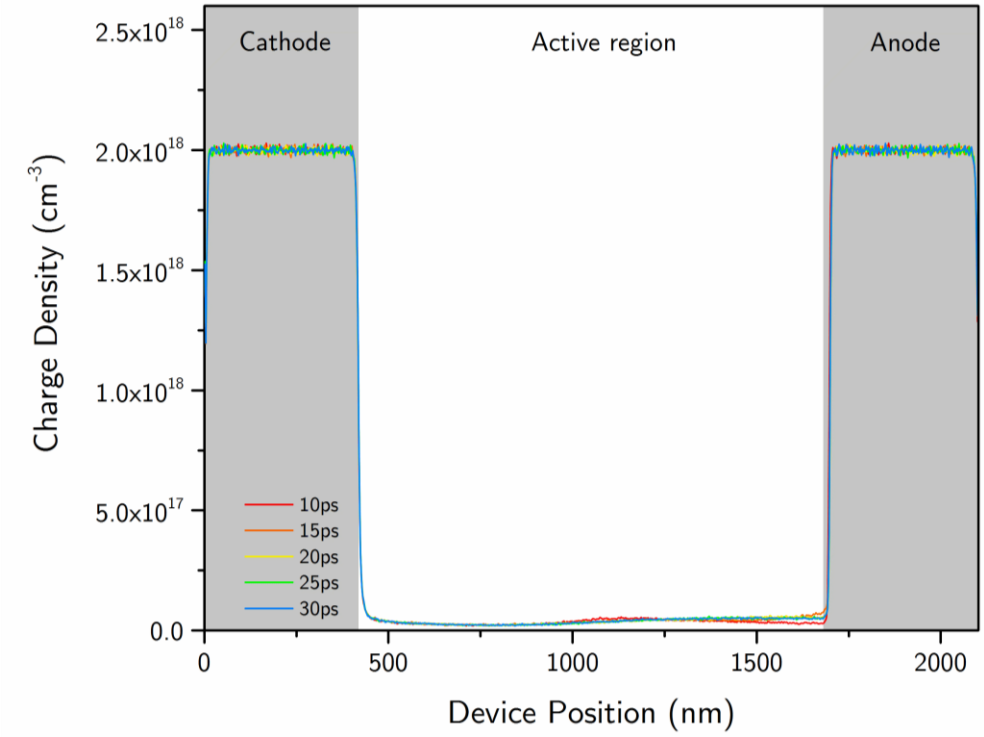

Figure 5.12 Charge density as a function of device position for simulation times between 10 and 30ps when the Kroemer criteria is not met.

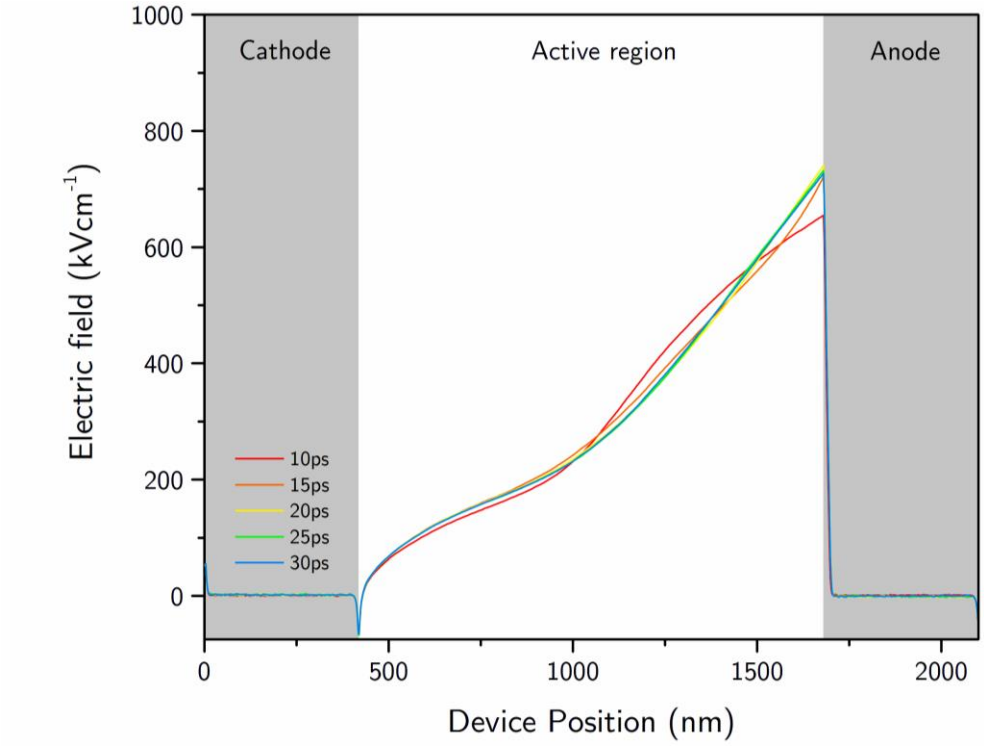

Figure 5.13 Electric field as a function of device position for simulation times between 10 and 30ps when the Kroemer criteria is not met.

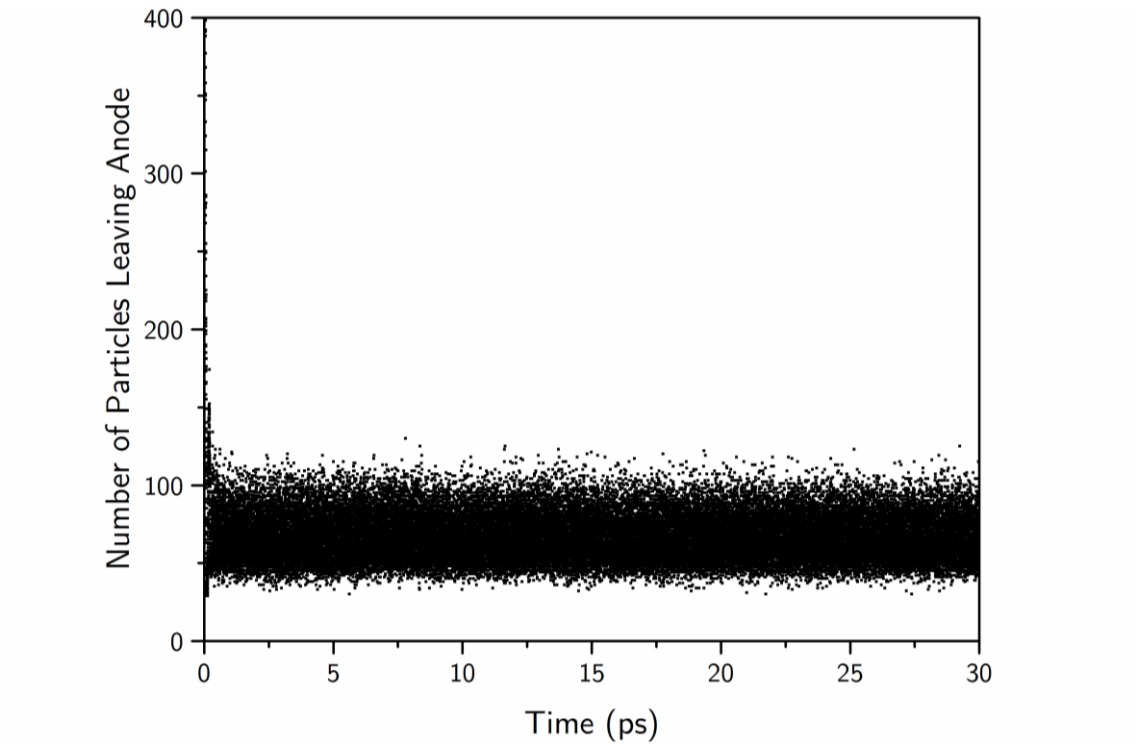

Figure 5.14 - The number of superparticles leaving the device at the anode every time step as a function of simulation time.

5.3. Results – Dipole mode

In the following section results are presented using the methods outlined in Chapter 2.3 for a GaN based Gunn device including a doping notch. A schematic of the notched device is presented in Figure 5.15. The doping notch, represented in orange in Figure 5.15, has a doping density of $8x10^{15}cm^{-3}$ and a length of 30nm.

In the dipole model the doping density of the active region is increased to $3.5x10^{17}cm^{-3}$ compared to $2x10^{17}cm^{-3}$ for the device operating in accumulation mode.

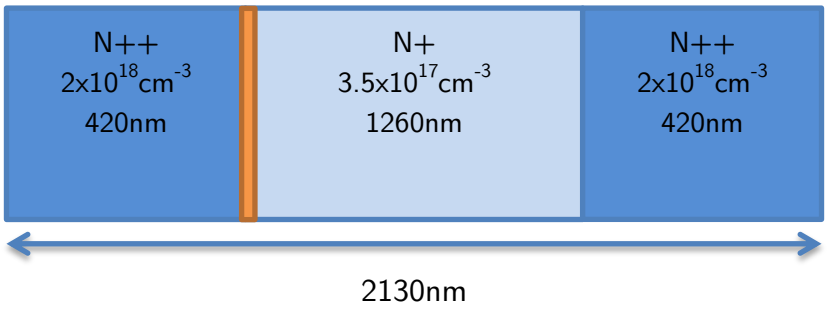

Figure 5.15 – Schematic of Gunn device being simulated. The doping density and length of each region is stated in the relevant region. A doping notch of length 30nm and doping density $0.8 \times 10^{16} cm^{-3}$ is shown in orange.

The applied potential is also reduced from 40V to 20V. Reducing the applied potential is necessary to ensure that the electric field within the active region at thermal equilibrium is lower than the saturation field. This ensures that electrons affected by the increase in electric field caused by the doping notch will have a reduced electron velocity. The device simulation parameters are summarised below in Table 5.4.

Charge density, electric field and average electron velocity are all presented as a function of device position for various simulation times. This data is used to analyse domain formation before investigating the current waveform and operating frequency of the device.

Parameter (units)	Device
Total length of device (nm)	2130
Length of anode and cathode (nm)	420
Length of active region (nm)	1260
Length of doping notch (nm)	30
Total number of grid spaces	852
Length of grid spacing – dx (nm)	2.5
Doping density at anode and cathode (cm^{-3})	$2x10^{18}$
Doping density in active region (cm^{-3})	$3.5x10^{17}$
Doping density of notch (cm^{-3})	$8x10^{15}$
Number of particles per cell	10,000
Time step – dt (ps)	$1x10^{-3}$
Lattice temperature (K)	300
Applied potential (V)	20
Number of time steps	30,000
$n_0 L$ (cm^{-2})	$4.41x10^{13}$

Table 5.4 - Simulation parameters used for 1D 3k GaN Gunn device operating in dipole mode.

Charge density as a function of device position for simulation times 2 to 7.2ps is presented in Figure 5.16. The characteristic dipole domain shape is clearly visible at around x=1000nm after 3.2ps. The regions of charge depletion and charge accumulation both become more prominent with time, behaviour consistent with the background theory [38]. Unlike the accumulation mode simulation there is a short

lag time before which a significant domain is produced. The dipole domain is shown to be much wider than the charge accumulation which is likely to have an effect on both the operating frequency and the shape of the current waveform, these effects will be analysed in detail in the next section.

The electric field as function of device position for simulation times 2 to 7.2ps is presented in Figure 5.17. For a device operating in dipole mode a sharp increase in field is expected around the charge accumulation. For a simulation time of 4ps this is shown to occur at around x=1020nm in Figure 5.16. The field peaks immediately after the region of charge accumulation, when the charge density reduces back to equilibrium as defined by the doping profile; after 4ps this occurs at x=1170nm (See Figure 5.16). The field begins to drop in the region of charge depletion, reaching an equilibrium point when the charge density returns to that described by the doping profile; this occurs at around x = 1300nm for a simulation time of 4ps. The behaviour of the electric field presented in Figure 5.17 is consistent with the charge density presented in Figure 5.16.

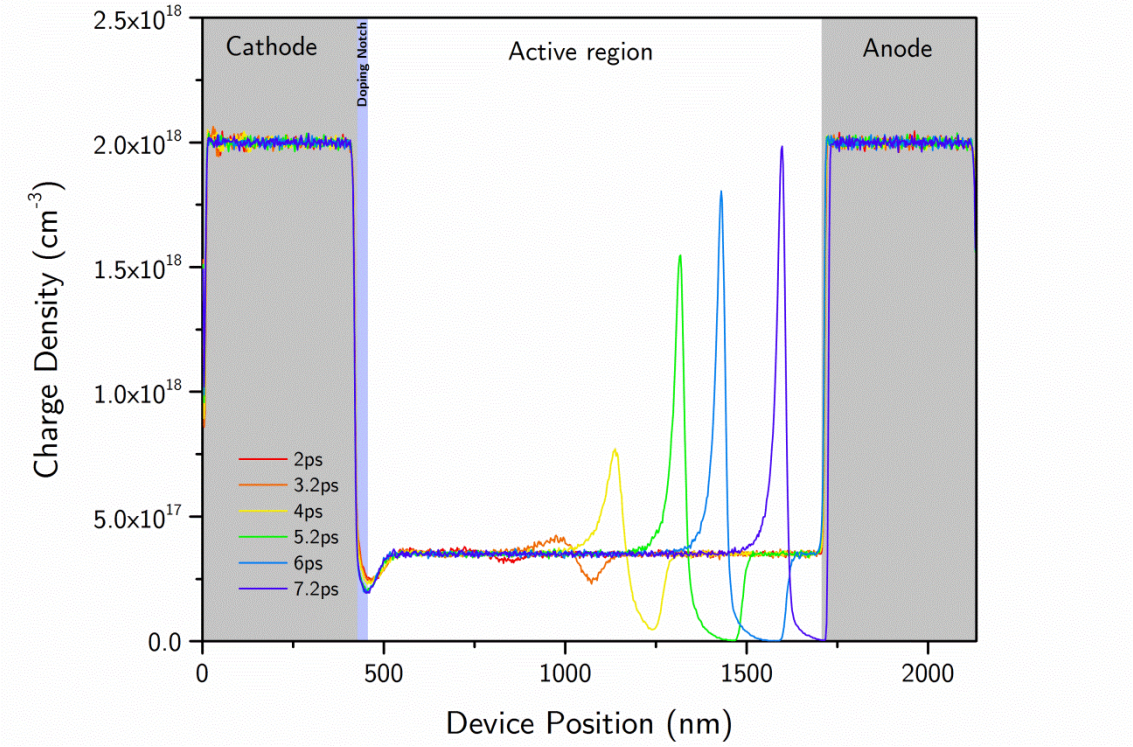

Figure 5.16 - Charge density as a function of device position for simulation times between 2 and 7.2ps.

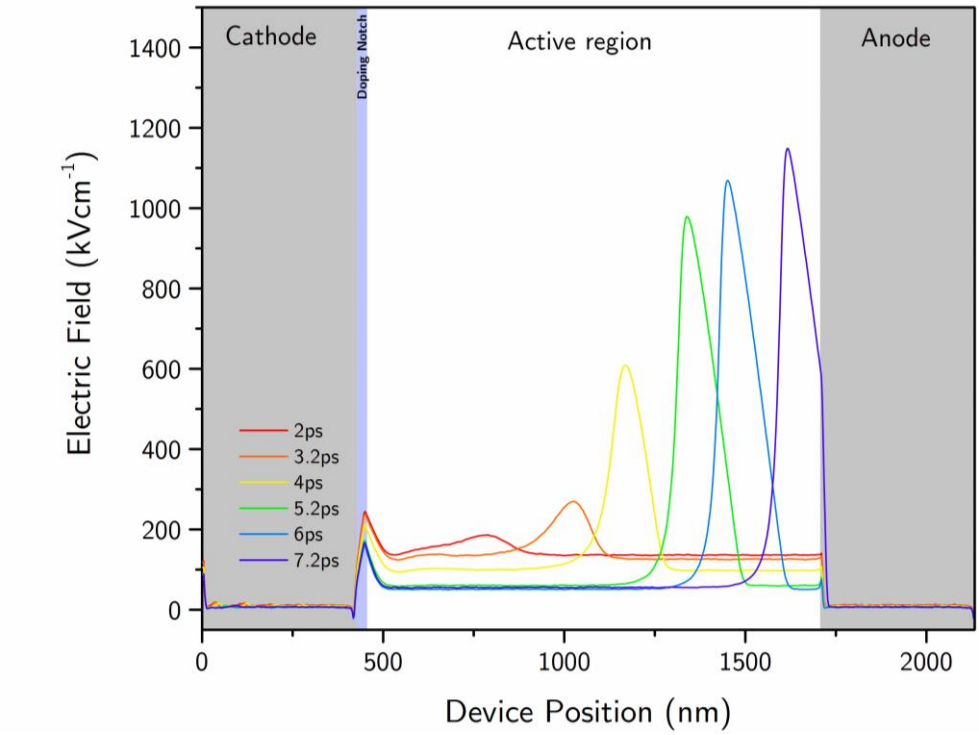

Figure 5.17 – Electric field as a function of device position for simulation times between 2 and 7.2ps.

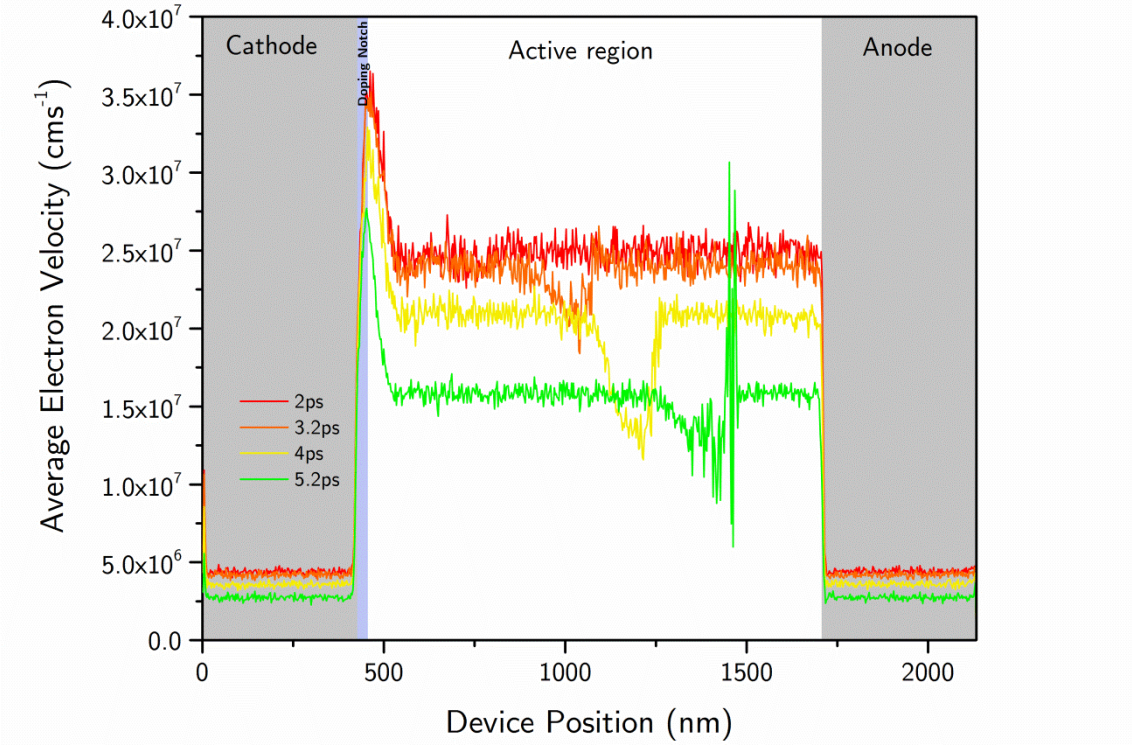

Figure 5.18 - Average electron velocity vs device position for simulation times between 2 and 5.2ps.

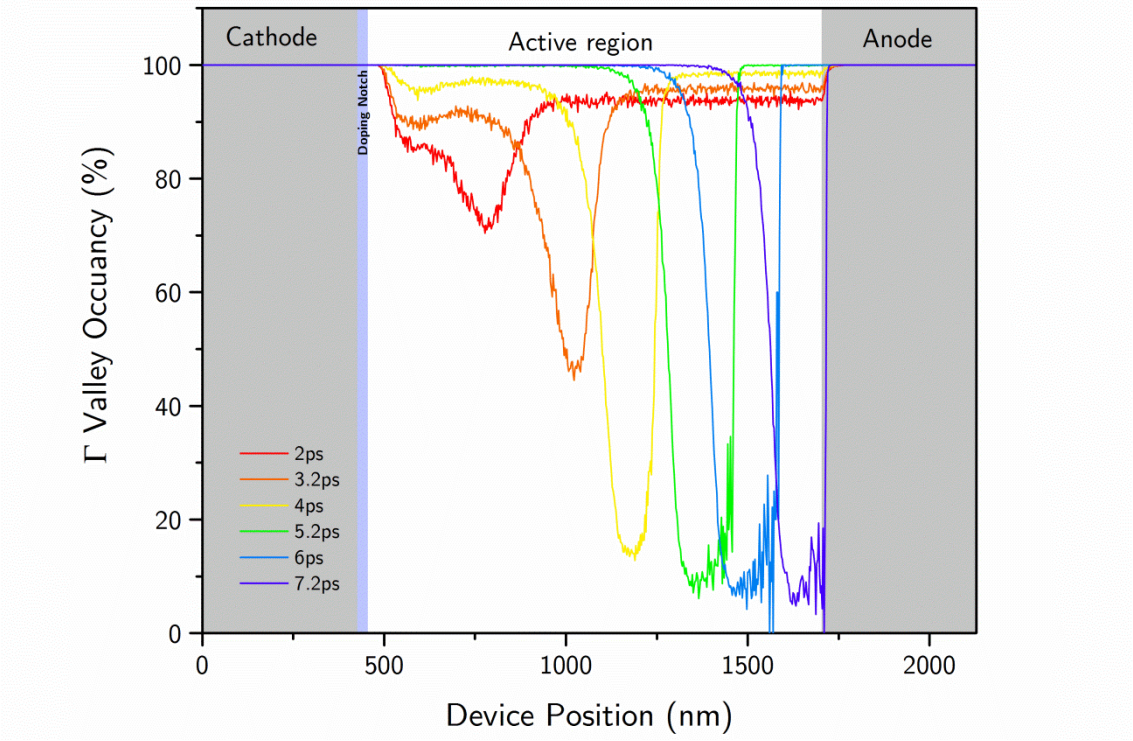

Figure 5.19 - Γ valley occupancy vs device position for simulation times between 2 and 7.2ps.

The average electron velocity per grid point as a function of device position for simulation times 2 to 5.2ps is presented in Figure 5.18. It is found that the average electron velocity increases around the doping notch. The increased velocity around the notch is fundamental to the formation of dipole domains and so it is useful to confirm that the doping notch is working as intended. It is also found that the average electron velocity dips around the areas of high field. After 5.2ps at around x~1500nm the velocity is seen to become rather noisy. The area of noise is consistent with the areas of charge depletion. The lack of charge in these areas means the average electron velocity is being calculated from a very small number of superparticles. With the charge depletion being so severe at late simulation times it is possible that average electron velocity is calculated according to the properties of only a few superparticles. The electron velocities for simulation times 6 and 7.2ps are dominated by noise around the dipole domain which is the main point of interest; and so these sets of results are omitted from Figure 5.18 to allow an easier analysis of the remaining data. For simulations after 4ps, when the domain is clearly established, it is shown that the dipole domain is moving at around the saturation velocity $(v_s \sim 1.2 \times 10^7 \mathrm{cms}^{-1})$. Interestingly, the dipole domain at simulations times prior to this are shown to travel slightly faster $(v \sim 1.9 \times 10^7 \mathrm{cms}^{-1})$. This can be explained by investigating the valley occupancy of the dipole domains at various simulation times.

The Γ valley occupancy as a function of device positon for simulation times 2 to 7.2ps is presented in Figure 5.19. Electrons in the high field area of the active region, within the dipole domain, are shown to have mostly transferred to the upper valleys. The number of electrons within the domain, occupying the upper valleys, is shown to increase with simulation time, until around 4ps at which point it is seen to reach a maximum. Electrons in the upper valleys have a higher effective mass and so as more electrons transfer to the upper valley it would be expected that the average velocity of electrons within the domain would reduce. This effect is shown to be responsible for the increased domain velocity found at simulation times before 4ps in Figure 5.18

5.3.1. *Operating frequency*

The number of electrons leaving the anode in a device operating in dipole mode should drop during domain formation and then increase when the dipole annihilates at the anode; much like a device operating in accumulation mode [35]. The transit time of the dipole will determine the operating frequency of the device while domain formation and annihilation times will determine the shape of the current waveform. These factors are likely to be different for a device operating in accumulation mode and a device operating in dipole mode. As such the shape of the current oscillation is likely to be different [38].

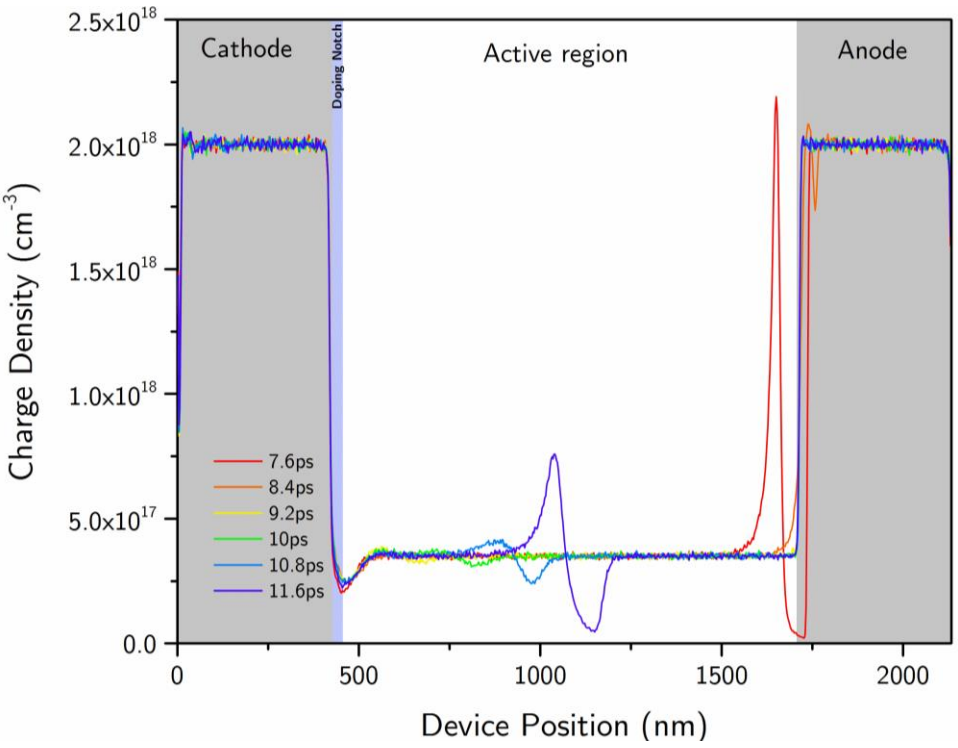

Figure 5.20 - Charge density as a function of device position for simulation times between 7.6ps and 11.6ps.

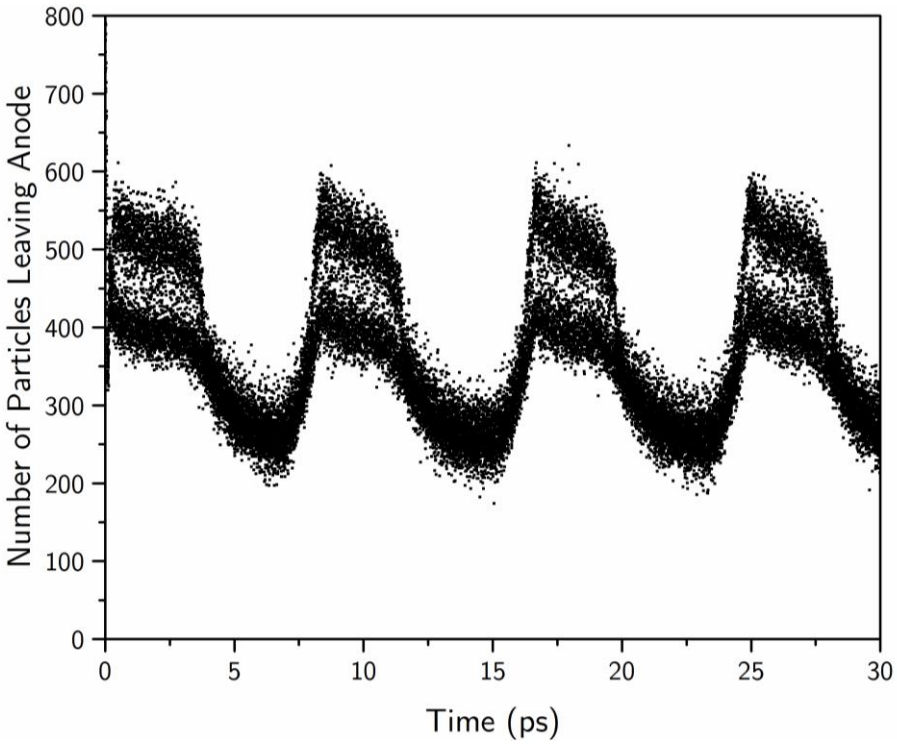

Figure 5.21 - The number of superparticles leaving the device at the anode every time step as a function of simulation time for a device operating in dipole mode.

The domain initially makes contact with the anode at around t=7.2ps (See Figure 5.16) at which point the current begins to increase. By around t=8.8ps the domain has fully annihilated which is the same time at which the number of electrons leaving the anode peaks. The current fluctuation is then found to slowly reduce, as a domain begins to grow, until around t= 10.8ps when the current sharply drops and a significant dipole domain is present. The reduction in current is caused by domain formation. The domain takes much longer to form compared to the device operating in accumulation mode and so the current waveform has a more prolonged peak rather than a sharp peak. There is an amount of noise noticeable around the highest part of the current waveform in Figure 5.21. An amount of noise is expected from a 1-dimensional model since the number of electrons leaving the anode is being calculated from a single cell. By simulating this same device in 2-dimensions and more realistic current waveform will likely be produced. The peak number of electrons leaving the anode occurs at 8.3ps, 16.7ps and 25.1ps giving an average transit time of around 8.4ps and a corresponding operating frequency of f~119 GHz.

5.4. Summary

In this chapter N++ - N+ - N++ vertical Gunn diodes have been explored. The mechanisms surrounding the formation of charge accumulations have been explored. A GaN Gunn diode was simulated and shown to operate in accumulation mode. The physical principles surrounding how the device functioned was explored and was

shown to be consistent with the background literature. The results presented here have significantly less noise than those presented in a comparable Monte Carlo study undertaken by Macpherson [44], showcasing the importance of a fine mesh and a large number of superparticles. The Kroemer criterion has been checked against the simulation. It was found that when the Kroemer criterion is not met in our model charge accumulations are not consistently formed. The operating frequency of the device was found to be 164 GHz and the shape of the current waveform was presented.

The device simulated by Macpherson had an active region of the same length (1260nm) as the model presented here and had an operating frequency of around 300 GHz [44]. As mentioned previously the valley separation in the study by Macpherson is much larger than the one used here. The larger valley separation will result in a larger critical field, peak velocity and saturation velocity; meaning the charge accumulation will travel across the active region with a higher velocity leading to an over estimation of the operating frequency. The investigation by Momox also finds a larger operating frequency than what is reported here at between 300-700 GHz even with a larger active region length of 2000nm. The actual GaN device created by Pavlidis [6] had a much lower operating frequency compared with these models as well at between 65-95 GHz with an active region of around 3000nm.

In the final section of this chapter the mechanisms surrounding the formation of dipole domains in 1D vertical devices were explored. For the first time a GaN Gunn device was simulated that was shown to operate in dipole domain mode. The physical principles which governed device function were explored and shown to be consistent with the background literature. The operating frequency of the device was estimated to be 119 GHz and the shape of the current waveform was investigated. The shape of the waveform was found to be different to that of the device operating in accumulation mode due to the difference in domain growth and domain annihilation times.

The operating frequency of a device operating in accumulation mode is restricted by the length of the active region and the transit time of the charge accumulation and hence the saturation velocity of the material being used in the active region [84]. It has been shown that for a device operating in dipole mode that the domain travels at velocities higher than the saturation velocity under certain conditions. This provides the opportunity for the development of a device which can operate at a higher frequency than that dictated by the saturation velocity and active region length [85].

Chapter 6. 2-Dimensional Device Development

Many GaN based electronic devices have multi-dimensional effects which cannot be accurately modelled using the 1-dimensionanl device model presented in the previous chapters. High Electron Mobility Transistors (HEMT's) can be created without modulation doping in AlGaN/GaN heterostructures due to spontaneous and piezoelectric polarisation at the interface producing a 2-Dimensional Electron Gas (2DEG) [4]. High power GaN based electronic such as Heterojunction Field-Effect Transistors (HFETs) have a device geometry whereby the contacts and gate are placed on top of an active layer where a 2DEG is formed [86]. In each of these circumstances a 1-dimensional model would not be capable of producing a realistic representation of actual device function. It would be possible however to accurately model each device using two spatial dimensions. The results presented in this section have been collected using the model described in Chapter 2.4. As the first step in the development process a 2-dimensional vertical GaN Gunn diode with the same structure as that presented in Chapter 5.2 has been simulated. The physical

principles presented in this chapter are largely the same as in Chapter 5. These results are presented as a proof of concept that our in-house developed Monte Carlo model is able to accurately simulate 2-dimensional devices. The following model simulates electrons in 2 spatial directions; electrons are not part of a 2DEG.

6.1. Results

The data presented in the following chapter follows the same pattern as in chapter 5. Charge density, electric field, average electron velocity and valley occupancy profiles are presented in 2-dimensions and compared to the 1-dimensional model. The device structure is presented in the same format as the contour plots in Figure 6.1. The material specific parameters for GaN are the same as those used in the previous models. The device specific parameters are the same in the x-direction as those used in the 1-dimensional device model operating in accumulation mode. These parameters are presented in Table 6.1 for convenience along with parameters specific to the y-direction.

The 2-dimensional model is significantly more computationally expensive compared with the 1-dimensional model. The most significant factor affecting simulation time is the more complex Poisson solver routine. The electric field and potential profiles are now calculated according to the 4 adjacent grid spacing's, instead of 2 as in the 1d model, an additional set of boundary conditions must be accounted for in the y-

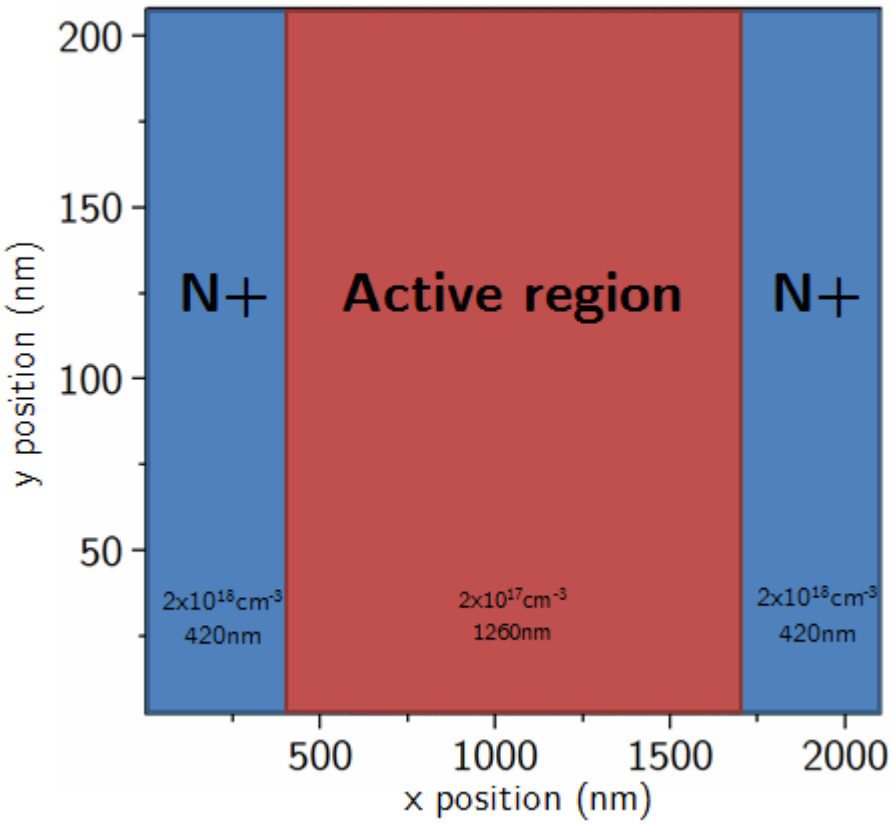

Figure 6.1 – Schematic of 2-dimensional Gunn device operating in accumulation mode

direction and the number of grid points is significantly increased (100000 in the 2d model compared with 1000 in the 1d model). In an attempt to keep simulation times reasonable the number of particles per cell is reduced from 10,000 in the 1-dimensional simulation to 40 in the 2-dimensional simulation. Despite the significant reduction in the number of particles per cell it is estimated that in thermal equilibrium there are 1.84×10^6 superparticles present in the 2-dimensional device model.

Parameter (units)	Device
Total length of device (nm)	2100
Length of anode and cathode (nm)	420
Length of active region (nm)	1260
Number of grid spaces in the x-direction	1000
Length of grid spacing - dx (nm)	2.1
Total width of device in y-direction (nm)	210
Number of grid spaces in the y-direction	100
Length of grid spacing – dy (nm)	2.1
Doping density at anode and cathode (cm^{-3})	$2x10^{18}$
Doping density in active region (cm^{-3})	$2x10^{17}$
Number of particles per cell	10,000
Time step – dt (ps)	$5x10^{-4}$
Lattice temperature (K)	300
Applied potential (V)	40
Number of time steps	60,000
$n_0 L$ (cm^{-2})	$2.52x10^{13}$

Table 6.1 – Simulation parameters for 2-dimensional GaN Gunn device model.

The charge density profiles for simulation times 1ps to 6ps are presented as a contour plots in Figure 6.2. As expected a small accumulation layer is seen to form around the cathode and grows in size as it propagates towards the anode. The

accumulation of charge in the 1-dimensional model is found at around 680nm (1ps), 900nm (2ps), 1050nm (3ps), 1230nm (4ps) 1375nm (5ps) and 1510nm (6ps). The charge accumulations are found in the same areas of the device at the same simulation times in the 2-dimensional model. The amount of charge present in the accumulation layers varies in the 2-dimensional model with y-position. For example, after 2ps the charge density within the accumulation layer at x = 900.9nm, ranges from $2.5x10^{17}cm^{-3}$ to $5.5x10^{17}cm^{-3}$; compared to a peak charge density of around $3.8x10^{17}cm^{-3}$ in the 1-dimensional model. The top and bottom boundaries of the device are electrically neutral so the charge density profile should be reasonably uniform in the y-direction. Charge density as a function of y position is presented in Figure 6.3 for an x position of 900.9nm.

The results presented in Figure 6.3 indicate that the variation of charge density with y position is statistical noise rather than a physical effect. A small amount of noise is to be expected, however it is thought that the relatively low number of particles per mesh spacing is exacerbating the effect. Despite the noticeable level of noise in the y-direction the charge density profile of the device as a whole is consistent with the 1-dimensional model.

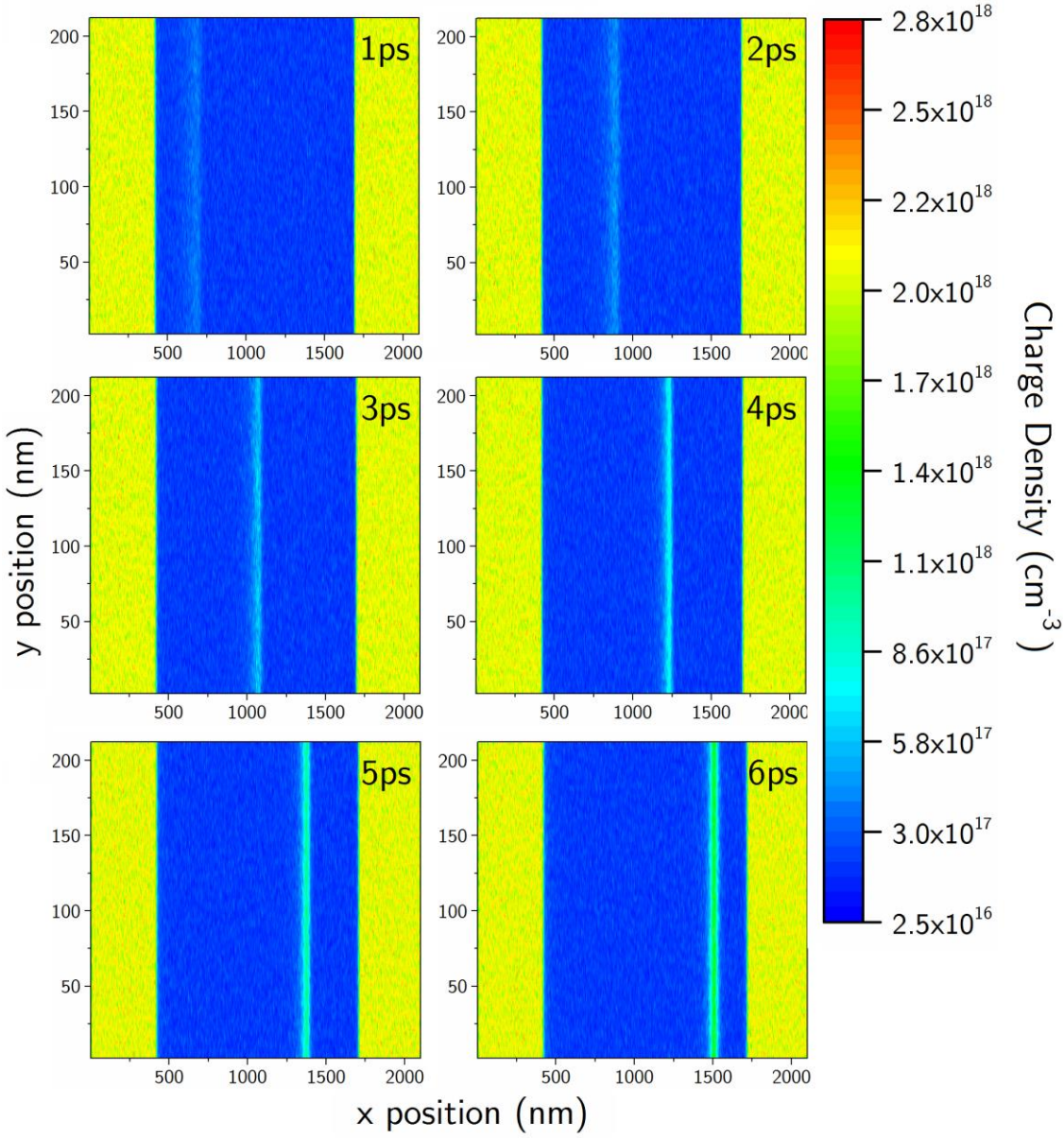

Figure 6.2 – Charge density (cm^{-3}) as a function of device position in the x and y directions for simulation times 1-6ps.

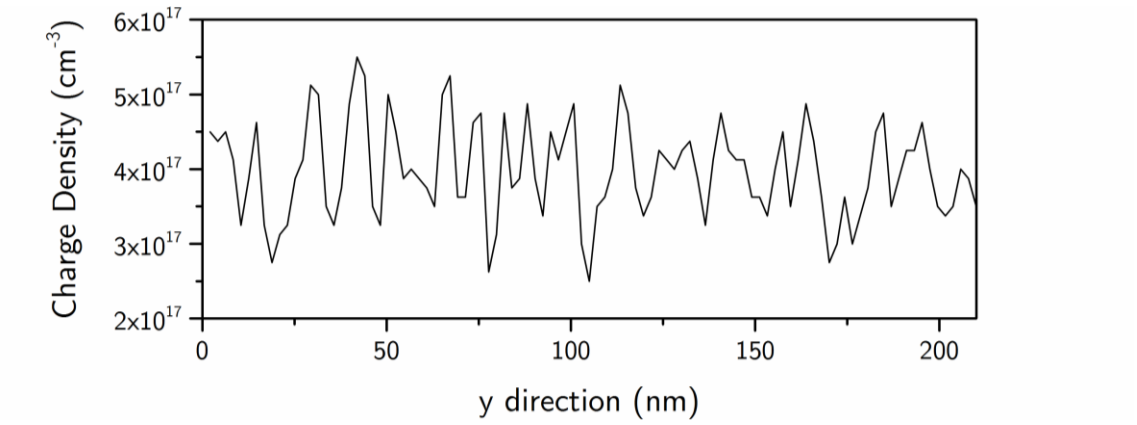

Figure 6.3 – Charge Density as a function of y direction for the mesh spacing x = 900.9

The electric field profiles for simulation times 1 to 6ps are presented in Figure 6.4. The field is clearly separated within the active region resulting in a high field region at positions in front of the accumulation layer and a low field region at positions before the layer. The electric field is shown to be constant with y position which further rules out any physical effects manipulating electrons in the y-direction. The position where the field profile splits is consistent with both the charge density profile presented in Figure 6.2 and the results presented for the 1-dimensional model in Figure 5.4. The electric field profile provides confidence in the function of the 2-dimensional Poisson solver and reinforces the idea that any variation in electron characteristics in the y-direction is simply statistical noise.

The average electron velocity within each cell, as a function of device positon, for simulation times 1 to 6ps is presented in Figure 6.5. The average velocity is highest in the areas preceding the accumulation layer and grows within this region with simulation time; the same behaviour observed in the 1-dimensional model.

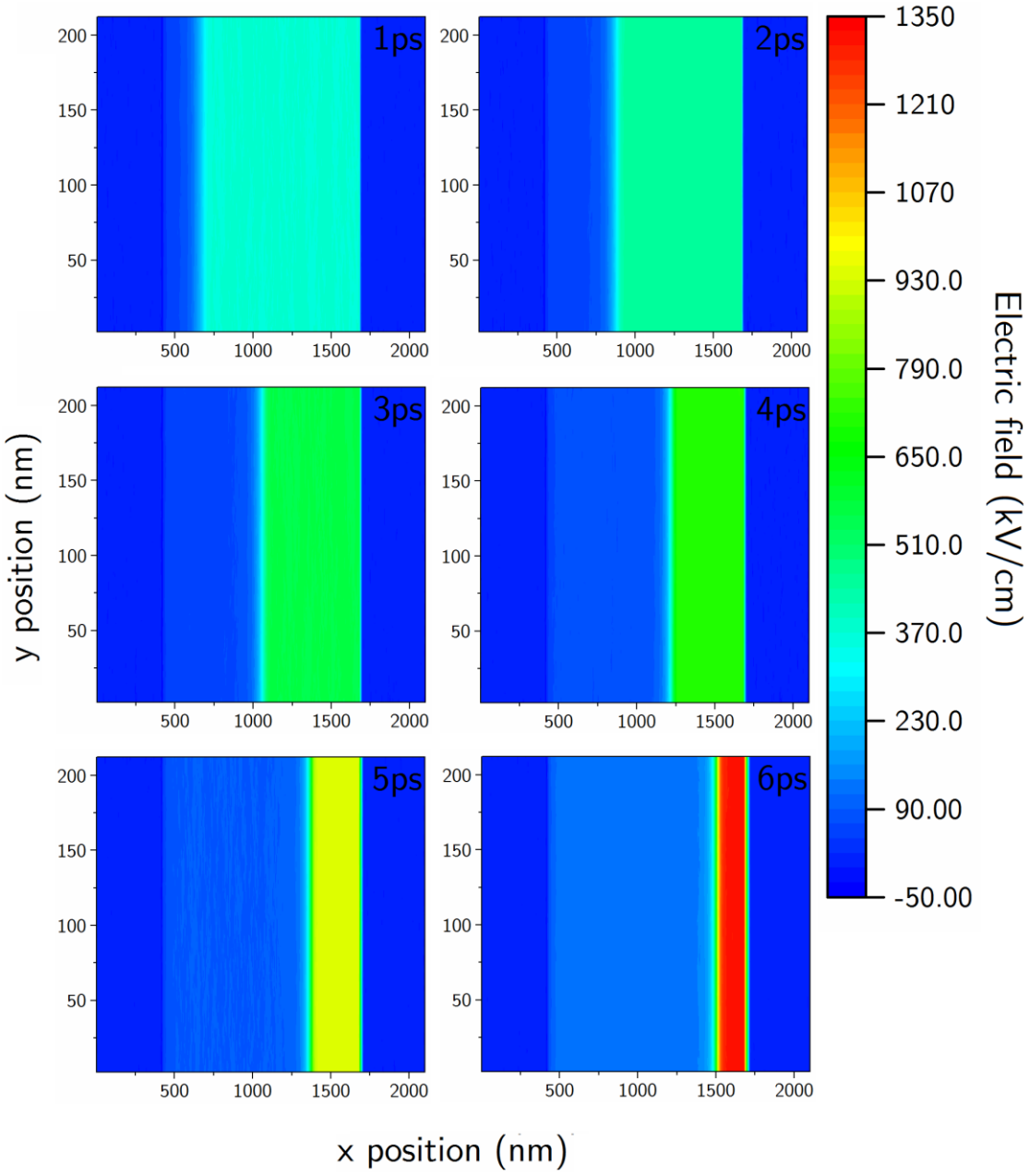

Figure 6.4 – Electric field (kV/cm) as a function of device position in the x and y directions for simulation times 1-6ps.

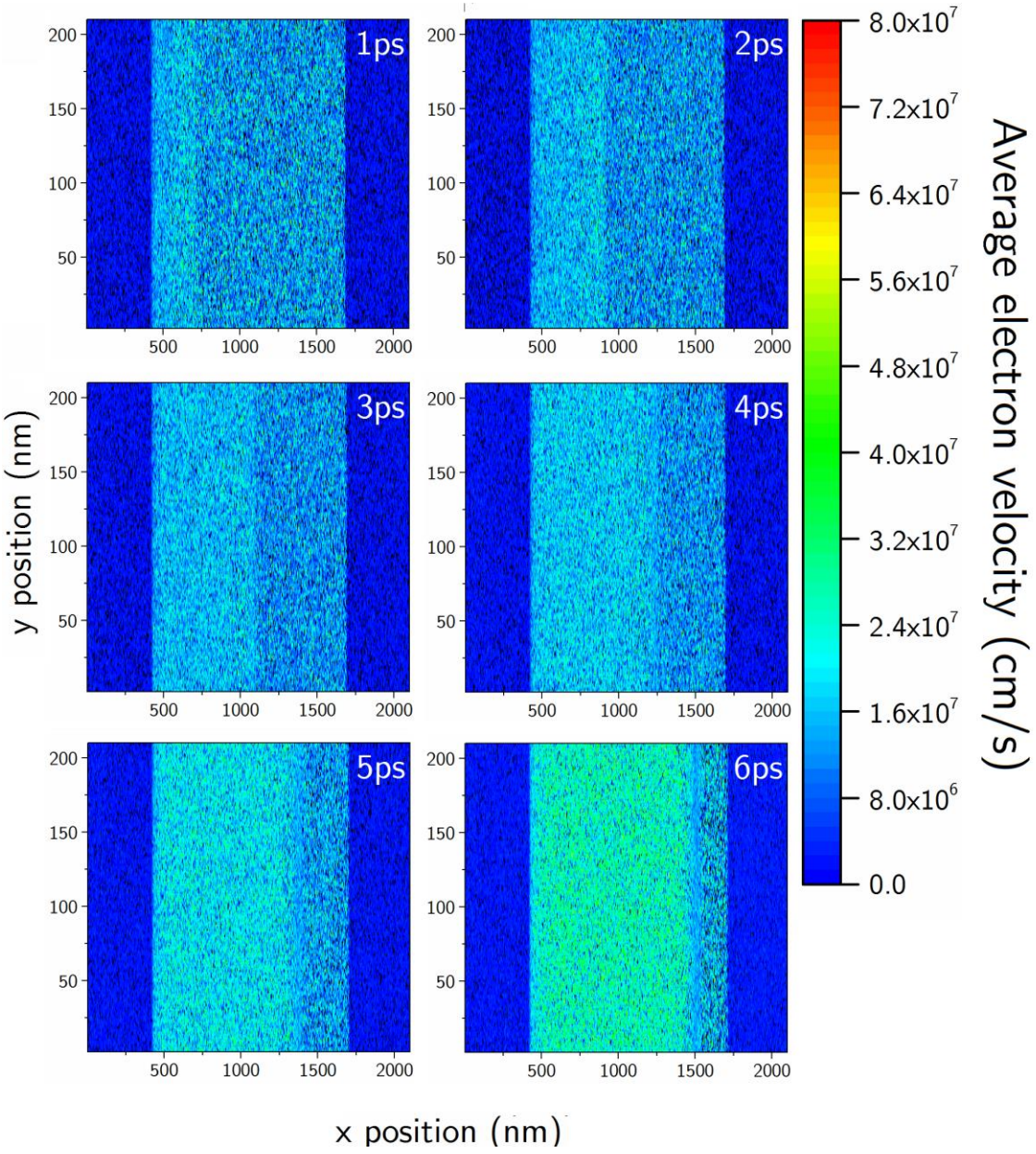

Figure 6.5 – Average electron velocity in the x-direction (cm/s) as a function of device position in the x and y directions for simulation times 1-6ps.

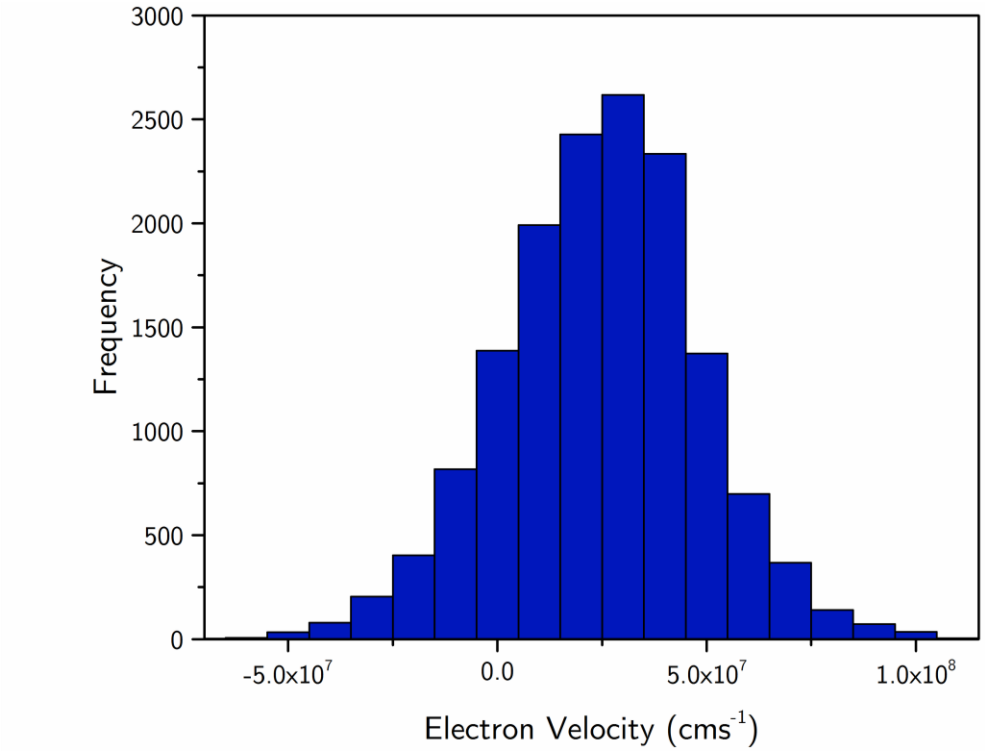

Figure 6.6 – Histogram showing the electron velocity in the direction of the applied field (x-direction) distribution of 15,000 particles in a bulk GaN simulation at 100kV/cm.

The average velocity of electrons within or in front of the accumulation layer stays around the same and is consistent with the 1-dimensional model and the saturation velocity of the bulk model ($v_s \sim 1.2 \times 10^7 cms^{-1}$). As was seen in the depletion region of the devices simulated in Chapter 5 the average electron velocity is very sensitive to the number of superparticles being simulated. Electron velocity is affected by many transient processes and has a widespread distribution even for individual applied fields in steady state. The velocity distribution of 15,000 particles in a bulk GaN simulation is shown in Figure 6.6 as an example. With such a wide velocity distribution some statistical noise within physical space is expected. It also

seems likely however that the levels noise seen in Figure 6.5 could be reduced by simulating a larger number of superparticles.

Finally, the Γ valley occupancy profile is presented in Figure 6.7 for simulation times between 1 and 6ps. In areas of low field and high velocity it can be seen that the majority of electrons occupy the lowest conduction band valley. Electrons which make up the accumulation layer and those occupying the area in front of the accumulation, where the electric field is high and the average velocity is low, mostly occupy the upper valleys. The valley occupancy profile is consistent with what would be expected from the electric field profile and can be used to explain the velocity profile presented in Figure 6.5. In areas where most electrons occupy the upper valleys we find that the average electron velocity is around the saturation velocity whereas electrons shown to occupy the lower valleys are found the have a higher velocity. The proportion of superparticles occupying the upper valleys in the high field areas increases with simulation times, consistent with the 1-dimensional model.

6.2. Summary

The behaviour of carriers in the 2-dimensional model is shown to be consistent with the behaviour of carriers in the equivalent 1-dimensional model. With correct carrier behaviour being simulated the model is ready to be taken into the next stages of development. Various issues associated with the 2-dimensional model have also been

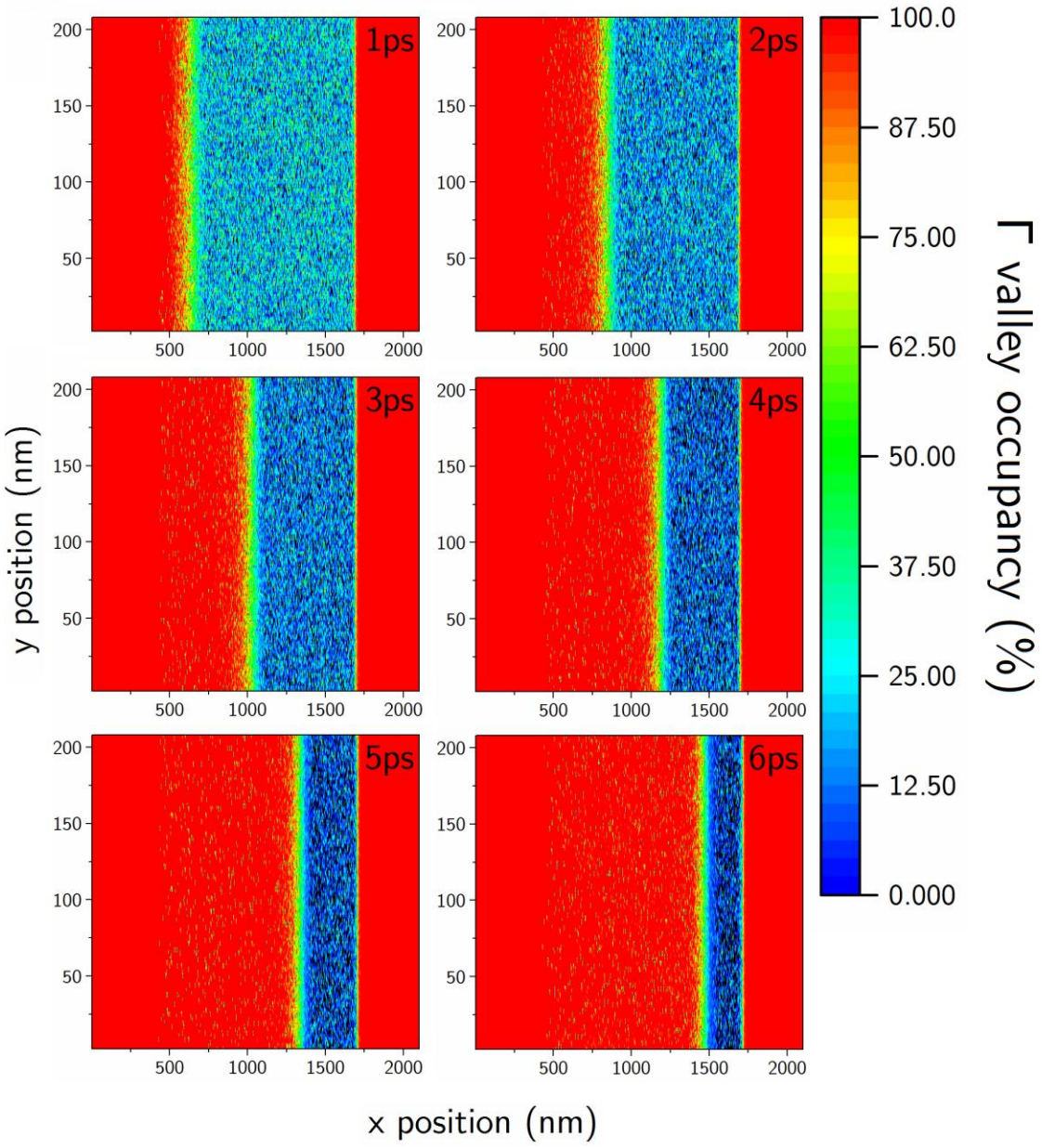

Figure 6.7 – Average Γ valley occupancy per mesh spacing (%) as a function of device position in the x and y directions for simulation times 1-6ps.

highlighted from this exercise. The most important issue is the requirement to reduce the number of particles being simulated per cell compared with the 1-dimensional model. A reduction in the number of simulated particles per cell is shown to have a slight detrimental effect on the precision of the model. A more detailed description regarding the performance of this model and the further developments envisaged to tackle performance issues will be presented in the final chapter of this thesis.

Chapter 7. Conclusions and Future Work

In this thesis the effects of a hot phonon distribution on electron transport in bulk $In_{0.53}Ga_{0.47}As$ have been explored and Gunn diodes have been simulated. The evolution of the phonon distribution in $In_{0.53}Ga_{0.47}As$ was described and shown to be consistent with data published for GaAs. It was shown that the dominant hot phonon effects in $In_{0.53}Ga_{0.47}As$ at room temperature are diffusive heating and phonon reabsorption. A noticeable phonon drag effect was not found to be present.

Results have been presented for a recreation of a Gunn device simulated by Tully in 1983 [1]. It has been shown that if a constant potential is applied across the device it will operate with a stationary anode domain. A time dependent potential is required for the device to function in accumulation mode. The device is shown to operate with a considerable 'dead zone' consistent with the original research. The results presented here are shown to be consistent with those presented by Tully [1] when accounting for the uncertainty surrounding the parameter set used in the original research. The average electron velocity results presented in this thesis show

considerably less noise than in the original publication which demonstrates the increased precision which can be achieved in Monte Carlo simulations by using a finer mesh and more superparticles per cell.

GaN Gunn diodes were simulated in one spatial dimension. A device was simulated operating in accumulation mode with an operating frequency of 164 GHz. The Kroemer criterion was also proven for a device of this design. For the first time a GaN Gunn diode was simulated that was shown to be operating in dipole domain mode. The device had an operating frequency of 119 GHz. The shapes of the two waveforms have been compared. A proof of concept for a 2-dimensional device simulator was also presented. The device model was found to be operating as expected producing results consistent with the equivalent 1-dimensional model. The exercise highlighted several areas for potential future development.

There is a number of interesting development routes which could be followed to expand the models presented in this thesis for further investigations. The three main routes are, combining the device model with the hot phonon model to simulate hot phonon effects in semiconductor devices, expanding the 2-dimensional device so that more complex devices can be modelled and a computational optimisation of each of these models. By combining the hot phonon model with the device model the effects of a non-equilibrium phonon distribution on transport within electronic devices can be investigated directly. To successfully utilise a model of this design a

large amount of computing power would be required. A powerful computational resource has recently become available at the University of Hull in the form of Viper. Viper is the University of Hull's new High Performance Computer (HPC); it is the highest rated HPC within the university sector in the north of the UK. The HPC contains 180 compute nodes each with 2x14 core processors which is a vast improvement compared with the 64 cores available at the time this research was conducted.

The 2-dimensional model could be expanded so that more complex devices can be modelled. The initial first step would be to move away from simulating vertical devices and to model more traditional planar devices with the source and drain positioned on top of the active region. This could be expanded further by attaching a gate to simulate a MOSFET. Finally, the model could be used to simulate 2 Dimensional Electron Gases (2DEGs) which would enable the simulation of devices like HEMT's which utilise the high mobility of 2DEGs. A 2DEG scattering routine is currently under development by a fellow PhD student.

For either of these developments to be successful it is vital that a computational optimisation is undertaken in an attempt to manage the significant increase in computational complexity. As mentioned previously the introduction of the Viper HPC will enable the implementation of the computationally demanding model extensions. In addition to using the Viper HPC for the more computationally

demanding projects it would be possible to re-write the models using Nvidia's CUDA platform for use on Graphics Processing Units (GPUs). In this way the model could be run across thousands of cores without the need of optical interconnects which would reduce performance.

References

[1] J. W. Tully, "Monte Carlo Simulation of a Millimeter-Wave Gunn-Effct Relaxation Oscillator," *IEEE Trans. Electron Devices*, vol. 30, no. 6, pp. 566–571, 1983.

[2] T. J. Flack, B. N. Pushpakaran, and S. B. Bayne, "GaN Technology for Power Electronic Applications: A Review," *J. Electron. Mater.*, vol. 45, no. 6, pp. 2673–2682, 2016.

[3] A. Bindra, "Wide-Bandgap-Based Power Devices," *IEEE Power Electron. Mag.*, no. March, pp. 42–47, 2015.

[4] O. Ambacher, J. Smart, J. R. Shealy, N. G. Weimann, K. Chu, M. Murphy, W. J. Schaff, L. F. Eastman, R. Dimitrov, L. Wittmer, M. Stutzmann, W. Rieger, and J. Hilsenbeck, "Two-dimensional electron gases induced by spontaneous and piezoelectric polarization charges in N- and Ga-face AlGaN/GaN heterostructures," *J. Appl. Phys.*, vol. 85, no. 6, p. 3222, 1999.

[5] E. Alekseev, A. Eisenbach, D. Pavlidis, S. Hubbard, and W. Sutton, "GaN-based NDR Devices for THz Generation," *Int. Symp. Sp. Terahertz Technol.*, p. 162, 2000.

[6] E. Alekseev and D. Pavlidis, "Large-signal microwave performance of GaN-based NDR diode oscillators," *Solid. State. Electron.*, vol. 44, no. 6, pp. 941–947, 2000.

[7] T. Sasaki and S. Zembutsu, "Substrate-orientation dependence of GaN single-crystal films grown by metalorganic vapor-phase epitaxy," *J. Appl. Phys.*, vol. 61, no. 7, pp. 2533–2540, 1987.

[8] D. D. Koleske, M. E. Coltrin, K. C. Cross, C. C. Mitchell, and A. A. Allerman, "Understanding GaN nucleation layer evolution on sapphire," *J. Cryst. Growth*, vol. 273, no. 1–2, pp. 86–99, 2004.

[9] H. Amano, N. Sawaki, I. Akasaki, and Y. Yoyoda, "Metalorganic vapor phase epitaxial growth of a high quality GaN film using an AlN buffer layer," *Appl. Phys. Lett.*, vol. 48, no. 1986, pp. 353–355, 1986.

[10] M. G. Mynbaeva, A. V. Kremleva, D. A. Kirilenko, A. A. Sitnikova, A. I. Pechnikov, K. D. Mynbaev, V. I. Nikolaev, V. E. Bougrov, H. Lipsanen, and A. E. Romanov, "TEM study of defect structure of GaN epitaxial films grown on GaN/Al2O3 substrates with buried column pattern," *J. Cryst. Growth*, vol. 445, pp. 30–36, 2016.

[11] J. W. Pomeroy, M. Kuball, M. J. Uren, and T. Martin, "Direct optical

measurement of hot-phonons in active AlGaN/GaN devices," *Phys. Status Solidi*, vol. 245, no. 5, pp. 910–912, May 2008.

[12] N. Killat, M. J. Uren, S. Keller, S. Kolluri, U. K. Mishra, M. Kuball, N. Killat, M. J. Uren, S. Keller, S. Kolluri, U. K. Mishra, and M. Kuball, "Impact ionization in N-polar AlGaN / GaN high electron mobility transistors," *Appl. Phys. Lett.*, vol. 105, no. 6, pp. 1–4, 2014.

[13] C. Y. Zhu, M. Wu, C. Kayis, F. Zhang, X. Li, R. A. Ferreyra, A. Matulionis, V. Avrutin, U. Ozgur, and H. Morkoc, "Degradation and phase noise of InAlN/AlN/GaN heterojunction field effect transistors: Implications for hot electron/phonon effects," *Appl. Phys. Lett.*, vol. 101, no. 10, pp. 1–4, 2012.

[14] J. R. Hook and H. E. Hall, *Solid State Physics*, 2nd ed. John Wiley & Sons Ltd, 1991.

[15] F. Shi, *GaN Nanowires Fabricated by Magnetron Sputtering Deposition*. InTech, 2011.

[16] Y. Wang, H. Yin, R. Cao, F. Zahid, and Y. Zhu, "Electronic structures of III-V zinc-blende semiconductors from atomistic first principles," *arXiv*, pp. 1–4, 2013.

[17] L. Shuti and O. Chuying, "First principles study of wurtzite and zinc blende GaN," *Phys. Lett. A*, vol. 336, no. 2–3, 2004.

[18] K. Tomizawa, *Numerical Simulation of Submicron Semiconductor Devices*. 1993.

[19] M. Lundstrom, *Fundementals of carrier transport*, 2nd ed. Cambridge University Press, 2000.

[20] M. Poljak and V. Jovanovi, "Assessment of Electron Mobility in Ultrathin-Body InGaAs-on-Insulator MOSFETs," vol. 59, no. 6, pp. 1636–1643, 2012.

[21] B. K. Ridley, *Quantum Processes in Semicondcutors*, 4th ed. 1999.

[22] D. R. Naylor, A. Dyson, and B. K. Ridley, "Steady-state and transient electron transport in bulk GaN employing an analytic bandstructure," *Solid State Commun.*, vol. 152, no. 6, pp. 549–551, 2012.

[23] D. Vasileska, *Computational Electronics - Semiclassical and Quantum Device Modelling and Simulation*. CRC Press, 2010.

[24] B. K. Ridley, *Electrons and Phonons in Semiconductor Multilayers*, 2nd ed. Cambridge University Press, 2009.

[25] B. K. Ridley, W. J. Schaff, and L. F. Eastman, "Theory of the GaN crystal diode: Negative mass negative differential resistance," *J. Appl. Phys.*, vol. 97, no. 9, p. 094503, 2005.

[26] Encyclopædia Britannica, "Gas," *Encyclopædia Britannica*, 2013. [Online]. Available: http://www.britannica.com/EBchecked/topic/226306/gas/51950/Boltzmann-equation?anchor=ref507044. [Accessed: 15-Mar-2013].

[27] K. F. Brennan and D. H. Park, "Theoretical comparison of electron real-space transfer in classical and quantum two-dimensional heterostructure systems," *J. Appl. Phys.*, vol. 65, no. 3, p. 1156, 1989.

[28] R. Sakamoto, K. Akai, and M. Inoue, "Real-Space Transfer and Hot-Electron Transport Properties in III-V Semiconductor," vol. 3, no. 8930183, pp. 2344–2352, 1989.

[29] E. Bellotti and F. Bertazzi, *Nitride Semiconductor Devices*, 2007th ed. Weinheim: Wiley-VCH, 2007.

[30] V. Bougrov, M. E. Levinshtein, S. L. Rumyantsev, and A. Zubrilov, *Properties of Advanced Semiconductor Materials*. New York: John Wiley & Sons Ltd, 2001.

[31] T. P. Chow and Ghezzo, *II-Nitride, SiC, and Diamond Materials for Electronic Devices*. Pittsburgh: MRS Proceedings, 1996.

[32] J. M. B. D. K. Ferry and S. M. Goodnick, "Studies of High Field transport in GaN / AIGaN Heterostructures," vol. 1, no. 1, pp. 2261–2264, 2004.

[33] R. P. Joshi, S. Viswanadha, P. Shah, and R. D. Del Rosario, "Monte Carlo analysis of GaN-based Gunn oscillators for microwave power generation," *J. Appl. Phys.*, vol. 93, no. 8, pp. 4836–4842, 2003.

[34] M. Semenenko, O. Yilmazoglu, H. L. Hartnagel, and D. Pavlidis, "Determination of satellite valley position in GaN emitter from photoexcited field emission investigations," *J. Appl. Phys.*, vol. 109, no. 2, pp. 1–4, 2011.

[35] M. Shur, *GaAs Device and Circuits*. New York: Springer Science, 1989.

[36] B. K. Ridley and T. B. Watkins, "The Possibility of Negative Resistance Effects in Semiconductors," *Proc. Phys. Soc.*, vol. 78, no. 2, pp. 293–304, 1961.

[37] K. Hess, "Advanced theory of semiconductor devices," in *Wiley Interscience*, vol. 1, 2000.

[38] S. M. Sze, *Physics of Semiconductor Devices*, 2nd ed. New York: John Wiley & Sons Ltd, 1981.

[39] Y. Wang, L. A. Yang, Z. Z. Wang, J. P. Ao, and Y. Hao, "The enhancement of the output characteristics in the GaN based multiple-channel planar Gunn diode," *Phys. Status Solidi Appl. Mater. Sci.*, vol. 1258, no. 5, pp. 1252–1258, 2015.

[40] W. Heinle, "Experimental verification of bistable switching with gunn diodes," *Electron. Lett.*, vol. 7, no. 10, pp. 246–247, 1971.

[41] A. Dyson, D. R. Naylor, and B. K. Ridley, "Hot-Phonon Effects on High-Field Transport in GaN and AlN," *IEEE Trans. Electron Devices*, vol. 62, no. 11, pp. 3613–3618, 2015.

[42] J. Ajayan and D. Nirmal, "A review of InP/InAlAs/InGaAs based transistors for high frequency applications," *Superlattices Microstruct.*, vol. 86, pp. 1–19, 2015.

[43] P. Lugli, C. Jacoboni, L. Reggiani, and P. Kocevar, "Monte Carlo algorithm for hot phonons in polar semiconductors," *Appl. Phys. Lett.*, vol. 50, no. 18, p. 1251, 1987.

[44] R. F. Macpherson, G. M. Dunn, and N. J. Pilgrim, "Simulation of gallium nitride Gunn diodes at various doping levels and temperatures for frequencies up to 300 GHz by Monte Carlo simulation, and incorporating the effects of thermal heating," *Semicond. Sci. Technol.*, vol. 23, p. 055005, 2008.

[45] A. Khalid, G. M. Dunn, R. F. Macpherson, S. Thoms, D. Macintyre, C. Li, M. J. Steer, V. Papageorgiou, I. G. Thayne, M. Kuball, C. H. Oxley, M. Montes Bajo, a. Stephen, J. Glover, and D. R. S. Cumming, "Terahertz oscillations in an In0.53Ga0.47As submicron planar Gunn diode," *J. Appl. Phys.*, vol. 115, pp. 0–6, 2014.

[46] D. R. Naylor, "Development of Monte-Carlo Simulations for III-V Semiconductors employing an analytic band-structure," University of Hull, 2012.

[47] S. Laux, "On particle-mesh coupling in Monte Carlo semiconductor device simulation," *IEEE Trans. Comput. Des.*, vol. 15, no. 10, 1996.

[48] W. Press, T. Saul, V. William, and B. Flannery, *Numerical Recipes in Fortran 90*, 2nd ed. Cambridge University Press, 2010.

[49] L. Hirst, M. Führer, D. J. Farrell, A. Lebris, J. Guillemoles, M. J. Y. Tayebjee, R. Clady, T. W. Schmidt, Y. Wang, and M. Sugiyama, "Hot carrier dynamics in InGaAs/GaAsP quantum well solar cells," *13th Photovolt. Spec. Conf.*, p. 3302, 2011.

[50] J. B. Khurgin, S. Bajaj, and S. Rajan, "Elastic scattering by hot electrons and apparent lifetime of longitudinal optical phonons in gallium nitride," *Appl. Phys. Lett.*, vol. 107, no. 26, pp. 1–5, 2015.

[51] S. Bajaj, O. F. Shoron, P. S. Park, S. Krishnamoorthy, F. Akyol, T. H. Hung, S. Reza, E. M. Chumbes, J. Khurgin, and S. Rajan, "Density-dependent electron transport and precise modeling of GaN high electron mobility

transistors," *Appl. Phys. Lett.*, vol. 107, no. 15, pp. 1–4, 2015.

[52] M. Ramonas, A. Matulionis, and L. Rota, "Monte Carlo simulation of hot-phonon and degeneracy effects in the AlGaN/GaN two-dimensional electron gas channel," *Semicond. Sci. Technol.*, vol. 18, no. 2, pp. 118–123, Feb. 2003.

[53] E. Tea, H. Levard, and J. F. Guillemoles, "Advanced modeling of hot carrier effects in 3rd Generation Solar Cells," *Eur. Photovolt. Sol. Energy Conf.*, pp. 1–4, 2011.

[54] A. A. Maznev, F. Hofmann, A. Jandl, K. Esfarjani, M. T. Bulsara, E. a. Fitzgerald, G. Chen, and K. a. Nelson, "Lifetime of sub-THz coherent acoustic phonons in a GaAs-AlAs superlattice," *Appl. Phys. Lett.*, vol. 102, pp. 1–13, 2013.

[55] R. Mickevičius and A. Reklaitis, "Hot phonon effects on electron high-field transport in GaAs," *J. Phys. Condens. Matter*, vol. 1, pp. 9401–9412, 1989.

[56] B. K. Ridley, "Hot phonons in high-field transport," *Semiconductor Science and Technology*, vol. 4. pp. 1142–1150, 1999.

[57] M. Rieger, P. Kocevar, P. Lugli, P. Bordone, L. Reggiani, and S. M. Goodnick, "Monte Carlo studies of nonequilibrium phonon effects in polar semiconductors and quantum wells. II. Non-Ohmic transport in n-type gallium arsenide," *Phys. Rev. B*, vol. 39, no. 11, pp. 7866–7875, 1989.

[58] C. Bulutay, B. Ridley, and N. Zakhleniuk, "Electron momentum and energy relaxation rates in GaN and AlN in the high-field transport regime," *Phys. Rev. B*, vol. 68, no. 11, p. 115205, Sep. 2003.

[59] P. Bordone, C. Jacoboni, P. Lugli, L. Reggiani, and P. Kocevar, "Effect of a perturbed acoustic-phonon distribution on hot-electron transport: A Monte Carlo analysis," *J. Appl. Phys.*, vol. 61, no. 4, pp. 1460–1468, 1987.

[60] A. Rostami, H. Rasooli, and H. Baghban, "Terahertz Technology," *IEEE Trans. Microw. Theory Tech.*, vol. 77, no. 3, pp. 910–928, 2011.

[61] X. Yin, B. W.-H. Ng, and D. Abbott, *Terahertz Imaging for Biomedical Applications*. Springer Science, 2012.

[62] S. K. Sharma and D. Y. Kim, "Design, simulation, fabrication, packaging and testing of an AlGaAs/GaAs Gunn diode at 94 GHz," *J. Korean Phys. Soc.*, vol. 67, no. 4, pp. 619–624, 2015.

[63] M. I. Maricar, A. Khalid, G. Dunn, D. Cumming, and C. H. Oxley, "Experimentally estimated dead space for GaAs and InP based planar Gunn diodes," *Semicond. Sci. Technol.*, vol. 30, no. 1, p. 012001, 2015.

[64] M. I. Maricar, J. Glover, A. Khalid, C. Li, G. Evans, D. R. S. Cumming, and

C. H. Oxley, "An AlGaAs/GaAs-Based Planar Gunn Diode Oscillator With A Fundemental Frequency Operation Of 120 GHZ," *Microw. Opt. Technol. Lett.*, vol. 56, no. 10, pp. 2449–2451, 2014.

[65] K. Tomizawa, Y. Awano, N. Hashizume, and M. Kawashima, "Monte Carlo simulation of submicron GaAs n+ −i(n)−n+ diode," *IEE Proc. I Solid State Electron Devices*, vol. 129, p. 131, 1982.

[66] P. Lugli, "The Monte Carlo method for semiconductor device and process modeling," *IEEE Trans. Comput. Des. Integr. Circuits Syst.*, vol. 9, no. 11, 1990.

[67] D. P. Adorno, M. Zarcone, and G. Ferrante, "Far-Infrared Harmonic Generation in Semiconductors : A Monte Carlo Simulation," vol. 10, no. 1, pp. 310–315, 2000.

[68] M. Fischetti and S. Laux, "Monte Carlo analysis of electron transport in small semiconductor devices including band-structure and space-charge effects," *Phys. Rev. B*, vol. 38, no. 14, 1988.

[69] INSPEC, *Properties of Gallium Arsenide*. The Institution of Electrical Engineers, London, 1986.

[70] O. Madelung, U. Rossler, and M. Schulz, *Group IV Elements, IV-IV and III-V Compounds. Part a - Lattice Properties*. Landolt-Börnstein - Group III Condensed Matter, Vol. a (Springer-Verlag, Berlin/Heidelberg, 2001).

[71] A. Aishima, K. Yokoo, and S. Ono, "An Analysis of Wide-Band Transferred Electron Device," *IEEE Trans. Electron Devices*, vol. 25, no. 6, pp. 640–645, 1978.

[72] G. M. Dunn and M. J. Kearney, "A theoretical study of differing active region doping profiles for W-band (75–110 GHz) InP Gunn diodes," *Semicond. Sci. Technol.*, vol. 18, no. 8, pp. 794–802, 2003.

[73] C. Sevik and C. Bulutay, "Efficiency and harmonic enhancement trends in GaN-based Gunn diodes: Ensemble Monte Carlo analysis," *Appl. Phys. Lett.*, vol. 85, no. 17, pp. 3908–3910, 2004.

[74] H. Arabshahi and F. Taghavi, "Calculation of High Field Electron Transport Properties in GaSb and GaAs Using a Monte Carlo Method," *Res. J. Appl. Sci.*, vol. 6, no. 3, pp. 213–217, 2011.

[75] A. Guen-Bouazza, C. Sayah, B. Bouazza, and N. E. Chabane-Sari, "Steady-State and Transient Electron Transport within Bulk InAs, InP and GaAs: An Updated Semiclassical Three-Valley Monte Carlo Simulation Analysis," *J. Mod. Phys.*, vol. 04, no. 05, pp. 616–621, 2013.

[76] S. Vainshtein, V. Yuferev, V. Palankovski, D. S. Ong, and J. Kostamovaara,

"Negative differential mobility in GaAs at ultrahigh fields: Comparison between an experiment and simulations," *Appl. Phys. Lett.*, vol. 92, no. 6, pp. 2–5, 2008.

[77] A. Khalid, N. J. Pilgrim, G. M. Dunn, M. C. Holland, C. R. Stanley, I. G. Thayne, and D. R. S. Cumming, "A planar Gunn diode operating above 100 GHz," *IEEE Electron Device Lett.*, vol. 28, no. 10, pp. 849–851, 2007.

[78] A. Nakagawa, K. Watanabe, T. Yoshida, T. Deguchi, and Y. Oki, "77 GHz Planar Gunn VCOs on AlN Substrates Using Novel Flip-Chip InP Gunn Diodes," *IEEE MTT-S Int. Microw. Symp. Dig.*, 2000.

[79] H. Eisele and R. Kamoua, "Submillimeter-wave InP Gunn devices," *IEEE Trans. Microw. Theory Tech.*, vol. 52, no. 10, pp. 2371–2378, 2004.

[80] Y. P. Teoh, G. M. Dunn, N. E. Priestley, and M. Carr, "Monte Carlo simulations of asymmetry multiple transit region Gunn diodes," *Semicond. Sci. Technol.*, vol. 20, no. 5, pp. 418–422, 2005.

[81] E. Momox, N. Zakhleniuk, and N. Balkan, "Overshoot mechanism in transient excitation of THz and Gunn oscillations in wide-bandgap semiconductors.," *Nanoscale Res. Lett.*, vol. 7, p. 647, 2012.

[82] M. Piccardo, L. Martinelli, J. Iveland, N. Young, S. P. Denbaars, S. Nakamura, J. S. Speck, C. Weisbuch, and J. Peretti, "Determination of the first satellite valley energy in the conduction band of wurtzite GaN by near-band-gap photoemission spectroscopy," *Phys. Rev. B - Condens. Matter Mater. Phys.*, vol. 89, no. 23, pp. 1–5, 2014.

[83] M. Shur, *Physics of Semiconductor devices*, vol. 1. 1998.

[84] V. N. Sokolov, K. W. Kim, V. a. Kochelap, and D. L. Woolard, "Terahertz generation in submicron GaN diodes within the limited space-charge accumulation regime," *J. Appl. Phys.*, vol. 98, no. 2005, p. 064507, 2005.

[85] E. A. Barry, V. N. Sokolov, K. W. Kim, and R. J. Trew, "Terahertz generation in GaN diodes operating in pulsed regime limited by self-heating," *Appl. Phys. Lett.*, vol. 94, no. 2008, pp. 2007–2010, 2009.

[86] E. A. Jones, F. Wang, and B. Ozpineci, "Application-based review of GaN HFETs," *2nd IEEE Work. Wide Bandgap Power Devices Appl. WiPDA 2014*, pp. 24–29, 2014.